# Microfabricated Reactors for Partial Oxidation Reactions

by

Ravi Srinivasan

B.Tech., Indian Institute of Technology, Bombay (1992)

Submitted to the Department of Chemical Engineering
in partial fulfillment of the requirements for the degree of

Doctor of Philosophy

at the

MASSACHUSETTS INSTITUTE OF TECHNOLOGY

February 1998



Signature of Author .....
Department of Chemical Engineering
October 28, 1997

Certified by .....
Martin A. Schmidt
Associate Professor of Electrical Engineering
Thesis Supervisor

Certified by .....
Klavs F. Jensen
Lammot du Pont Professor of Chemical Engineering
Thesis Supervisor

Accepted by .....
Robert E. Cohen
St. Laurent Professor of Chemical Engineering
Chairman, Committee for Graduate Students

# Microfabricated Reactors for Partial Oxidation Reactions

by

Ravi Srinivasan

Submitted to the Department of Chemical Engineering
in partial fulfillment of the requirements for the degree of
Doctor of Philosophy

Micromachining technology allows fabrication of novel chemical reactors having several potential advantages over conventional techniques. Microfabricated chemical reactor (microreactor) systems offer distributed point-of-use chemical manufacturing for safer operation without storage and transportation hazards; ability to tailor reactor geometries of submillimeter to micron dimensions for improved performance; improved process control by integrated sensors and actuators; and shorter development time from laboratory to chemical production. To test these concepts, microreactors were fabricated and tested for gaseous catalytic partial oxidation reactions.

Microreactors having sub-millimeter flow channels, with integrated heaters and flow and temperature sensors were fabricated on Si. Thin film Pt lines served as resistive heaters, and flow and temperature sensors. The flow sensor was a thin-film hot-wire anemometer, and the temperature sensor was a thin-film resistance temperature device (RTD). The individual reactants are mixed on-chip, and reacted on a heated catalyst. The reaction products were monitored externally using a quadrupole mass spectrometer. Several highly flammable gas mixtures without diluents (*e.g.*, 20% $H_2$ and $O_2$, $NH_3$ and $O_2$ at all compositions, $C_2H_6$ and $O_2$ at all compositions) were ignited in the microreactor, without an explosion, demonstrating the safety potential of the microreactor.

Conversion-selectivity issues and ignition-extinction behavior was explored using Pt catalyzed $NH_3$ oxidation as the model reaction. Comparisons with conventional laboratory reactors indicated that the conversion-selectivity performance was limited by the microreactor channel height. Decreasing the channel height by 50% enhanced the conversion by ~10%. Heat transfer was enhanced by fabricating microreactors with higher thermal conductivity Si membranes (Si microreactors). The excellent heat transfer of Si microreactor allowed operation in novel regimes inaccessible by conventional reactors. Unlike conventional reactors, Si microreactors could be operated between ignition and extinction temperatures. Operation in these novel temperature regimes could be very useful in hydrocarbon partial oxidation reactions for changing the product distribution, and increasing selectivity to the desired partial oxidation product.

Scale-up for industrial use could be achieved by operating several microreactors, in parallel, as minichemical systems. Calculations based on the test results of the prototype SiN microreactor indicate that microreactor-based systems could be useful for small quantity point-of-use chemical production. The microreactor operation was limited to

~650°C due to thermal stresses and material degradation. While further research is required to improve high temperature stability, and address scale-up and cost issues, the current design and operation of a single microreactor could be used as a laboratory platform for kinetic studies. The advantages provided by microreactors for kinetic studies include safety, low reactant usage, less waste, and well-defined geometries that allow relatively simple simulations for better understanding of reaction kinetics.

**Thesis Supervisor: Martin A. Schmidt**
**Title: Associate Professor of Electrical Engineering**

**Thesis Supervisor: Klavs F. Jensen**
**Title: Lammot du Pont Professor of Chemical Engineering**

# Acknowledgments

It has been a lot of fun and a great learning experience to question the conventional wisdom of building large plants, and asking what we can do by building chemical equipment as small as possible using newly available microfabrication technologies. I thank my advisors Marty Schmidt and Klavs Jensen for allowing me to work on this exciting topic, and guiding me to build a microreactor that actually works! It was Marty's innovative ideas and Klavs's breadth of chemical engineering knowledge that made this thesis happen. I thank Marty for taking me on as a student when only a vague idea of the project existed, and for his approachability and patience especially with my procrastination. I thank Klavs for always making time for me and taking care of many details inspite of his very tight schedule, and for his willingness to help.

I thank DuPont for funding part of this work and especially for allowing a great degree of freedom in pursuing my ideas. It was pleasure working with DuPont personnel- Jan Lerou was always supportive as a manager, Mike Harold provided input on reaction chemistries and took time to be on my thesis committee, and Jim Ryley provided a lot of assistance in fabricating microreactors. I am grateful to my undergraduate mentors- Prof. Jayesh Bellare, Prof. Arvind Kudchadker, and Prof. Rakesh Lal for getting me started on miniaturization, and for supporting 'an undergraduate kid' to take on ambitious projects.

One of the fondest memories at MIT are my interactions with my fellow students. I have been lucky to be working with students of the KFJ-group and Schmidt-group. These

groups have very different skill sets and strengths, and I have learnt a lot from interacting with them. I thank them for helping me in innumerable ways in my thesis, and for being great friends. I especially thank Errol and Kerri for treating me as a part of their family and going out of their way to help me. Peter Berger and Theresa Liu were great UROPs, helping me carry out experiments. It was fun sparring with I-Ming on some of the technical issues regarding microreactors. I also thank Samara for taking time to fabricate several microreactors for me.

I thank my thesis committee members- Prof. Satterfield, Prof. Sawin, Prof. Ying, and Dr. Mike Harold for guiding me through this thesis. I benefited greatly from Prof. Satterfield's enormous experience in heterogeneous catalysis. I thank the MTL staff, particularly Octo, for help in the clean-rooms.

Finally, I am indebted to my parents for all their sacrifices for my benefit. I dedicate this thesis to them.

# Contents

# List of Figures

# Chapter 1 Introduction and Motivation

The chemical industry has traditionally operated large plants in centralized location for economies of scale. Environmental and market pressures are forcing a rethink of the large scale operation design paradigm [1-3]. Although the chemical industry has an excellent safety record, large scale plant operation and shipping of products cause accidents that sometimes even lead to loss of life [4-8]. Further, large plants have the disadvantage of inflexible operation to meet changing product demand. Sudden increases in product demand cannot be met due to the large time (several months to years) needed to build large plants, and sudden decreases in product demand leads to idle capacity. Recent reports have suggested operation of small, highly automated plants for increased safety and flexible operation [1, 3]. Point-of-use, on-demand, distributed chemical production in miniaturized chemical plants (minichemical systems) can improve safety due to the smaller potential damage, and due to elimination of shipping and transportation hazards[1]. The economies of scale of large plants could be offset by economies of mass production (the use of standardized components that are replicated and mass produced), as in the automobile and consumer electronics industry [3]. This thesis explores the use of the emerging technology of micromachining to fabricate a chemical reactor that could be used in a minichemical plant. The target application for the microreactor is toxic and potentially explosive catalytic partial oxidation reactions, an important class of reactions that could benefit from increased safety due to miniaturization and point-of-use production in minichemical systems.

Previous work in miniaturization in the chemical industry is reviewed, following which, a brief introduction to microfabrication technology and its potential advantages for chemical production is presented. Partial oxidation reactions are then introduced, and the advantages offered by microreactors for these reactions are presented.

## 1.1 Prior Work on Miniaturization in Chemical Industry

The chemical industry constantly strives to increase productivity and efficiency of unit operations. But, until recently, there was no active research effort dedicated to miniaturization of chemical unit operations. The earliest published work on miniaturization of plant components was from ICI in the early 1980s, under the title of Process Intensification [9]. The aim of process intensification was to identify and improve efficiencies of heat and mass transport limited chemical processes. A successful implementation of the process intensification strategy included the 'Higee' miniature gas-liquid distillation unit, that used centrifugal forces to enhance mass transfer for improved efficiency and reduced unit size compared with conventional distillation columns [10]. The high centrifugal forces (upto 1000g compared with 1g of conventional distillation columns), induced large liquid shear creating a thin liquid film on the column packing. The thin liquid film enhanced contact with the gas phase. The ICI group also fabricated a miniature heat exchanger having small diameter (1mm) channels using photo-etched copper sheets and pressed titanium plates. The small channel diameters offered large surface to volume ratios for enhanced heat transfer [9].

In the late eighties, a group in Forschungszentrum Karlsruhe in Germany built a miniature heat exchanger (of volume $1cm^3$ ) having smaller diameter channels (~100μm) by diamond point milling an Al plate [11]. Tests showed that the heat transfer

coefficients (~$2x10^4$ $W/m^2/K$) of the miniature heat exchanger were ~20x the heat transfer coefficient of conventional heat exchangers.

The technology of diamond point milling of metal sheets developed at Forschungszentrum Karlsruhe was adapted and used by several groups to build chemical reactors for partial oxidation reactions: Honicke and Weissmeir have demonstrated the partial oxidation of propene to acrolein on milled Cu sheets that were oxidized to form catalytically active $Cu_2O$ [12]. Milled Al sheets were also anodically oxidized to form porous $Al_2O_3$ support for increased surface to volume ratios [13]. The metal milling technique has also been adapted by BASF to build microreactors [14]. BASF is pursuing several possible applications for microreactors including cataytic screening, kinetic measurement, and increasing safety of potentially explosive reactions.

In the early 1990s, DuPont had initiated exploratory research to identify and apply microfabrication methods to chemical unit operation designs for improved performance. DuPont has fabricated externally heated silicon microchannel reactors, and demonstrated several hazardous reactions that included fast catalytic reactions (HCl oxidation to $Cl_2$, Production of HCN, Methyl Iso Cyanate (MIC), and $COCl_2$ (phosgene) ); photochemical reactions (chlorination of dichloro-dimethyl-silane to dichloro-chloromethyl-silane); and high temperature reactions (butyl-amine phosgenation to butyl-iso-cyanate, cyclo-hexylamine phosgenation to cyclo-hexyl-isocyanate) [1]. An excellent summary of the potential applications of microfabricated chemical reactors has also been presented [1].

The research group at Institut für Mickrotechnik (Mainz, Germany) used x-ray photolithography, electroplating and injection molding (collectively known as LIGA

technique), laser processing, and photoetched glass to fabricate integrated chemical units, e.g. micromixer- reaction chamber [15].

Researchers at Pacific Northwest National Laboratories (PNNL) have fabricated and carried out preliminary tests of microchannel heat exchangers, liquid-liquid mixers, and combustor-evaporators that have low $NO_x$ production [16]. They have also proposed the use of micromachined reactors for environmental restoration of contaminated ground-water, and for portable chemical plants for on-site $H_2$ production for fuel cells via liquid hydrocarbon (methanol) reforming.

## 1.2 Microfabrication technology for chemical systems

### 1.2.1 Brief overview of microfabrication

Microfabrication is an emerging field that has adapted established Integrated Circuits (IC) manufacturing steps such as thin film deposition, ion implantation, lithography, and etching, to fabricate miniature sensors and actuators with feature sizes of 1μm to 100μm [17]. The potential advantages offered by microfabrication for these applications include miniaturized parts, large volume low cost production due to batch fabrication, and improved performance via integration of electronics on-chip for increased sensitivity and lower noise. Pressure sensors and accelerometers (for airbag deployment) used in automobiles are commercially the largest volume microfabricated products. Due to the established knowledge base, microfabrication has traditionally used silicon and associated thin film materials such as polysilicon, silicon nitride, quartz, and I.C compatible metals for fabrication. However, microfabrication technology for new materials such as glass, ceramics (e.g. SiC) [18], and polymers are currently being

developed, which could potentially be adapted for a variety of chemical engineering applications requiring specialized materials. Several recent publications provide a good review of the technologies used in microfabrication [19] [17] [20] [21].

### 1.2.2 Microfluidic systems

In recent years, there has been considerable interest in microfabricated systems that involve fluid handling, or microfluidic systems, primarily for analysis and sensing, where they offer the advantages of small sample volumes and faster assay times[22]. Microfabricated separation and detection units include Gas Chromatographs (GCs) [23], Liquid Chromatographs (LCs) [24], and Capillary Electrophoresis (CE) units [25]. In addition to analysis systems, flow control and metering units such as valves [26], liquid pumps [27], and flowsensors [28] have also been microfabricated. Several of these chemical systems including the gas chromatograph, microvalve (http://www.redwoodmicro.com), and flowsensors are commercially available.

There has been considerable commercial interest in recent years for developing microfabricated analytical systems for biological applications-Affymetrix has developed a microfabricated chip for genetic disease testing (GeneChip®) [29]; Perkin Elmer is developing a DNA sequencing unit [30]; Caliper Technologies is working on a 'laboratory-on-a-chip' concept for clinical diagnostics (http://www.calipertech.com); Abbot Laboratories has developed a microfluidic test station [31]; and Cepheid is developing fluidic units for medical diagnostics [32].

Many of the technical challenges such as packaging, gas-bubble removal and surface tension effects in liquid flow, and macroworld-device interface are common to microfluidic devices irrespective of the end application being chemical analysis or

chemical production. Thus, the infrastructure being developed for the analytical instruments market could also adapted for chemical production.

### 1.2.3 Potential advantages of microfabricated systems for chemical production

Microfabrication offers integration of several functions on a single unit which sets microreactors apart from passive microchannel devices such as capillary reactors or honeycomb monolith reactors. For example, reactors can be integrated with flow, temperature and pressure sensors, as well as actuators such as valves in a single unit for improved process monitoring and control. In the event of a thermal runaway, the on-chip sensors would detect a sudden increase in temperature or pressure. Corrective measures such as shutting off the on-chip reactant valve and/or the heater, or introducing a purge stream, could then be initiated to prevent the runaway.

The use of photolithography in microfabrication offers tailored and complex channel network of desired dimensions for improved performance. This was used in the microreactor design to provide on-chip mixing capability, whereas conventional reactors have pre-mixed feed. Pre-mixed feed has the danger of thermal flashback, where the flame-front travels upstream to the mixing point, causing extensive damage to equipment in the path of the flame-front.

Scale-up can be achieved by operating several microreactors in parallel for minichemical systems. This parallel scale-up route has many advantages over conventional scale-up, which entails going from laboratory scale to a single large reactor unit through a series of costly laboratory experiments, pilot plant stages, and simulations. In contrast, since each microreactor would behave exactly alike individually and in replicated unit, scale-up would be considerably shorter and less expensive, allowing for

faster time to market, and flexible operation in the event of sudden changes in product demand.

### 1.3 Microreactors for partial oxidation reactions

Microreactors were fabricated for safer operation of gaseous hydrocarbon catalytic partial oxidation reactions. Hydrocarbon partial oxidation reactions are widely used in the chemical industry to produce oxygenates e.g. aldehydes, alcohols, and nitrogen bearing compounds e.g., cyanides, nitriles, and cyanates, for polymers and agricultural products [33]. Many of the products are toxic [33] making them ideal candidates for point-of-use production. In fact, the world's worst chemical accident in Bhopal occurred due to the leakage of a partial oxidation product: Methyl-iso-cyanate [4].

The high exothermicity ($\Delta H_{rxn}$~ 100kJ) of partial oxidations makes the control of conventional partial oxidation reactors, such as fixed-bed reactors and catalytic gauze reactors very difficult [33, 34]. Fixed bed reactors exhibit high parametric sensitivity-small changes in processing conditions such as feed temperature and inlet composition could lead to hot-spot formation and reactor melt-down [35] [36]. Gauze reactors are susceptible to chain branching reactions leading to flame formation, and are therefore run conservatively, outside the flammable regime [34]. Recently, fluidized bed reactors have been used for enhanced heat transfer in partial oxidation reactions [34]. Unfortunately, they are very difficult to design and operate efficiently. Microreactors, due to their large surface area to volume ratios, would have both enhanced heat transfer, potentially preventing a thermal runaway reaction, as well as wall-quenching of gas-phase radicals, allowing for safe operation in the flammable regime. Since partial oxidation reactions are

extremely fast (~1ms contact time), the throughput of one microreactor could be large enough that a modest number of microreactors operating in parallel could produce sufficient quantities of chemicals for point-of-use production.

### 1.4 Thesis outline

The goal of this work was to fabricate, on silicon, a microreactor with integrated heaters, flow and temperature sensors, and to test its behavior for exothermic and potentially explosive partial oxidation reactions. The prototype SiN microreactor design and fabrication issues are presented in Chapter 2. The experimental test setup is described in Chapter 3, and the catalytic partial oxidation experiments in the prototype SiN microreactor is described in Chapter 4. Based on the prototype microreactor results, improved microreactor designs for heat and mass transport were implemented, which are described in Chapter 5. Conclusions and recommendations for future work are presented in Chapter 6.

## References


[1] J. J. Lerou, M. P. Harold, J. Ryley, J. Ashmead, T. C. O'Brien, M. Johnson, J. Perrotto, C. T. Blaisdell, T. A. Rensi, and J. Nyquist, "Microfabricated Minichemical Systems: Technical Feasibility," presented at Microsystem Technology for Chemical and Biological Microreactors, Mainz, Germany, 1996.

[2] J. J. Lerou and K. M. Ng, "Chemical reaction engineering: A multiscale approach to a multiobjective task," *Chemical Engineering Science*, vol. 51, pp. 1595-1614, 1996.

[3] R. S. Benson and J. W. Ponton, "Process Miniaturization- A Route to Total Environmental Acceptability?," *Trans. ChemE.*, vol. 71A, pp. 160, 1993.

[4] W. Lepkowski, "Bhopal: Special Report," *C&EN*, vol. 63, pp. 18-32, 1985.

[5] W. Lepkowski, "Ten Years Later: Bhopal," *C&EN*, vol. 72, pp. 8-18, 1994.

[6] T. G. Theofanous, "A physicochemical mechanism for the ignition of the Seveso accident," *Nature*, vol. 291, pp. 640-642, 1981.

[7] T. G. Theofanous, "The physicochemical origins of the Seveso accident-1. Initial heatup," *Chemical Engineering Science*, vol. 38, pp. 1615-1629, 1983.

[8] T. G. Theofanous, "The physicochemical origins of the Seveso accident- 2. Induction period," *Chemical Engineering Science*, vol. 38, pp. 1631-1636, 1983.

[9] W. T. Cross and C. Ramshaw, "Process Intensification: Laminar Flow Heat Transfer," *Chemical Engineering Research and Design*, vol. 64, 1986.

[10] C. Ramshaw, *The Chemical Engineer*, vol. 389, pp. 13-14, 1983.

[11] K. Schubert, W. Bier, G. Linder, and D. Seidel, "Fabrication and testing of compact micro heatexchangers (In German)," *Chem.-Ing.-Tech.*, vol. 61, pp. 172-173, 1989.

[12] D. Hönicke and G. Weissmeier, "Heterogeneously Catalyzed Reactions in a Microreactor," presented at Microsystem Technology for Chemical and Biological Microreactors, Mainz, 1996.

[13] G. Wiessmeir and D. Hönicke, "Microfabricated components for heterogeneously catalysed reactions," *Journal of Micromechanics and Microengineering*, vol. 6, pp. 285-289, 1996.

[14] K.-P. Jäckel, "Microtechnology: Application Opportunities in the Chemical Industry," presented at Microsystem Technology for Chemical and Biological Microreactors, Mainz, 1996.

[15] H. Möbius, W. Ehrfeld, V. Hessel, and T. Richter, "Sensor controlled processes in chemical microreactors," presented at International Conference on Solid-State Sensors and Actuators, Stockholm, Sweden, 1995.

[16] R. S. Wegeng, C. J. Call, and M. K. Drost, "Chemical system miniaturization," presented at Spring National Meeting of the AIChE, New Orleans, 1996.

[17] L. Ristic, "Sensor technology and devices," . Boston: Artech house, 1993.

[18] N. Rajan, C. Zorman, M. Mehregany, and R. DeAnne, "3C-SiC coatings of silicon micromachined atomizers," presented at International Conference on Micro-Electro-Mechanical Systems, Nagoya, Japan, 1997.

[19] J. Bryzek, K. Peterson, and W. McCulley, "Micromachines on the march," *IEEE Spectrum*, pp. 20-31, May 1994.

[20] J. W. Gardner, *Microsensors: Principles and Applications*. New York: John Wiley and Sons, 1994.

[21] S. M. Sze, "Semiconductor Sensors," . New York: John Wiley and Sons, 1994.

[22] R. F. Service, "The incredibly shrinking laboratory," *Science*, vol. 268, pp. 26-27, 1995.

[23] J. B. Angell, S. C. Terry, and P. W. Barth, "Silicon micromechanical devices," *Scientific American*, vol. 248, pp. 44-55, April 1983.

[24] "Design of open tubular column liquid chromatograph using silicon chip technology," *Sensors and Actuators*, vol. B1, pp. 249-255, 1990.

[25] D. J. Harrison, K. Fluri, K. Seiler, Z. Fan, C. S. Effenhauser, and A. Manz, *Science*, vol. 261, pp. 895, 1993.

[26] P. W. Barth, "Silicon microvalves for gas flow control," presented at International Conference on Solid-State Sensors and Actuators, Stockholm, Sweden, 1995.

[27] A. S. Dewa, K. Deng, D. C. Ritter, C. Bonham, H. Guckel, and S. Massoud-Ansari, "Development of LIGA-fabricated, self-priming, in-line, gear pumps," presented at International Conference on Solid-State Sensors and Actuators, Chicago, 1997.

[28] T. R. Ohnstein, R. G. Johnson, R. E. Higashi, D. W. Burns, J. O. Holmen, E. A. Satren, G. M. Johnson, R. E. Bicking, and S. D. Johnson, "Environmentally rugged, wide dynamic range microstructure airflow sensor," presented at Solid-State Sensor and Actuator Workshop, Hilton Head, SC, 1990.

[29] R. C. Anderson, G. J. Bogdan, Z. Barniv, T. D. Davies, J. Winkler, and K. Roy, "Microfluidic biochemical analysis system," presented at International Conference on Solid-State Sensors and Actuators, Chicago, 1997.

[30] M. Albin, R. Kowaliks, E. Picozza, Y. Raysberg, C. Sloan, E. Winn-Deen, T. Woudenberg, and T. Zupfer, "Micromachining and microgenetics: What are they and where do they work together?," presented at Solid-State Sensor and Actuator Workshop, Hilton Head, SC, 1996.

[31] D. VerLee, A. Alcock, G. Clark, T. M. Huang, S. Kantor, T. Nemcek, J. Norlie, J. Pan, F. Wadsworth, and S. T. Wong, "Fluid circuit technology: Integrated interconnect technology for miniature fluidic devices," presented at ISolid-State Sensor and Actuator Workshop, Hilton Head. SC, 1996.

[32] K. Peterson, "Biomedical Applications of MEMS," presented at International Electron Devices Meeting, San Francisco, 1995.

[33] C. N. Satterfield, *Heterogeneous Catalysis in Industrial Practice*, 2nd ed. New York: McGraw-Hill Inc., 1991.

[34] L. D. Schmidt, M. Huff, and S. S. Bharadwaj, "Catalytic partial oxidation reactions and reactors," *Chemical Engineering Science*, vol. 49, pp. 3981-3994, 1994.

[35] M. Morbidelli and A. Varma, "A generalized criterion for parametric sensitivity: application to thermal explosion theory," *Chemical Engineering Science*, vol. 43, pp. 91, 1988.

[36] G. F. Froment and K. B. Bischoff, *Chemical Reactor Analysis and Design*, 2nd ed. New York: J. Wiley & Sons, 1990.

# Chapter 2 Microreactor Design and Fabrication

A prototype microreactor having a sub-millimeter channel with integrated heaters and, flow and temperature sensors, was fabricated on Si using standard microfabrication techniques in MIT's clean room facility (Microsystems Technology Laboratory). The detailed description of the device is presented in Section 2.1, followed by a literature survey of relevant microfabrication work and its influence on the microreactor design in Section 2.2. Simple thermal and reaction engineering models used to design the microreactor dimensions are detailed in Section 2.3, and the fabrication procedure is described in Section 2.4.

## 2.1 Microreactor description and survey of relevant microfabrication designs

### 2.1.1 Description and Overview of the microreactor

The microreactor consists of a T-shaped channel (in top-view) for gas flow etched in a silicon wafer (Figures 2.1 and 2.2). The channel is capped from the top by a 1 μm thick silicon nitride (SiN) membrane and sealed from the bottom with an aluminum plate having 3 gas inlet-outlet holes. The reactants enter at the two horizontal ends of the T-shaped channel, mix at the entrance, and react in the vertical reaction channel. The products exit at the vertical end of the T.

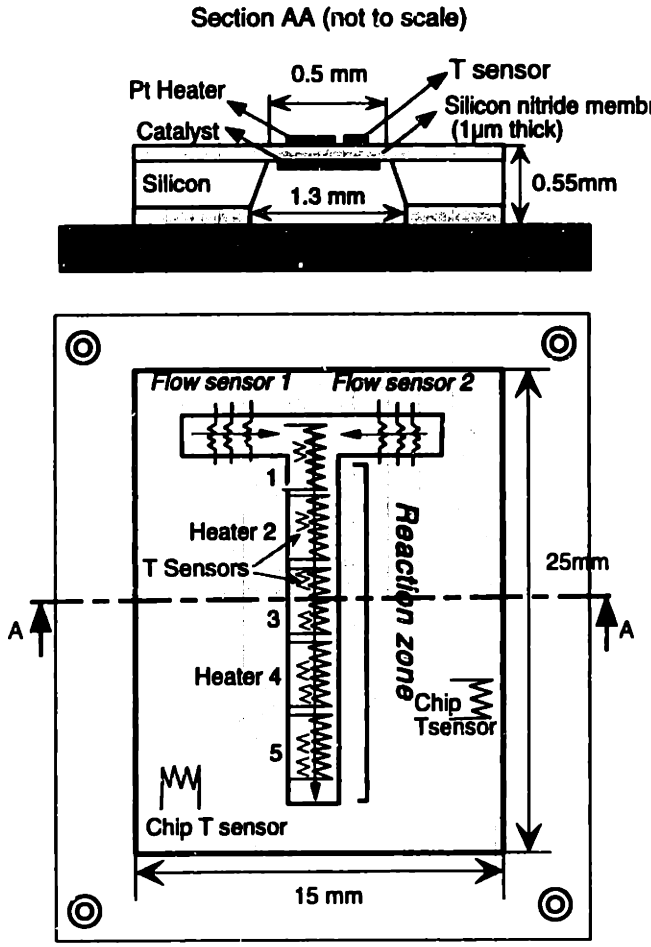


***Figure 2.1** Schematic figure of the microreactor.*

The top-face of the SiN membrane has thin film Pt lines deposited, which serve as resistive heaters, and flow and temperature sensors. The flow sensor is a thin-film hot-wire anemometer; the temperature sensor is a thin-film resistance temperature device (RTD) [1]. Both devices rely on the increase of electrical resistance of Pt with temperature. A thin film Pt catalyst, coated on the bottom-face (channel-side) of the SiN membrane in the reaction channel, is resistively heated by the thin film heater deposited on the top-face of the membrane. The temperature is measured by the sensors present adjacent to the heaters (Figure 2.1). Thus the catalyst is thermally coupled with the heater and temperature sensor via the 1 μm thick silicon nitride membrane.

***Figure 2.2 Photograph of microreactor showing the Si chip (2.5 × 1.5 $cm^2$) epoxied to the Al sealing plate. Pt metal lines forms heaters, flow and temperature sensors. The lines terminate in bond pads at the edges of the chip. (Felice Frankel©, MIT).***

Finite Element simulations show that the temperature variation across the thickness of the silicon nitride membrane is negligible [2], which indicates that the temperature sensor measurements accurately represent the catalyst temperature.

## 2.2 Survey of relevant microfabrication work

### 2.2.1 Microfabricated thermal microstructures

The microreactor requires a thermal microstructure that would allow the catalyst to be resistively heated to ignition temperatures at a reasonable power. Several thermally isolated microstructures have previouly been microfabricated, primarily for combustible and metal-oxide gas sensors [3, 4] [5], anemometer flow sensors[6], infra-red sources and detectors [7-9], and thermal actuators for applications such as microvalves [10]. For these applications, the thermally isolated microstructures offered improved performance via low power operation and fast time response, compared with conventional fabrication techniques. The thermally isolated structure designs consisted of SiN membranes and microbridges [11-13] , sandwich structures of $SiO_2$ and $Si_3N_4$ for stress-relieved membranes [5], polysilicon microbridges and shells [14-16], Si cantilevers [8, 17], and $SiO_2$ bridges and membranes [16]. The $SiO_2$ and $Si_3N_4$ sandwich structures require extensive studies of different film thickness, and careful deposition control, to optimize the composite film stress for sturdy structures. Si microstructures, although robust, have

the disadvantage of large heat loss due to the high thermal conductivity of Si ($k_{Si}$ = 140 W/m/K), requiring higher power operation. Polysilicon microstructures have an intrinsic stress that is process-dependent, requiring controlled deposition [18], and $SiO_2$ microbridges are structurally unstable because of the high intrinsic stresses. We used low-stress SiN membranes due to their superior mechanical properties [6], as the microreactor thermal microstructures.

While the flowsensor and IR detection applications require extremely good thermal isolation for low-power operation, the microreactor requires good heat removal capability to control exothermic reactions. The microreactor design therefore involved a tradeoff in providing sufficient thermal isolation for ignition, and sufficient heat removal capability for reaction exotherms after ignition (Section 2.3.1). Si membranes were also designed and used as microstructured thermal conductors, and are described in Chapter 5.

### 2.2.2 Microfabricated heaters and temperature sensors

Thin film resistors of polysilicon and metal lines are commonly used as heater materials in Si microfabrication. Several temperature sensors have been microfabricated on Si, including metal resistor sensors (Resistive Temperature Devices or RTDs), semiconducting resistors (thermistors), thermocouples and thermopiles, diodes, and transistors [6]. We chose Pt as both the heating and temperature sensing element for the microreactor. Pt is a good heater material due to its high melting point (1755°C) [19] and large electromigration limit due to its high molecular weight [20]. In addition, Pt is a good temperature sensing (RTD) material, because its resistivity changes linearly with temperature over a wide range (0-800°C) [21]. The resistivity changes with temperature

becase of increased electron scattering from the thermally agitated lattice atoms (phonon scattering) [22].

Electrical resistance of 0.1 μm thick Pt (on 10nm Ti adhesion layer) increased linearly with temperature upto 800°C [23], consistent with observations of bulk Pt films [21]. Above 800°C, however, the electrical resistance increased exponentially due to material degradation, placing the upper limit on temperature measurements at 800°C. The electrical resistance can be expressed as,

$$R = R_o \times \left[1 + \alpha(T - T_o)\right] \qquad (2.1)$$

where R is the resistance at temperature T, $R_0$ is the resistance at a reference temperature $T_0$, and $\alpha$ is the temperature coefficient of resistance. The measured temperature coefficient of resistance ($\alpha$) for the thin-film was $2.9\times10^{-3}$/ °C [23], which is slightly lower than the measured value for other thin films ($3\times10^{-3}$/ °C) [11], and is much lower than bulk values of $3.85\times10^{-3}$/ °C [21].

### 2.2.3 Microfabricated Flowsensors

Hot-wire and hot-film anemometry are well established and widely used techniques for flow measurement [1, 24] due to their simplicity and ease of operation. The basic principle of anemometry is to measure the convective flow induced temperature drop of a heated resistor, and calibrate this temperature drop to the flowrate. There are many variations in the way anemometers are configured (single resistor used as heater and temperature sensor or separate heater and temperature sensors [6]); and in the way they are operated (constant-current mode and constant-temperature mode) [24]. Recently, anemometers have been microfabricated on silicon, providing the advantages of low-

power operation, fast time response, and integrated circuitry for improved performance [6, 18]. The microfabricated anemometers typically consist of a thermally isolated microstructure having a central thin-film heater and two temperature sensors placed symmetrically upstream and downstream of the heater. This configuration of separate heaters and temperature sensors has the advantage a single-resistor used as both heater and temperature sensor, of differential measurement, offering lower drift due to ambient temperature and pressure variations. The thermally isolated microstructures that have been fabricated include polysilicon bridges [15], silicon cantilevers, posts and bridges [17, 25, 26], and silicon nitride diaphragms and bridges [11, 27]. The heater material is doped polysilicon [15, 25] or metal. The temperature sensors used include metal resistors (RTDs) [11, 27, 28], thermocouples and thermopiles [25], diodes [17], polysilicon resistor (thermistor) [15]. Although diodes and polysilicon resistors have the advantage of CMOS compatibility, their performance (linearity and sesitivity) is poor compared with RTDs and thermocouples. The Honeywell flow sensor, consisting of Pt heaters and temperature sensors on a SiN microbridge, showed excellent performance (wide dynamic range and high sensitivity) and survived testing in harsh conditions of high temperature (85 °C), high humidity (80%), and dusty environments [11, 29].

The microreactor flowsensor structure adopted in this study resembled the Honeywell design, with Pt heater and temperature sensors deposited on a SiN thermally isolating microstructure. The microreactor flowsensor was, however, designed for time-of-flight mode of operation, where the central heater was pulsed, and the time taken for the heat pulse to be detected upstream and downstream determined the flowrate [6, 26]. In contrast, the Honeywell flowsensor was designed for differential-temperature mode of

operation, where the temperature difference between the upstream and downstream temperature determined the flowrate. The differential-temperature mode of operation requires calibration for individual gases whereas the time-of-flight mode of operation offers the possibility of a universal calibration for all gases.

## 2.3 Microreactor Design

Models of varying degrees of accuracy and difficulty ranging from simple scaling analysis to rigorous 3-D Galerkin Finite Element calculations [2] were implemented to design the microreactor. Since the characteristic dimension of the microreactor was 0.5mm and the microreactor was operated at atmospheric pressures, the Knudsen number is sufficiently small (Kn~ $10^{-4}$) that continuum transport analysis applied to the cases considered in this work. The microreactor designs were evolutionary, with experiments used to validate the models, and the model predictions used to improve the microreactor design. The analytical models and the design constraints for the microreactor are described in this section.

The goal of the design was to obtain dimensions of the microreactor membrane, heater resistor, temperature sensor, and flow sensor. Five major design criteria used that were used for the design:

1) Reactant residence time should be sufficient for reaction,
2) Heat transfer design of the membrane should allow for catalyst heating to ignition temperatures, and simultaneously allowing for heat removal of heat of reaction,

3) Current densities in heater resistor lines should not exceed electromigration limits,

4) The temperature sensors should have sufficient sensitivity (1°C), and

5) Flow sensor should be sensivitive to ~10% variation in operating flowrate.

The reactor design and the resistor design calculations were iterative and are summarized in the flow-chart (Figure 2.3). Reaction engineering scaling analysis was used to determine the required residence time, and the required heat transfer in the microreactor (Section 2.3.1). The heater resistor dimensions were designed to withstand the power required for heating to ignition temperatures without electromigration (Section 2.3.2). The temperature sensor (Section 2.3.3), and the flowsensor (Section 2.3.4) were designed for sufficient sensitivity.

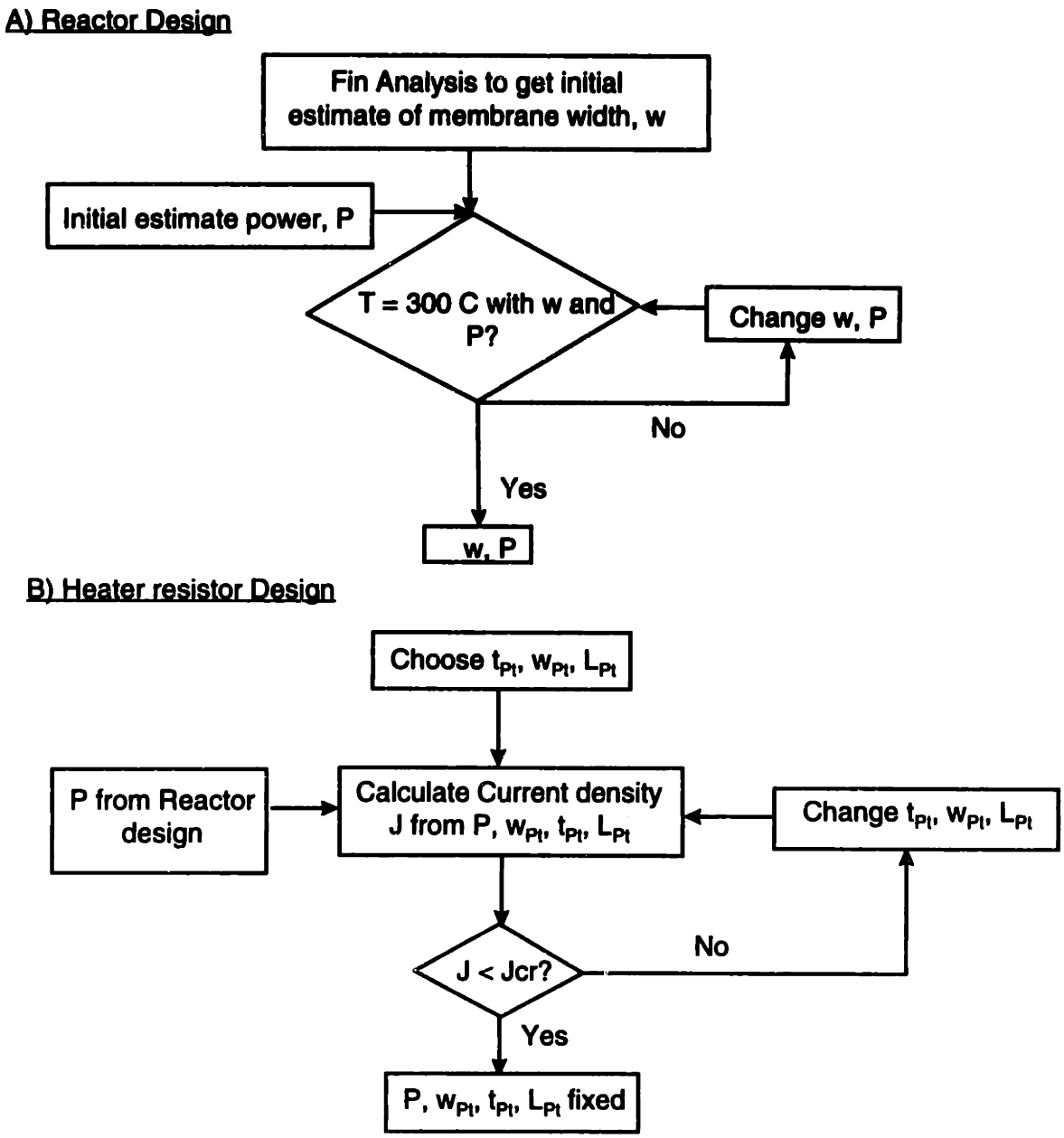


***Figure 2.3** Simplified flow chart of the microreactor design procedure. A) Reactor design calculations to get membrane width, w, and heater power, P. B) Heater resistor calculation to get heater dimensions: Length $L_{Pt}$, width $w_{Pt}$, thickness $t_{Pt}$. J is the current density via the heater.*

### 2.3.1 Reactor Design

The reactor design consisted of two parts:

1) A scaling analysis to determine the rate limiting step for residence time calculation, and

2) Thermal design of the microstructure for efficient catalyst heating, and removal of heat of reaction.

***Residence time calculation***

The residence time was designed to be lower than the characteristic time for the rate limiting step in the reaction. The reactant gases diffuse from the bulk of the gas to the catalyst surface, react on the heated catalyst, and the products diffuse back to the bulk of the gas in the channel, before being convected away from the reaction zone (Figure 2.4). The rate limiting step was determined by comparing the relative time constants (estimated by scaling analysis) of the different reactions. The characteristic reaction time (trxn) is ~1ms for most heterogeneously catalyzed partial oxidation reactions [30]. The characteristic diffusion time varies as ~ $h^2/D$, where h is the characteristic length which in our case is the channel height, and D is the gas diffusivity. Since the channel is formed by etching the bulk of the Si wafer, the channel height is determined by the wafer thickness (h = 550 μm). The characteristic diffusion time is ~$h^2/D = (550\times10^{-6}\ m)^2/(10^{-5}\ m^2/s)$ =30ms, which is much larger than the reaction time of 1ms, indicating that diffusion of reactants to catalyst, is the rate determining step. Therefore, the residence time was designed to be larger than the diffusion time for maximum conversion. The average residence time ($\tau_{res}$) is ~L/v, where L is the length of the reaction zone and v is the average gas velocity in the channel. The residence time in the reaction zone was designed to be ~50ms, and the reaction channel length (L) was designed to be 3.4mm, giving a average gas velocity (v) of ~7cm/s.

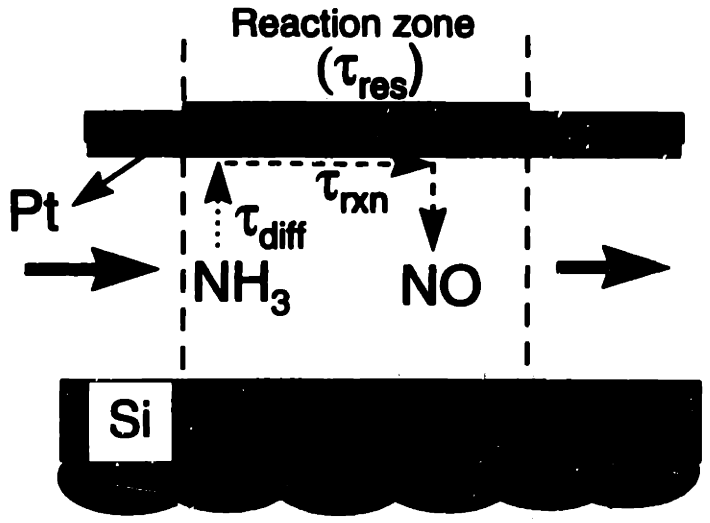


***Figure 2.4** Schematic figure of microreactor cross-section showing the sequence of steps for reaction including diffusion to the catalyst surface reaction and diffusion of products to the bulk of the gas.*

***Thermal Design***

The main mechanism of heat loss from the catalyst was conduction via the SiN membrane to the cold microreactor walls (calculated later in this section). Therefore the design of SiN membrane geometry (w and $w_{fin}$ in Figure 2.5 ) was critical for optimal heat transfer in the microreactor. The SiN membrane thickness was fixed at 1μm (which is relatively high for a CVD film), for structural stability. A narrow membrane width (w) improves heat transfer by providing a shorter conduction path from the heater/catalyst to the cold microreactor walls. In addition, a smaller membrane width also results in lower amount of heat generation because of smaller volumetric throughput of the reactants (Volumetric flowrate $V = v \cdot h \cdot w$. Since $v = 7\frac{cm}{s}$ , fixed by residence time calculation; $h = 550\mu m$, fixed by channel height; smaller w implies smaller V, and thus less heat generated $Q = V \cdot \Delta H_{rxn}$).

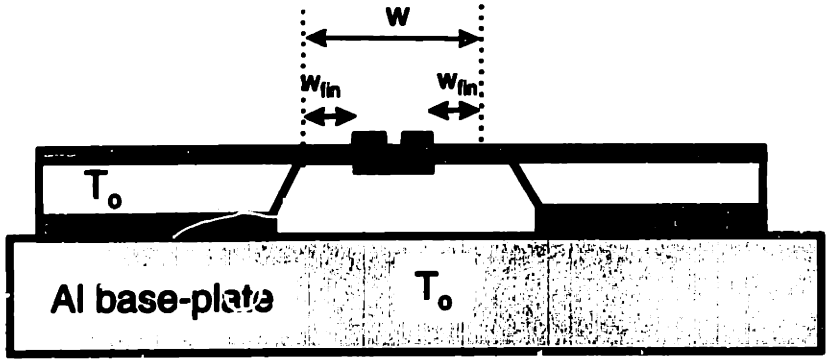


***Figure 2.5** Schematic of the microreactor cross-section showing membrane dimensions used in the heat transfer calculations.*

Since the heater and catalyst are symmetrically placed on the membrane, the heat transfer characteristics of both the heater and the catalyst were assumed to be the same. This resulted in a design trade-off, because the heater resistor required sufficient thermal isolation (larger membrane membrane width) to reach ignition temperatures, whereas control of the exothermic reactions required sufficient heat removal capability from the catalyst (smaller membrane width). The membrane was therefore designed to maximize the amount of heater power required to reach ignition temperatures (~300°C), with the upper limit on the heater power set by the maximum current density that did not cause electromigration of the heater line.

The heater power to be supplied, and the membrane width were iterated to meet the design goal of reaching the ignition temperature (300°C) at the design power (Figure 2.3). A 1-D fin analysis (Appendix A) provided an estimate of the membrane width (w = 500μm), a value that was lower than the characteristic fin length, for better heat transfer. The initial power estimate was obtained from the heat transfer arguments. 1-D heat transfer calculations were then carried out to check if the estimated membrane width and heater power met the design criteria of the microreactor reaching ignition temperatures.

***Estimate of power to be supplied***

Since the heater and the catalyst are symmetrically placed on the SiN membrane, the heat transfer characteristics of the heater and the catalyst were assumed to be the same. If the heater and the catalyst are thermally isolated, ignition temperature could be reached at low heater powers. But, after ignition, the heat of reaction would result in unacceptably high temperature rise. Very good heat conduction out of the catalyst and heater, on the other hand, would require a very large power supply for ignition, which can result in electromigration of the heater lines. The heater power (P) was therefore designed to be of the same order as the heat generated by reaction .

The heat generated by reaction,

$$Q = n \cdot \Delta H_{rxn} = P \qquad (2.2)$$

where $n$ was the molar flowrate, and $\Delta H_{rxn}$ was the heat of reaction.

Using a membrane width ($w$) of 500μm, and the average gas velocity ($v$) of 7cm/s, obtained from the residence time calculation, the typical volumetric flowrate was determined to be ~10sccm. This volumetric flowrate corresponded to a reactant molar flowrate ($n$) of $7.5 \times 10^{-7}$ moles/s in a typical reacting mixture ($NH_3$ or hydrocarbon in $O_2$) that had 10% reactant by volume. Using a representative heat of reaction ($\Delta H_{rxn}$) value of 500kJ/mol (for complete oxidation of $NH_3$ oxidation to $N_2$ and $H_2O$, the heat of reaction is 454kJ), and substituting into equation (2.2),

$$P = 7.5\times10^{-7}\, mol/s \cdot 500\times10^{3}\, J/mol$$

$$P = 0.375W .$$

After a few design iterations, the design power ($P$) chosen for the microreactor was 0.3W.

***Evaluation of estimated of w and P against design criteria***

1-D models of the heat transfer were used to determine if the initial estimate of the heater power ($P$ = 0.3W) supplied to a 500μm wide membrane, would provide a temperature rise of 300°C (ignition temperature). The heater was restricted to the center of the membrane to avoid excessive heat loss to the microreactor walls and efficient use of heater power (Figure 2.5). The heat transfer model was also used to determine $w_{fin}$ (Figure 2.5).

Three modes of heat loss were identified (Figure 2.6) and estimated:

1) Conduction via the membrane to the microreactor walls ($Q_1$),
2) Conduction via the gas in the reaction channel to the bulk Si, ($Q_2$), and
3) Free convection in air above the microreactor ($Q_3$).

Radiation is neglected since the operating temperatures of the microreactor is low (~400°C). Convection in the gas channel was of the same order as conduction due to small channel size and low gas velocities, which resulted in a low heat transfer Peclet number ($Pe = \frac{v \cdot h}{\alpha} = \frac{0.1 \, m/s \cdot 550 \cdot 10^{-6} m}{4 \cdot 10^{-5} \, m^2/s} \approx 1$).

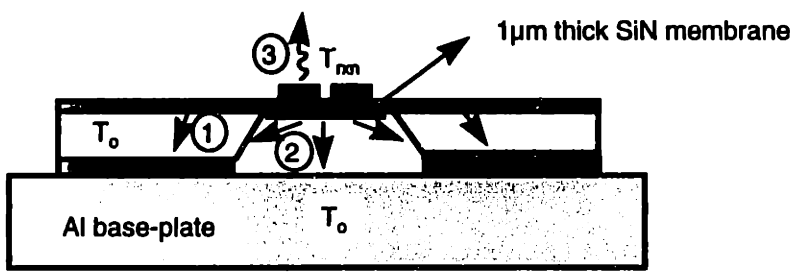

***Figure 2.6** Microreactor schematic cross-section showing the various modes of heat loss- 1) Conduction via SiN membrane, 2) Conduction via air in channel, and 3) Free convection in air.*

Using a 1-D heat conduction equation, the heat removed via the membrane is given by,

$$Q_1 = k_{SiN} \cdot A \cdot \frac{T_{rxn} - T_o}{w_{fin}} \qquad (2.3)$$

Assuming aprori that the heat conduction via membrane is the dominant mode of heat loss (verified later in this section), the heat loss can be equated to the heater power.

$$Q_1 = k_{SiN} \cdot (2 \cdot L \cdot t_{SiN}) \cdot \frac{(T_e - T_o)}{w_{fin}} \approx P \qquad (2.4)$$

where L is the length of the heater segment ($L$= 3.4mm, previously fixed by residence time analysis); $t_{SiN}$ is the membrane thickness ( $t_{SiN}$ =1μm, fixed by structural constraints in the beginning of this section); P is the design heater power ($P$=0.3W, fixed previously in this analysis). Substituting these values into equation 2.4,

$$\Rightarrow Q_1 = 14 \cdot (2 \cdot 3.4 \times 10^{-3} \cdot 1 \times 10^{-6}) \cdot \frac{(300)}{w_{fin}} \approx 0.3$$

$$\therefore \underline{w_{fin} \approx 100\mu m}.$$

Since $w_{fin}$ was chosen to be 100μm for the microreactor design, the heater segment extended to a width of 300μm (Figure 2.5).

The heat conduction calculation also verifies that the chosen design values of w and P could provide a temperature rise of 300°C ( If estimate for w was low for the design P, we would get an absurd value of $w_{fin}$ such that, $2 \cdot w_{fin} \geq w$ ).

The heat transfer via gas conduction in channel (Mode 2),

$$Q_2 = k_{air} \cdot (L \cdot w) \cdot \frac{(T_{max} - T_o)}{H} \qquad (2.5)$$

$$\therefore Q_2 = 0.046 \cdot (3.4\times10^{-3} \cdot 500\times10^{-6}) \cdot \frac{300}{550\times10^{-6}}$$ (all values in S.I. units)

$$\underline{Q_2 = 43mW}.$$

The heat transfer to ambient air via free-convection,

$$Q_3 = h_{air} \cdot (L \cdot w) \cdot (T_{max} - T_o) \qquad (2.6)$$

where $h_{air}$ is the heat transfer coefficient for free convection . $h_{air}$ ~10 SI units, at stagnant conditions [31].

$$\therefore Q_3 = 10 \cdot (3.4\times10^{-3} \cdot 500\times10^{-6}) \cdot 300$$

$$\underline{Q_3 = 5mW}.$$

These calculations also indicate that for the given membrane geometry, the dominant mode of heat loss from the catalyst is via conduction in the membrane ($Q_1$).

### 2.3.2 Heater resistor design

The goal of the resistor design is to obtain the heater resistor dimensions: width $w_{Pt}$, length $L_{Pt}$, and thickness $t_{Pt}$, that can withstand the design heater power (0.3W) without electromigration of the heater lines. Most of the electromigration studies in the have been on Al and Al alloys, while no work has been reported on electromigration of Pt [20]. Electromigration limit increases with molecular weight of the material and also depends on the microstructure of the thin film [20]. Due to the complicated mechanism, a quantitative model to predict electromigration limit with molecular weights has not been

developed. Hence, for the first design, the electromigration limit of Pt ($J_{Pt}$) was assumed to be 10x that of Aluminum ($J_{Al} = 10^5$ A/cm$^2$ [32]). This value ($J_{Pt} > 1 \times 10^6$ A/cm$^2$) was later experimentally verified to be correct (Section 5.1.2, in Figure 5.3, the maximum current density at 2W of power supply was ~9x10$^6$A/cm$^2$ without electromigration ).

A safety factor of 60% was included in the design, and the heater lines were designed to withstand upto 0.5 W of power.

The power, $P$, is given by,

$$P = V \cdot I \tag{2.7}$$

where V is the applied voltage and I is the current in the heater line.

Neglecting temperature effects of electrical resistance, $R$, and using Ohm's law, we get,

$$P = I^2 \cdot R \tag{2.8}$$

where $R$ is the resistance of the heater.

But,

$$I = J \cdot (w_{Pt} \cdot t_{Pt}) \tag{2.9}$$

where $J$ is the current density in the heater line, $w_{Pt}$ and $t_{Pt}$ are the width and thickness of Pt line.

The electrical resistance,

$$R = \frac{\rho \cdot L_{Pt}}{w_{Pt} \cdot t_{Pt}} \tag{2.10}$$

where $\rho$ is the electrical resistivity, $L_{Pt}$ is the length, $w_{Pt}$ is the width, and $t_{Pt}$ is the thickness of the Pt heater line.

Substituting equations 2.9 and 2.10 into equation 2.8,

$$P = J \cdot (w_{Pt} \cdot t_{Pt} \cdot L_{Pt}) \cdot \rho \qquad (2.11)$$

Equation 2.11 suggested that for a given $P$ (0.5W) and $\rho$ (which is a thin-film property), increasing all the three dimensions- $w_{Pt}$, $t_{Pt}$, or $L_{Pt}$ would result in reduced $J$. The constraints on the heater dimensions were:

1) The total dimension of the heater segment was 3.4mm long x 300μm wide,

2) The operating voltage was designed to be 5-15V, and

3) The thickness of Pt was maintained under 0.1μm due to cost considerations.

Equations 2.11 was iteratively solved with the above constraints to obtain the design values:

$L_{Pt}$=11.5mm, $w_{Pt}$= 50μm, and $t_{Pt}$= 0.1μm.

$$\therefore R = \frac{\rho}{t_{Pt}} \cdot \frac{L_{Pt}}{w_{Pt}} = R_s \cdot \frac{L_{Pt}}{w_{Pt}} \qquad (2.12)$$

Substituting $\rho = 10^{-7}\Omega \cdot m$ (at room temperature), and $t_{Pt} = 0.1\mu m$ into equation 2.12,

$$R = \frac{10^{-7}}{0.1 \cdot 10^{-6} m} \cdot \frac{11.5 \cdot 10^{-2} m}{50 \cdot 10^{-6} m}$$

$$\therefore R \approx 1 \frac{\Omega}{square} \cdot 230$$

$$\therefore \underline{R = 230\Omega}.$$

To achieve a total length of 11.5mm for the heater line within the heater area of 3.4mm x 500μm, a meandering heater pattern was adopted (Figure 2.2) .

Equation 2.11 was used to determine the current density to check if it was within the electromigration limit. Subtituting $P$=0.3W, and the value of $\rho$ and the chosen heater dimensions in equation 2.11,

$$J = 9\times10^5 A/cm^2 < J_{cr,Pt}.$$

### 2.3.3 Temperature Sensor Design

Multiple Pt resistor lines present adjacent to the heater in the reaction channel served as the temperature sensors. The goal of the temperature sensor design is to determine the desired resistance value for maximum sensitivity, and to determine sensor dimensions that provide the design resistance value. The electrical resistance-temperature behavior is given by equation 2.1,

$$R = R_o \cdot [1+\alpha \cdot (T - T_o)]$$

where $R$ is the resistance at $T$, $R_o$ is the resistance at $T_o$, and $\alpha$ is the temperature coefficient of resistance. Differentiating the equation gives,

$$\Delta R = R_o \cdot \alpha \cdot \Delta T \qquad (2.13)$$

which indicates that a larger value of $R_o$ results in a larger change in $R$ for a given change in $T$, providing increased sensitivity. The resistance is determined by applying a constant current of 1mA to the sensors and measuring the voltage developed across it (Appendix H). As a design criteria, we chose a 1mV change for 0.5°C. $\alpha$ was determined to be $2.9\times10^{-3}$/°C [23]. Substituting into equation 2.13, we get,

$$1mA \cdot \Delta R = 1mV = 1mA \cdot R_o \cdot \alpha \cdot \Delta T$$

or,

$$1mV = 1mA \cdot R_o \cdot {}^{2.9}/_{100} \cdot 0.5$$

$$\therefore R_0 \approx 70\Omega.$$

We chose $\underline{R_o = 300\Omega}$ for higher sensitivity.

The upper limit on the value for $R_o$ is dictated by the maximum temperature to be measured, and the maximum voltage that can be read by the data acquisition card (15V).

For a given $R_o$, the voltage generated at sufficiently large temperatures will exceed 15V and saturate the data acquisition card. The maximum temperature that can be measured with $R_o$= 300Ω is 1100°C.

The temperature sensor dimensions were calculated to yield $R_o$=300Ω.

The resistance is given by equation 2.10,

$$R = \frac{\rho \cdot L_{Pt,T}}{w_{Pt,T} \cdot t_{Pt,T}}$$

where $L_{Pt,T}$, $w_{Pt,T}$, and $t_{Pt,T}$ are the length, width, and thickness of the temperature sensor resistor line respectively. The line thickness $t_{Pt,T}$ is fixed by the heater resistor design at 0.1μm.

$$\therefore R_o = \frac{\rho(T_o)}{t_{Pt,T}} \cdot \frac{L_{Pt,T}}{w_{Pt,T}} = 1\frac{\Omega}{square} \cdot \frac{L_{Pt,T}}{w_{Pt,T}} = 300\Omega$$

$$\Rightarrow \frac{L_{Pt,T}}{w_{Pt,T}} = 300.$$

$L_{Pt,T}$ and $w_{Pt,T}$ were designed to be small for localized temperature measurements. Therefore, $w_{Pt,T}$ was chosen to be the minimum linewidth (10 μm) of the mask (for ease of fabrication ). The sensor length, $L_{Pt,T}$ was therefore 3mm.

### 2.3.4 Flowsensor Design

The flowsensor consisted of a central heater and two temperature sensors present upstram and downstream of the heater (Figure 2.7). The flowsensor was designed for a time-of-flight mode of operation (Section 2.2.3), which has the advantage of not requiring calibration for different gases. A transient heat transfer scaling analysis was performed to

decide the placement of the temperature sensors with respect to the heaters (*d* in Figure 2.7) for maximum flowrate sensitivity.

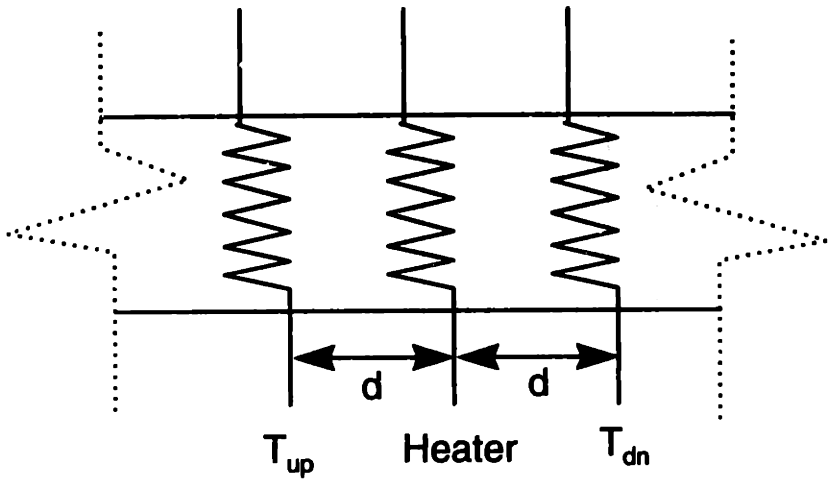


***Figure 2.7** Schematic of flowsensor showing heater and temperature sensor spacing used in sensor design.*

After the heater was pulsed, heat transfer occurred both by convection, as well as conduction via air and membrane. While the conduction heat transfer was isotropic and caused the temperature pulse to reach simultaneously upstream and downstream, convection heat transfer caused the pulse to reach downstream quicker than upstream. The design goal to increase the effect of convection to maximize the time difference between the heat pulse detection upstream and downstream, was achieved by estimating and comparing the characteristic convection time ($\tau_{conv}$) and characteristic conduction times ($\tau_{cond}$).

The characteristic conduction time,

$$\tau_{conv} \approx \frac{d}{v} \tag{2.14}$$

where $v$ was the average gas velocity.

The characteristic conduction time,

$$\tau_{cond} \approx \frac{d^2}{\alpha} \tag{2.15}$$

where $\alpha$ was the thermal diffusivity.

These equations showed that while the convection time scaled linearly with the heater-sensor distance ($d$), the conduction time scaled to the second power of the heater-sensor distance. The convection time was designed to be much shorter than the conduction time, to make convection the dominant mode of heat transfer.

$i.e., \tau_{cond} >> \tau_{conv}$

$$\Rightarrow \frac{d^2}{\alpha} >> \frac{d}{v} \tag{2.16}$$

Since conduction occurred both via the gas and the SiN membrane, comparison of $\alpha$ was used to determined the dominant mode of conduction.

The thermal diffusivity of SiN ($\alpha_{SiN} = 10^{-6}\frac{m^2}{s}$) was much higher than the thermal diffusivity of air ($\alpha_{air} = 4 \cdot 10^{-5}\frac{m^2}{s}$), indicating that the heat pulse was be conducted much faster via SiN membrane than via air. Therefore $\alpha_{SiN}$ was used in equation 2.16 for the flowsensor design, which gave us,

$$\frac{d^2}{\alpha_{SiN}} >> \frac{d}{v}$$

$$\Rightarrow d >> \frac{\alpha_{SiN}}{v} \tag{2.18}$$

Substituting the desired flow velocity sensitivity of 1cm/s (corresponding to a flowrate sensitivity of 1sccm) into equation 2.18,

$$d >> \frac{\alpha_{SiN}}{v} = \frac{10^{-6}\, m^2/s}{0.01\, m/s} = 10^{-4} m.$$

For our design, we chose $d=5\times10^{-4}$m.

## 2.4 Fabrication procedure

The microreactor was fabricated in a two mask (+1 shadow mask) process using bulk micromachining technology. The starting material for the μ-reactor fabrication (Figure 3) was a double-side polished (100 mm diameter, 550 μm thick) silicon wafer. The wafer was coated by low pressure chemical vapor deposition (LPCVD) with 1 μm thick low-stress silicon nitride (SiN) [33]. The deposit on the frontside of the wafer eventually formed the capping membrane of the microreactor (Figure 2.8). The SiN on the backside of the wafer was patterned using photoresist, and plasma etched (in $SF_6$) using the photoresist as the mask, to expose the underlying silicon in the T-shaped channel regions (step 3). The etch termination was timed, with the time previously determined using dummy runs. Overetching by ~1μm was acceptable in this step since the microreactor channel dimensions, that are being defined in this step, are large (500μm).

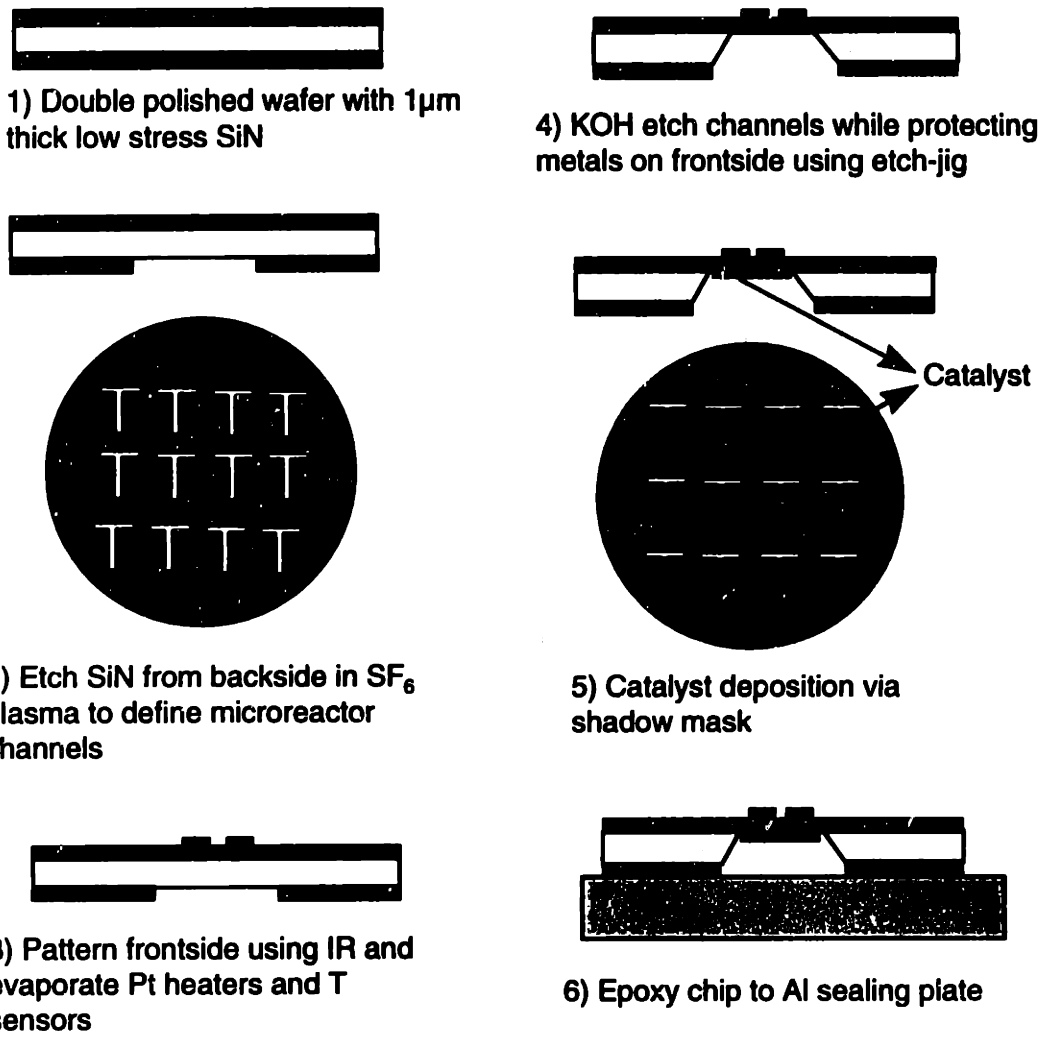


***Figure 2.8** Fabrication process flow for the microreactor.*

In the next step, the frontside of the wafer was coated with image reversal resist for metal deposition, and patterned after alignment to the T-shaped channels on the backside of the wafer (the backside to frontside alignment through the Si wafer was achieved using infrared light). The frontside of the wafer was then coated with 0.1 μm Pt (with 10 nm Ti as an adhesion layer) by electron-beam evaporation, and patterned using metal lift-off (in acetone using an ultrasonic bath) to form the metal heaters, and temperature and flow sensors (step 4). The gas flow channels were then formed by etching bulk of the silicon

(exposed on the backside of the wafer) in KOH solution (20% by weight in water at 90°C). KOH anisotropically etches Si along <111> planes, thus forming channels that are trapezoidal in cross section (Figures 2 and 3). Since SiN is not attacked by KOH, the etch terminates on the SiN on the frontside of the wafer, thus forming the SiN capping membrane (step 5). A custom built Poly-Tetra-Flouro-Ethylene ('teflon') sealing assembly (fabricated at DuPont, courtesy of J. Ashmead and J.F. Ryley) was used to protect the Pt on the frontside of the wafer from KOH during this etch. The wafer was carefully handled in the subsequent processing steps as the microreactor membranes were fragile.

The catalyst was selectively deposited in the reaction channel under the heaters using a shadow mask (step 6) that was aligned and epoxied to the wafer. The wafers were aligned and contacted in a mask aligner using a custom-built alignment setup. Ultra-violet (uv) curable epoxy (Norland Optical Adhesive (#81), Norland Products Inc., New Brunswick, NJ 08902) was dabbed using a cotton swab in the four epoxy holes in the microreactor wafer (Appendix B, Figure B.2), and cured after 1 minute uv exposure (longer exposure makes subsequent wafer separation harder, shorter exposures resulted in insufficient curing). After the cure, the microreactor wafer and shadow mask stayed aligned during handling. They wafers were transferred to the electron-beam evaporation vacuum chamber for catalyst deposition. A 0.1 μm thick platinum catalyst (on 10 nm Ti) film was selectively deposited on the silicon nitride membrane in the reaction channel by electron-beam evaporation via the shadow mask (step 6). The shadow mask was separated from the device wafer after a two hour acetone soak. In some cases, a razor-blade was used as a wedge after the acetone soak to separate the wafers. The shadow

mask was reused after cleaning in 3:1 mixture of $H_2SO_4$ and $H_2O_2$ to remove residual uv epoxy.

The wafer was then diced into 12 individual chips, and each chip was visually aligned and epoxied to an aluminum base-plate with 3 gas inlet-outlet holes (step 7). The aluminum base-plate was custom-machined at MIT (drawings in Appendix D). Cyano-acrylate epoxy ('super-glue') as well as vacuum grease (Dow-Corning High Vacuum Grease, Dow Corning Corporation, Midland, MI 48640) were successfully used for the attachment..

After being released in step 4, the SiN membranes broke during subsequent processing steps, possibly due to stress concentrations at sharp corners. The largest number of breakages were in the die-saw step, and the overall yield of the process was ~70%. Thicker membranes were more robust.

***Shadow Mask Fabrication***

The shadow mask was a silicon wafer with etched slots. The fabrication of the shadow mask was similar to the microreactor fabrication procedure (Figure2.9). The starting material was a double side polished Si wafer coated with 1500Å thick low-stress SiN that served as the etch mask. The backside of the wafer was patterned to define the shadow-mask slots, and etched in $SF_6$ plasma to expose the underlying Si. The shadow mask slots were formed by etching the bulk of the Si in the exposed regions in 20% KOH solution at 90°C. The SiN was then removed in hot phosphoric acid (at 185°C) to form the Si shadow mask.

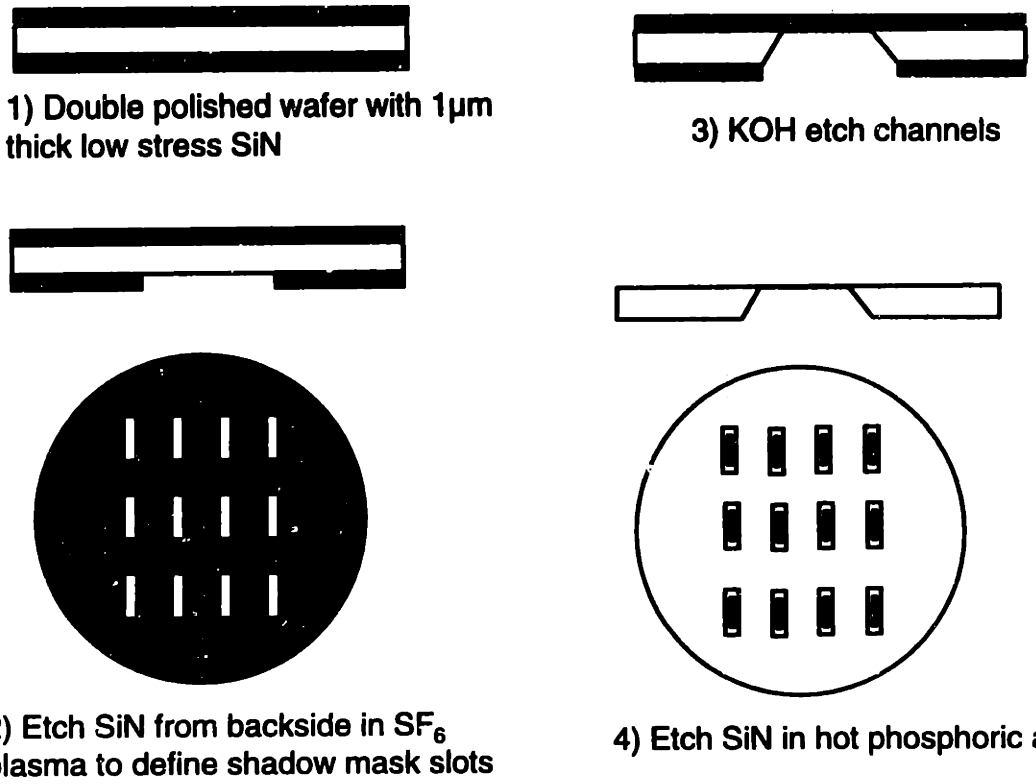


***Figure 2.9** Fabrication procedure for shadow mask.*

## References

[1] E. O. Doebelin, Measurement Systems: Application and Design, 4th ed. New York: McGraw-Hill Inc., 1990.

[2] I.-M. Hsing, "Simulation strategies for microfabricated chemical systems," Ph.D. thesis in Chemical Engineering. Cambridge, MA: Massachusetts Institute of Technology, 1997.

[3] R. E. Cavicchi, J. S. Suehle, K. G. Kreider, M. Gaitan, and P. Chaparala, "Fast temperature programmed sensing for micro-hotplate gas sensors," IEEE Electron Devices Letters, vol. 16, pp. 286-288, 1995.

[4] M. A. Huff, S. D. Senturia, and R. T. Howe, "A thermally isolated microstructure suitable for gas sensing applications," presented at Solid-State Sensor and Actuator Workshop, 1988.

[5] N. Najafi, K. D. Wise, and J. W. Schwank, "A micromachined ultra-thin-film gas detector," IEEE Transactions on Electron Devices, vol. 41, pp. 1770-1777, 1994.

[6] J. W. Gardner, Microsensors: Principles and Applications. New York: John Wiley and Sons, 1994.

[7] M. Parameswaran, A. M. Robinson, D. L. Blackburn, M. Gaitin, and J. Geist, "Micromachined thermal radiation emitter from a commercial CMOS process," IEEE Electron Device Letters, vol. 12, pp. 57-59, 1991.

[8] R. Lenggenhager, H. Baltes, and T. Elbel, "Thermoelectric infrared sensors in CMOS technology," Sensors and Actuators A, vol. 37-38, pp. 216-220, 1993.

[9] I. H. Choi and K. D. Wise, "A silicon-thermopile-based infrared sensing array for use in automated manufacturing," IEEE Transactions on Electron Devices, vol. ED-33, pp. 72-79, 1986.

[10] P. W. Barth, "Silicon microvalves for gas flow control," presented at The 8th International Conference on Solid-State Sensors and Actuators, Stockholm, Sweden, 1995.

[11] T. R. Ohnstein, R. G. Johnson, R. E. Higashi, D. W. Burns, J. O. Holmen, E. A. Satren, G. M. Johnson, R. E. Bicking, and S. D. Johnson, "Environmentally rugged, wide dynamic range microstructure airflow sensor," presented at Solid-State Sensor and Actuator Workshop, Hilton Head, SC, 1990.

[12] O. Tabata, "Fast-response silicon flow sensor with on-chip fluid temperature sensing elements," IEEE Transactions on Electron Devices, vol. ED-33, pp. 361-365, 1986.

[13] P. M. Sarro and A. W. v. Herwaarden, "A silicon-silicon nitride membrane formation process for smart thermal sensors," Sensors and Actuators A, vol. 41-42, pp. 666-671, 1994.

[14] N. R. Swart and A. Nathan, "Reliability study of polysilicon for microhotplates," presented at Solid-state Sensor and Actuator Workshop, Hilton Head, SC, 1994.

[15] Y.-C. Tai and R. S. Muller, "Lightly doped polysilicon bridge as an anemometer," presented at The 4th International Conference on Solid-State Sensors and Actuators, Tokyo, Japan, 1987.

[16] M. Parameswaran, H. P. Baltes, L. Ristic, A. C. Dhaded, and A. M. Robinson, "A new approach for the fabrication of micromechanical structures," Sensors and Actuators, vol. 19, pp. 289-307, 1989.

[17] G. N. Stemme, "A monolithic gas flow sensor with polyimide as thermal insulator," IEEE Transactions on Electron Devices, vol. ED-33, pp. 1470-1474, 1986.

[18] S. M. Sze, "Semiconductor Sensors," . New York: John Wiley and Sons, 1994.

[19] R. H. Perry and D. Green, "Perry's Chemical Engineer's Handbook," . New York: McGrawHill Inc., 1984.

[20] C. V. Thompson and J. R. Lloyd, "Electromigration and I.C. interconnects," MRS bulletin, vol. 18, No.12, pp.19-25, 1993.

[21] Omega Technologies, "The Temperature Handbook," , vol. 28, 1992.

[22] C. Kittel, Introduction to Soild State Physics, 6 ed. New York: John Wiley and Sons, 1986.

[23] S. L. Firebaugh, K. F. Jensen, and M. A. Schmidt, "Investigation of high temperature degradation of Pt thin films with an in-situ resistance measurement apparatus," Journal of MicroElectroMechanical Systems.

[24] R. F. Blackwelder, Hot-wire and hot-film anemometers, vol. 18A. New York: Academic Press, 1981.

[25] F. Mayer, O. Paul, and H. Baltes, "Influence of design geometry and packaging on the response of thermal CMOS flow sensors," presented at The 7th International Conference on Solid-State Sensors and Actuators, Stockholm, Sweden, 1995.

[26] J. Branebjerg, O. S. Jensen, N. G. Laursen, O. Leistiko, and H. Soeberg, "A micromachined flow sensor for measuring small liquid flows," presented at The 6th International Conference on Solid-State Sensors and Actuators, 1991.

[27] L. Qiu and E. Obermeier, "A microsensor with integrated heat sink and flow guide for gas flow sensing applications," presented at The 7th International Conference on Solid-State Sensors and Actuators, Stockholm, Sweden, 1995.

[28] K. Peterson, J. Brown, and W. Renken, "High-precision, high-performance mass-flow sensor with integrted laminar flow micro-channels," presented at The 3rd International Conference on Solid-State Sensors and Actuators, U.S.A, 1985.

[29] R. G. Johnson and R. E. Higashi, "A highly sensitive silicon chip microtransducer for air flow and differential pressure sensing applications," Sensors and Actuators, vol. 11, pp. 63-72, 1987.

[30] C. N. Satterfield, Heterogeneous Catalysis in Industrial Practice, 2nd ed. New York: McGraw-Hill Inc., 1991.

[31] J. P. Holman, Heat Transfer, 7 ed. New York: McGraw Hill, 1990.

[32] S. K. Ghandhi, VLSI fabrication principles. New York: John Wiley and Sons, 1983.

[33] M. Sekimoto, H. Yoshihara, and T. Ohkubo, "Silicon nitride single-layer x-ray mask," Journal of Vacuum Science and Technology, vol. 21, pp. 1017-1021, 1982.

# Chapter 3 Experimental Test Setup

The small size of the microreactor required non-standard, custom-built packaging techniques to supply reactants and detect products (fluid interface), and to supply electrical power and collect sensor output (electrical interface). The package was designed for quick and flexible testing and for easy replacement of degraded or broken microreactors. The fluid interface, electrical interface, detection system, experimental procedure, and sources of error are described in this chapter.

## 3.1 Fluid interface

Reactants were delivered to the microreactor from external gas cylinders with pressure regulators using 1/16" stainless steel piping (Figure 3.1). External mass flow controllers (Unit Instruments UFC 1100, 0-20sccm for $NH_3$ and 0-100sccm for $O_2$) were used to maintain the desired gas flowrates. A custom-built gas feedthrough Al block was used to feed reactants from the external piping into the microreactor. The Al block had inlet and outlet holes that were connected to external pipes using 1/16" Swagelock® fittings. The outlet and two inlet holes of the microreactor were aligned to the corresponding holes in the Al block, and compression sealed using o-rings. The Al block also had a cartridge heater to maintain the microreactor at ~150°C to prevent condensation of water produced in reactions. The detailed drawings of the Al block are included in Appendix E.

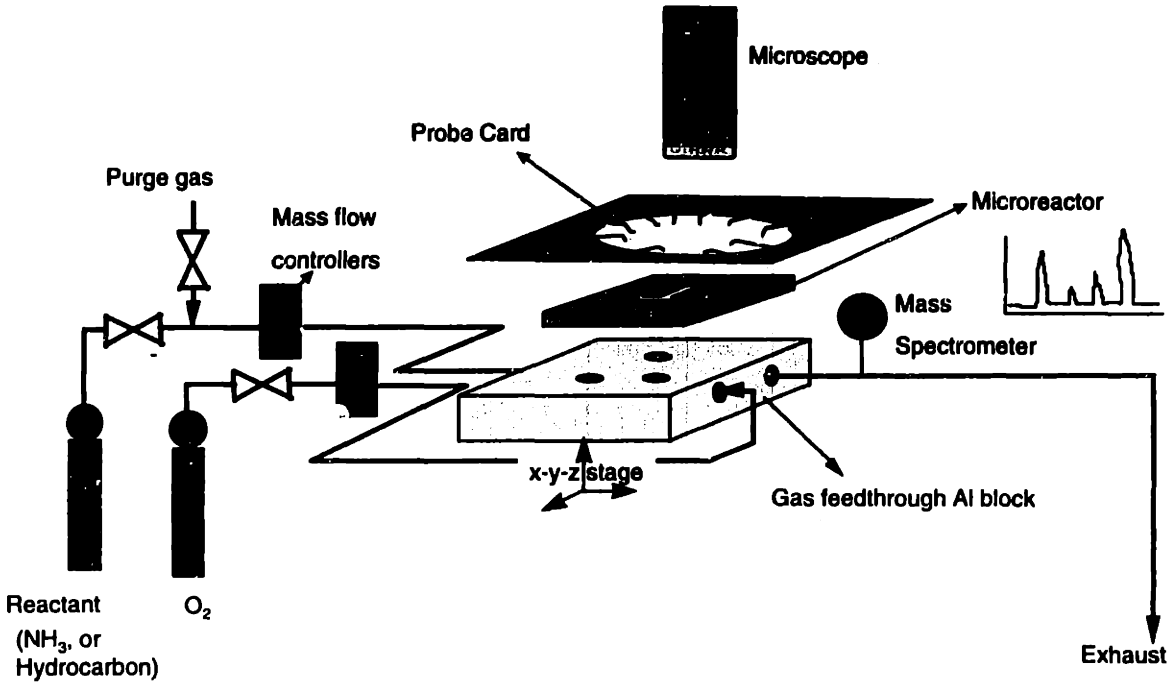


***Figure 3.1*** *Schematic of experimental test setup*

The microreactor exhaust composition was continuously monitored using a quadrupole mass spectrometer. Because of the small volumetric throughput of the microreactor (~10 sccm), care was taken to minimize any dead volumes between the microreactor and the mass spectrometer to prevent signal delays and signal convolutions due to gas mixing. Since conventional leak-valves have large dead-volumes, a 3.8 cm long, 15 μm i.d. fused silica capillary epoxied to the gas exhaust tube, was used to dose gases from the exhaust tubing (760 torr) into the mass spectrometer chamber (which was maintained at $1\times10^{-5}$ torr) (Figure 3.2). The fabrication procedure and detailed drawings of the capillary doser are in Appendix F. The doser periodically clogged (~30min of $NH_3$ oxidation) due to $H_2O$ condensation in the capillary and therefore needed to be replaced.

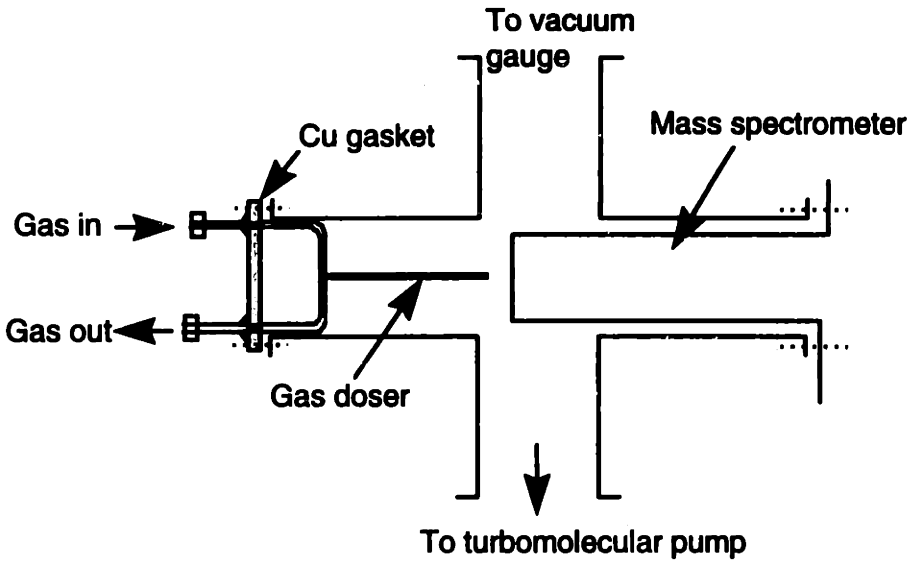


***Figure 3.2** Schematic of gas detection system including doser and mass spectrometer. The detailed drawing of the doser are in AppendixF.*

### 3.2 Electrical Interface

Electrical connections to the on-chip bond-pads of the heaters and sensors were made using a custom fabricated probe-card ( Built by Alphatronics Engineering Corporation, 154 Talamine Court, Colorado Springs, CO 80907). The probe-card was mounted in a probe-card holder (also built by Alphatronics Engineering Corporation), and was plugged into an edge-connector for power supply and sensor readout. The microreactor bond pads were aligned and contacted to the tungsten probes of the probe-card using an x-y-z-stage, a microscope (11cm working distance, 6μm resolution, Moritex), and a CCD camera. The probe-card design allowed quick and flexible testing by simply replacing the degraded or broken microreactor with a fresh microreactor, eliminating the need for time-consuming and involved wire-bond packaging of every microreactor. The microscope and CCD camera were mounted on a x-y stage to view different regions of the microreactor.

Virtual Instruments (VI's) were written on PC-based Labview software (National Instruments) to collect temperature sensor readings (RTDs), and heater power data. To obtain the electrical resistance of the RTD, a signal conditioning board (National Instruments SC-2042-RTD) supplied a constant current (I=1mA) to the RTDs, and the voltage across the RTD was read in a differential mode by the data-acquisition board (National Instruments AT-MIO-64E-3), to give the resistance (R=V/I). VI software converted resistance to temperature reading using the previously generated calibration curve (Equation 2.1), and the temperature readings were written into an Excel spreadsheet file. A constant current power supply (DuPont power supply custom built by Mark Wetzel) was used in this study. The power supply circuit also provided linearly scaled ( 0-5V) output for both voltage and current data, which was read into the data acquisition board for heater power measurement.

***Temperature error in the experiments***

The voltage resolution of the data acquisition card (12 bit) determined the temperature resolution of the experiments. With the maximum measurable voltage set at 15V for the data acquisition card, the temperature resolution for all the experiments was 0.5°C (detailed calculation in Appendix H), unless specified otherwise.

### 3.3 Mass spectrometer calibrations

A quadrupole mass spectrometer (Balzers QMA120) was used to determine exhaust composition. The mass spectrometer calibration procedure and strategies to get accurate concentration data with minimum effect of drift, are described in this section.

The mass spectrometer peak heights drifted primarily due to temperature variations. The mass spectrometer was run for ~1 hour before collecting data to obtain a stable

temperature and relatively constant peak heights. The large drift upon start up was due to ambient heating caused by the mass spectrometer thermal ionizer. The measured temperature rise of the walls of the vacuum chamber due to the ionizer was ~60°C.

It was observed that although the peak heights drifted with time, all the peaks drifted uniformly so that a constant peak height ratio was maintained for a given composition. This allowed comparisons of peak heights normalized to a standard peak across different runs, and more importantly, it allowed the use of a single calibration using normalized peak heights for a long period of time (~months). Gas peak heights were calibrated as a function of the volumetric gas composition using gas-$O_2$ mixtures (Appendix G and figures therein). To get drift-independent calibration curves, the peak heights were normalized using 100% $O_2$ peak height. It was observed that the normalized peak heights varied linearly with composition (within experimental error), which simplified the use of the calibration curves.

For a given chamber pressure, the gas peak height was solely a function of gas concentration and was not changed by the composition of the rest of the gases that made up the mixture. For example, at a given chamber pressure, the $NH_3$ peak height in 10% $NH_3$ in Ar mixture (by volume) was the same as $NH_3$ peak height in 10% $NH_3$ in $O_2$ mixture. In some cases, the chamber pressure changed as the gas mixture changed because of differences in pumping efficiencies of the turbomolecular pump for different gases [1], which changed the absolute peak heights of the gases also. For $NH_3$ oxidation reaction, chamber pressure remained constant. Since the peak height was uniquely determined by gas concentration, the calibrations could be used to determine the composition of reaction products that contained several different gases.

$NH_3$ calibration curve was only used as a reference to check the mass spectrometer setting, and was not used in concentration measurements. For higher accuracy, $NH_3$ concentration was determined by calibrating immediately prior to, and immediately after a reaction. The typical experimental sequence is illustrated in Figure 3.3. The $NH_3$ peak height was assumed to be linear with composition (verified previously, Appendix G, Figure G.1). The drift in the mass spectrometer in the two calibration ($\Delta$) was reported as the experimental uncertainty and plotted as the error bar in conversion data. Sample calculations showing the procedure for determining the error are shown in Appendix H. Since this calibration procedure was difficult to carry out for each of the individual reaction products for each run, the calibration curves (Appendix G and figures therein) were used to determine the concentration of the other gases.

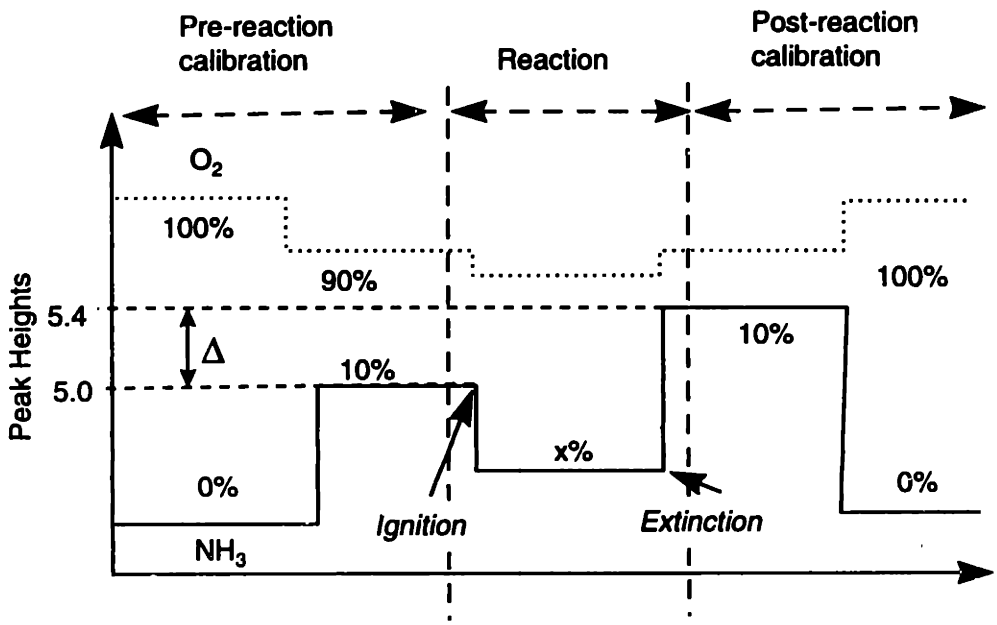


***Figure 3.3*** *Schematic of typical experimental sequence (in this case 10% $NH_3$ in $O_2$ reaction) showing $NH_3$ calibration steps. The $NH_3$ peak height difference before and after reaction ($\Delta$) is the due to the mass spectrometer drift and it determines the error bar of the data (Appendix H).*

### 3.4 Experimental Procedure for Reactions

An experimental protocol, which included a procedure to check for feed composition, a consistent catalyst activation process, and calibrations to account for mass spectrometer drifts, was developed to obtain accurate and consistent results.

***Feed composition check***

This test ensured proper mounting of microreactor on gas feedthrough Al block to prevent gas leaks that could change feed composition. Before mounting the microreactor, a fixed feed composition (e.g., 50% $NH_3$ in $O_2$) was mixed and fed to the mass-spectrometer using a Swagelock® Tee-fitting that bypassed the gas feedthrough Al block-microreactor assembly. The ratio of the measured reactant mass spectrometer peak heights (at mass number 17 for $NH_3$ and 32 for $O_2$) was used as a standard (Tee-standard) for gas leak checks. The microreactor was then mounted, and the peak heights of the reactants at the same composition (50% $NH_3$ in $O_2$ in this example) were measured. The peak height ratios with the microreactor and the Tee-standard should be the same in the case of constant feed composition without gas leaks (the absolute peak heights need not be the same because of mass spectrometer drifts). A drawback of this technique is that while it ensures consistent feed composition between the mass flow controller readings and the microreactor, it does not work if there are equal leaks of *both* gases which would also give the same composition but have different total flowrate than the mass flow controller setting. While the equal leak of both gases is unlikely, a better test would be to measure the total flowrate of the microreactor exhaust in addition to the constant composition check.

***Check for electrical connections***

After contacting the microreactor to the probe card, electrical interconnections are checked by passing a constant current through the heaters and temperature sensors, and determining if the measured voltage gives a reasonable resistance value. The temperature sensor base resistances ($R_0$) are then recorded at room temperature. In the cases where $H_2O$ is one of the known products of the reaction, the gas feedthrough Al block and the microreactor are then heated to ~150°C, as measured by the on-chip temperature sensor (The Al block temperature is higher than the microreactor temperature by ~30°C because of the air gap between the block and the microreactor due to the o-rings ).

***Catalyst activation***

The catalyst activity is known to change for many reactions over time [2].Therefore a consistent activation procedure was necessary to compare conversion and selectivity across many microreactors. In the case of $NH_3$ oxidation, Pt catalyst in microreactors undergoes etching (Section 4.4; Figure 4.16), resulting in increased catalyst surface area, and possibly, increased activity. The catalyst etching and restructuring phenomena is also observed in conventional Pt gauze catalysts[3]. The microreactor catalyst activation procedure for $NH_3$ oxidation is described next.

The catalyst was heated in an $O_2$ ambient at ~350°C for ~0.5 hours using the on-chip heaters. This procedure oxidized carbonaceous contaminants from the catalyst surface, and possibly, formed a thin film of $PtO_2$ on the surface. Next, $NH_3$ in $O_2$ mixture (typically ~10% $NH_3$) was ignited and reacted for ~20min at high flowrates (50sccm), with the power adjusted such that the whole heater length is at ~350°C. The high flowrates were necessary for uniform activation of catalyst segment since the downstream catalyst segments otherwise remained inactive at low flowrates because of

reactant depletion (Section 4.3.1). It was observed that first ignition temperature was usually high (~300 °C) and inconsistent, while subsequent ignitions occurred repeatably at temperatures ~200°C.

Following these checks and activation steps, reactions were carried out. The reactant and product peak heights were recorded during the course of the reaction, and was later used to obtain exhaust composition data with the previously generated calibration curves (Section 3.3).

## References


[1] O'Hanlon, *A Users Guide to Vacuum Technology,* 2nd ed. New York: John Wiley and Sons, 1989.

[2] M. V. Twigg, "Catalyst Handbook," . England: Wolfe Publ. Ltd., 1989.

[3] C. N. Satterfield, *Heterogeneous Catalysis in Industrial Practice*, 2nd ed. New York: McGraw-Hill Inc., 1991.

# Chapter 4 Silicon Nitride Microreactor Test Results

Test results of the silicion nitride (SiN) microreactor, including flowsensor characterization, reaction channel heat transfer behavior, and partial oxidation reactions are described in this chapter. Ammonia oxidation reaction was used as the model partial oxidation reaction. Ignition-extinction behavior, conversion-selectivity issues, and materials stability isssues were explored.

## 4.1 Flowsensor Testing

The flowsensor consisted of a central heater and two temperature sensors- one each present upstream and downstream of the heater (Section 2.2.3; Figures 2.7 and 4.1). The flowsensor was tested in a differential temperature mode of operation, where a fixed power was applied to the central heater resistor, and the convective flow induced temperature difference between the upstream and downstream sensors was measured. The flowsensor was tested in $O_2$ flow (Figure 4.1), and the flowrates were maintained using external mass flow controllers (Unit Instruments, UFC 1100). The resolution of the mass flow controller (1% of full scale = 1sccm) is plotted as the x-axis error-bar. The voltage resolution of the A/D card (12-bit card) which translates to a temperature resolution of 3°C (1.5°C for each sensor) is plotted as the y-axis error bar (equations used for converting voltage to temperature readings in Appendix H).

Although the flowsensor was designed to operate in a time-of-flight mode (Section 2.3.4), the measurements were obtained in a differential temperature mode of operation to simplify the required measurement electronics. While the differential temperature mode

of operation required steady heating of the central resistor and measurement of temperature, the time-of-flight mode required electronics to pulse the central heater and detect the time taken for the hot pulse to travel up and downstream. The flowsensor calibration (Figure 4.1) showed that the resolution decreased with increasing flowrates because both the upstream and downstream temperatures saturated at high flowrates, consistent with other micromachined flowsensor studies[1]. At an applied power of 20mW to the heater, the upstream temperature reached room temperature at flowrates larger than ~30sccm (within a temperature resolution of 1.5°C), and the downstream temperature saturated at 48°C at 60sccm flowrate. The flowsensor range could be increased by operating at higher powers. A design change that would improve resolution for the differential temperature mode is to place the temperature sensors as close to the heaters as possible, since the temperature change decreases with increasing distance from the heater.

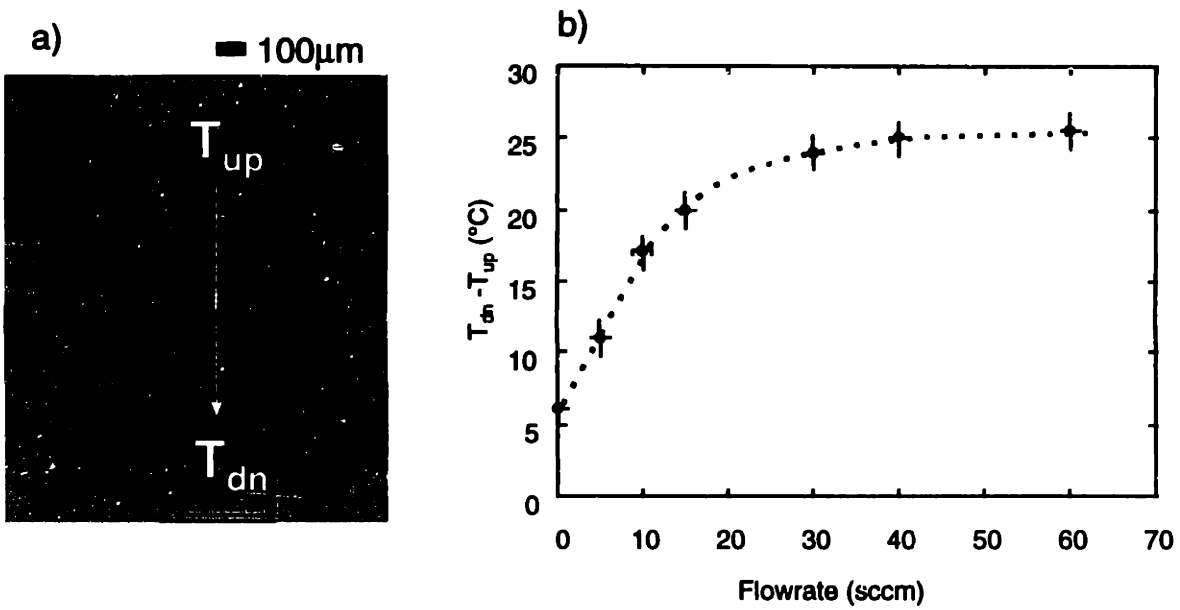


***Figure 4.1** a) Photomicrograph of the flow sensor. b) Calibration of the flowsensor in $O_2$. The temperature difference is not 0 at 0 flow due to the asymmetry in the upstream and downstream temperature sensors.*

A disadvantage of operating in the differential temperature mode is the need for calibrating the flowsensor for different gases. The time-of-flight mode has the advantage of requiring only a single calibration for all gases because this technique relies on flow velocity measurement, which does not dependent on the thermal characteristics of the gas.

### 4.2 Temperature profiles in inert gas environment

Experiments and simulations were carried out to determine the temperature profiles in the microreactor in inert gas flow. At a given flowrate of inert gas ($O_2$), power was supplied to the heater segment 4 (Figure 2.1), and the temperature monitored using the on-chip temperature sensors adjacent to the heater segment (see, *e.g.*, Figure 4.2). Each temperature sensor was geometrically identical and provided spatially averaged (650 μm×250 μm) temperature measurements.

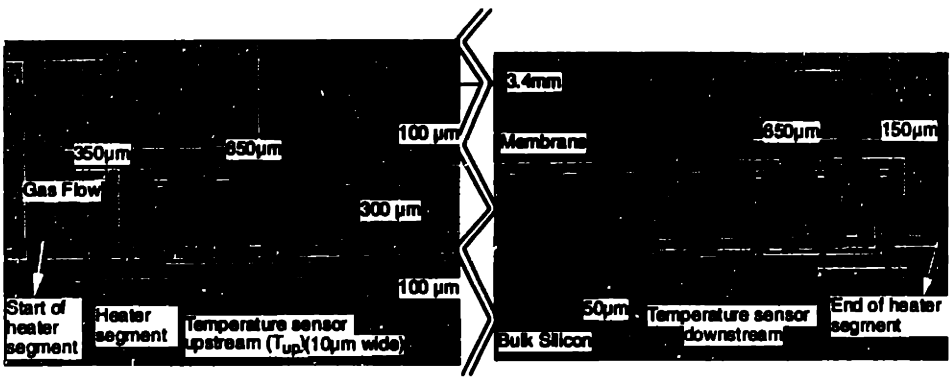


***Figure 4.2** Photomicrograph of heater #3 showing the heater and temperature sensors along with the relevant dimensions.*

Experiments showed that the temperature profile was uniform to within 10% along the axis of the heater (Figure 4.3), with a sharp fall off outside the heater segment. The temperature drops to less than 10% of the maximum at an axial distance of 700 μm from

temperature drops to less than 10% of the maximum at an axial distance of 700 μm from the edge of the heater segment, and to room temperature 1700 μm from the heater edge. The temperature resolution was ±0.5°C (the error-bars were smaller than the data points). The sharp axial fall off in temperature has been verified by three-dimensional finite element simulations (Figure 4.4) [2].

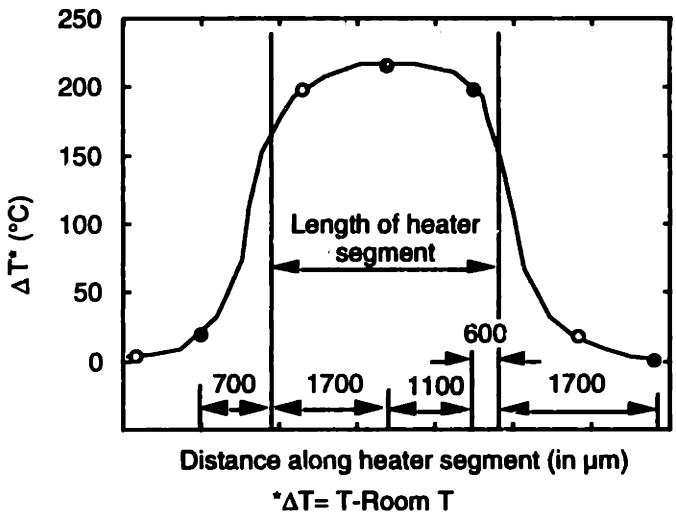


***Figure 4.3*** *Experimentally determined axial temperature profile showing the uniform temperature in the heater segment, and sharp fall-off outside the heater segment. The temperature resolution is ± 5°C.*

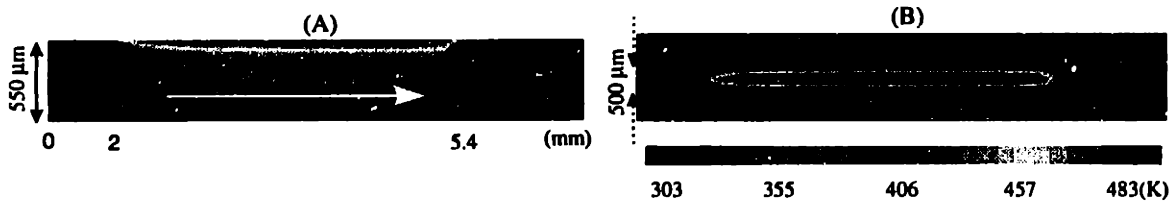


***Figure 4.4*** *Simulation of microreactor temperature profiles at 20 std. $cm^3$/min flow of $O_2$. Temperature profile in A) Axial cross-section of the channel, and B) Top-view of the membrane. The hot-zone is localized to the SiN membrane and adjacent gas, while the edges of the membrane and the bulk Si are at room temperature (Courtesy of I -M. Hsing).*

Simulations further revealed that the hot-zone was localized to the membrane and adjacent gas, while the channel walls were at room temperature (Figure 4.4). The excellent thermal conductivity of the bulk silicon (141 $W/m^2/°C$) and its large thickness

(550 μm) relative to the $SiN_x$ membrane (1 μm), contributes to the bulk silicon's efficient heat sinking capacity, resulting in the localized hot zone. The cold walls could potentially make the microreactors safer to operate by quenching the gas-phase radicals, thus preventing chain branching runaway reactions. Simulations also showed convection effects in the microreactor with increasing gas flowrates (Figure 4.5). The upstream temperature dropped significantly at larger flowrates, while the downstream temperatures remained constant. The simulations are in excellent agreement with experimental results (Figure 4.5B).

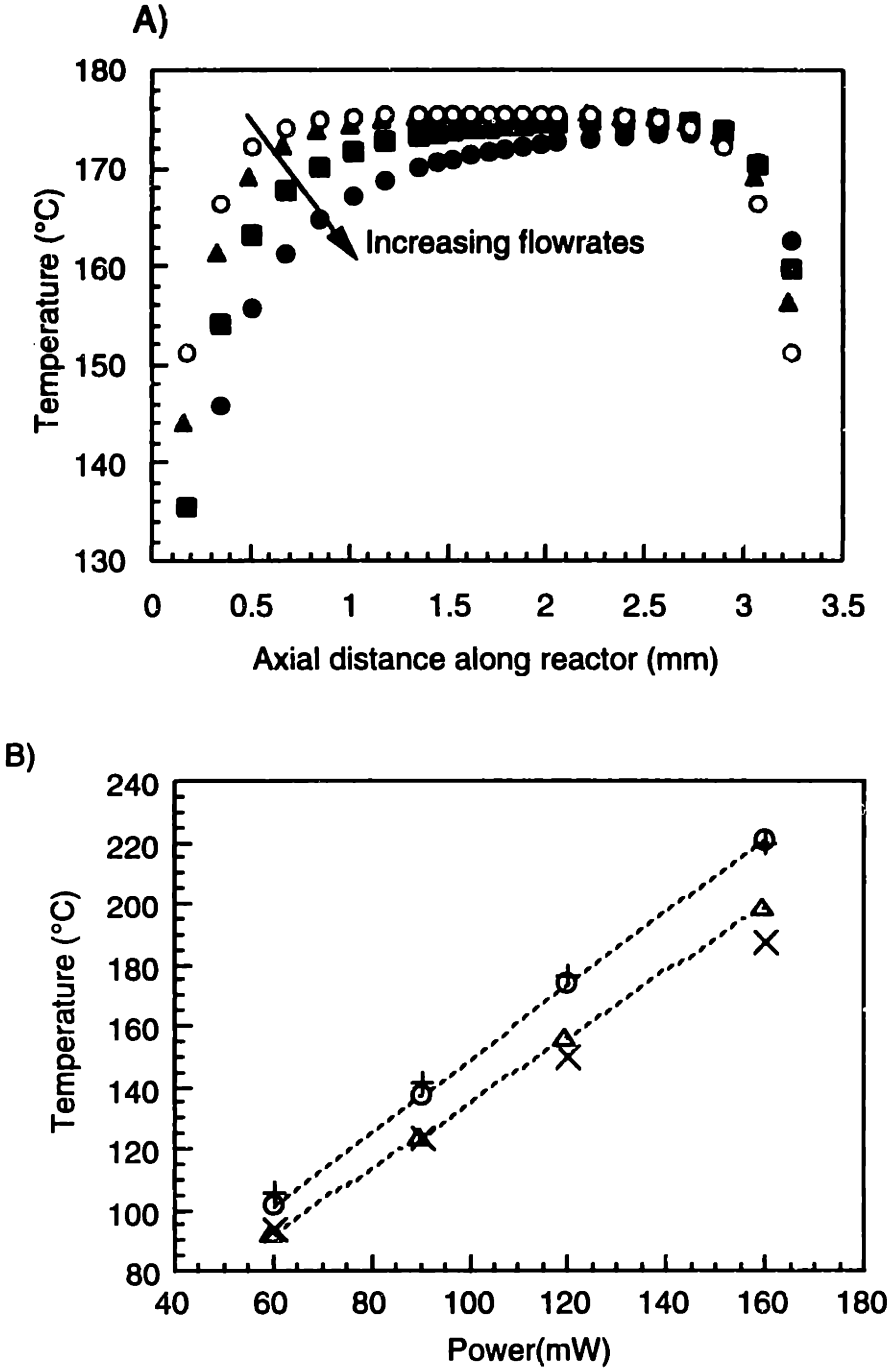


***Figure 4.5*** *A) Simulation of axial temperatures in the microreactor showing heat convection at increasing flowrates of $O_2$ (Courtesy of I-Ming Hsing). ○: 0 std. $cm^3$/min, ▲: 10 std. $cm^3$/min, ■ 25 std. $cm^3$/min and ●: 50 std. $cm^3$/min flow. B) Comparison of simulations (Δ downstream and ○ upstream circles) with experimental data. (X: downstream and ✚ upstream temperatures). The temperature resolution of the experimental data is ± 0.5°C.*

### 4.3 Ammonia oxidation in microreactor

Ammonia oxidation was chosen as the candidate reaction for microreactor studies because it is well understood [3, 4], highly exothermic, without catalyst contamination by carbon, and has several series and parallel reaction pathways allowing for selectivity studies. The desired product of the reaction is NO, while $N_2$ production represents product loss. Ammonia oxidation is used industrially in the production of nitric acid, and constitutes an important step in ammoxidation reactions used to produce nitrogen-bearing compounds for agricultural chemicals and monomers [5]. The major overall reactions in previously proposed mechanisms [3, 6] are:

$$NH_3 + \tfrac{5}{4}O_2 \xrightarrow{Pt} NO + \tfrac{3}{2}H_2O + 226kJ \quad \text{(R1)}$$

$$NH_3 + \tfrac{3}{2}NO \xrightarrow{Pt} \tfrac{5}{4}N_2 + \tfrac{3}{2}H_2O + 454kJ \quad \text{(R2)}$$

$$NO \xrightarrow{Pt} \tfrac{1}{2}N_2 + \tfrac{1}{2}O_2 + 90kJ \quad \text{(R3)}$$

$$NH_3 \xrightarrow{Pt} \tfrac{1}{2}N_2 + \tfrac{3}{2}H_2 - 47kJ \quad \text{(R4)}$$

$$H_2 + \tfrac{1}{2}O_2 \xrightarrow{Pt} H_2O + 242kJ \quad \text{(R5)}$$

#### 4.3.1 Ignition- Extinction Experiments

Reaction experiments were conducted on heater segment 3 (Figures 4.2), which was 3.4 mm long and had two temperature sensors—an upstream temperature sensor 350 μm from the beginning of the heater segment, and a downstream temperature sensor 150 μm

from the end of the heater segment. The detailed experimental procedure including the calibrations, leak-checks, and catalyst activation procedure are described in Section 3.4. In a typical experimental run, the power supplied to the heater was increased at a fixed inlet composition and flowrate of $NH_3$ and $O_2$.

Ignition occurred at ~200 °C in the center of the heater segment, resulting in a temperature rise due to heat of reaction (Figure 4.6). At operating flowrates (<15 sccm), the ignition front quickly traveled upstream and stabilized at the entrance region of the heater, resulting in higher temperature upstream, while the downstream temperature remained at ~200°C. Upon ignition, the $NH_3$ peak dropped in the mass spectrometer output of the exhaust stream, while the NO and $N_2$ peaks increased as they were produced (Figure 4.7). When the heater power was lowered, the ignited area gradually decreased; the downstream sections extinguishing first, and the upstream section eventually extinguishing at temperatures ~300°C.

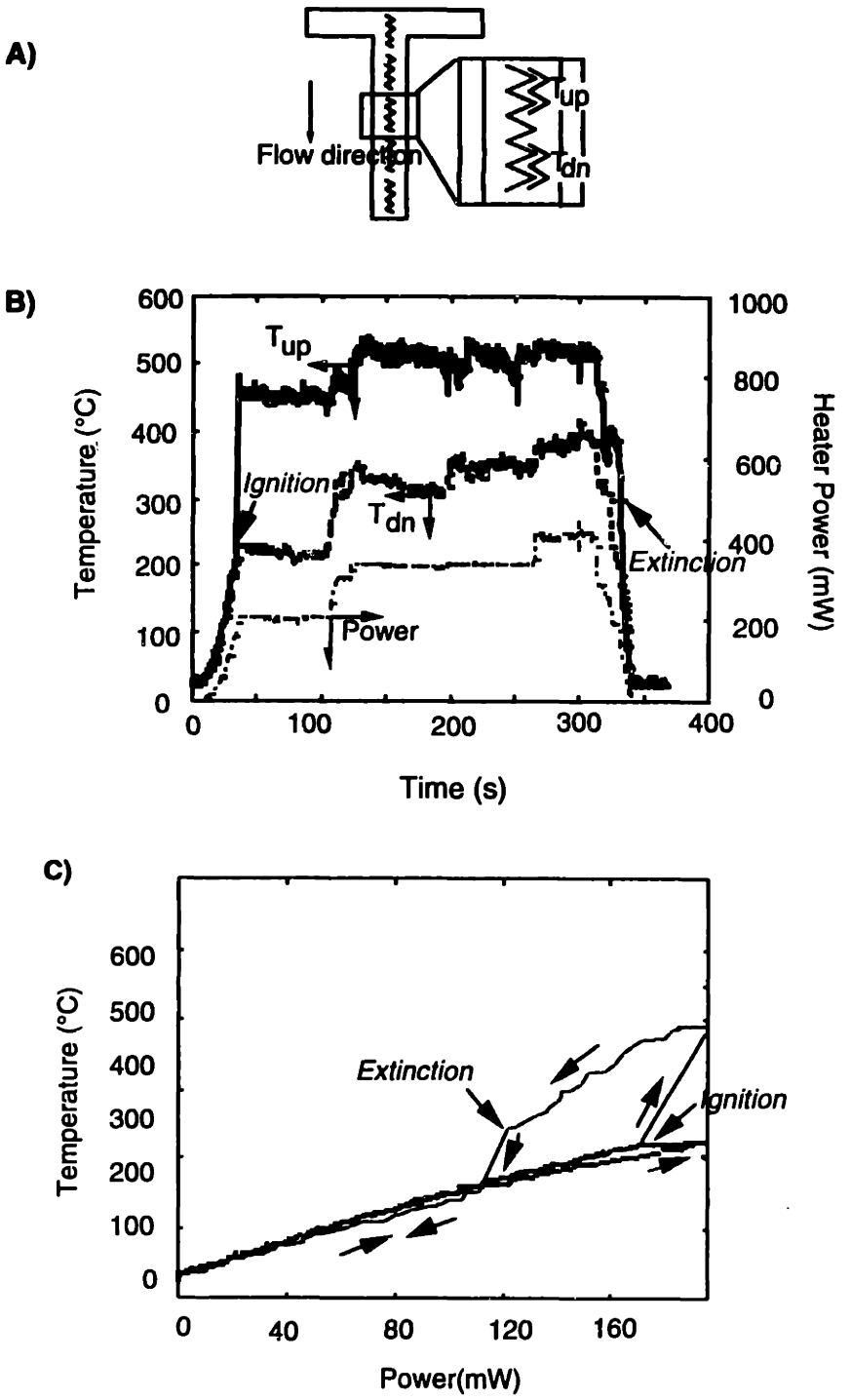


***Figure 4.6*** *A) Schematic of a microreactor showing active heater segment and position of temperature of sensors used in the experiment. B) Typical experimental result showing temperatures and heater powers with time. These results were collected at 15% inlet composition of $NH_3$ in $O_2$, pressure of 1 atm, and total flowrate of 5 std. $cm^3$/min. C) Temperature-power diagram for the same experiment, showing hysteresis behavior on the upstream temperature sensor, while the downstream sections did not ignite.*

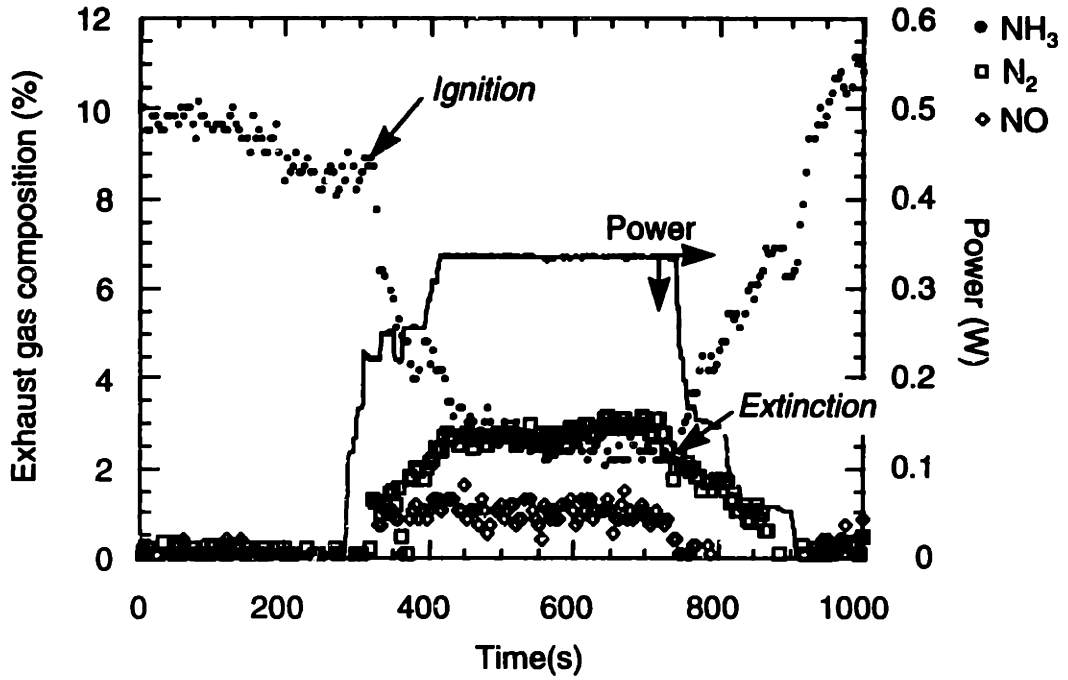


***Figure 4.7*** *Typical exhaust composition of the microreactor as a function of power.*

***Dynamics of Ignition Front Movement***

Simulations of the underlying physical chemical phenomena have confirmed that the upstream movement is a result of axial heat conduction in the membrane, and the presence of fresh reactants upstream [2]. The upstream movement of ignition wave, and the resulting difference between the upstream and downstream temperatures, was found to vary both with flowrates and inlet composition. At low flowrates, most of the reaction occurred at the entrance region of the heater segment, which consumed a large fraction of the reactants. This reactant depletion resulted in decreased downstream reaction and corresponding low heat generation rates, and the temperature downstream remained at the ignition value of 200°C. At larger flowrates, however, a significant reaction takes place downstream. This behavior, combined with increased convection, resulted in higher downstream and lower upstream temperatures at large flowrates (Figure 4.8A).

Figure 4.8B provides further insight into the relative importance of upstream reaction, and convection on the temperature profiles in the microreactor. In an inert gas flow, the temperature is higher downstream than upstream, even at low flowrates (5 sccm), because of convection. In contrast, when a reacting mixture is flowing, both the upstream reaction, as well as the convection of heat and reactants, determine the temperature profile. At low flowrates the temperature upstream is higher, but at large flowrates (>50 sccm), convection effects equalize the temperature profile along the heater segment.

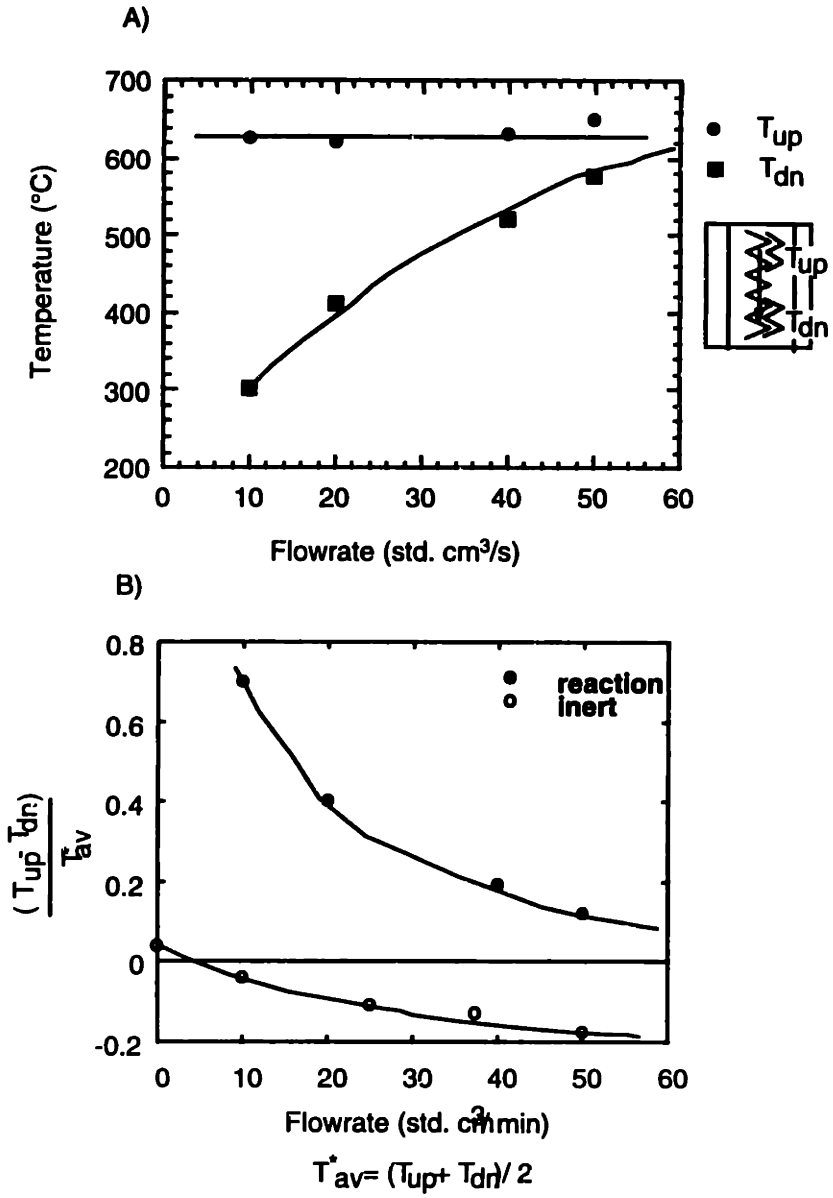


***Figure 4.8*** *A) Upstream and downstream temperatures as a function of flowrates for inlet compositions of 10% $NH_3$ in $O_2$, and power of 245±25 mW. Convection effects equalize the temperatures along the heater segment at higher flowrates. B) Temperature difference between upstream and downstream sections of the heater segment at varying flowrates. In inert flow, heat convection results in higher downstream temperatures, while in reactive flow, the opposing effects of upstream heat movement caused by reaction, and downstream convection of reactant and heat can be seen. The temperature difference is not zero at no-flow because of a small asymmetry in placement of sensors (cf. Figure 4.2). The resolution of the temperature data is ± 0.5°C.*

The temperature rise after ignition, and the corresponding thermal expansion, deformed the microreactor membrane (Figure 4.9), with increased deformations at larger temperatures. The deformations were visible at temperatures higher than 300°C. Although the deformation is undesirable from the standpoint of mechanical integrity of the membrane, it was a convenient research feature, allowing visualization of the progress of reaction (Figure 4.9). Video images of the membrane buckling showed that the ignition front moved upstream within 66 ms after igniting, reaching steady state after 160 ms.

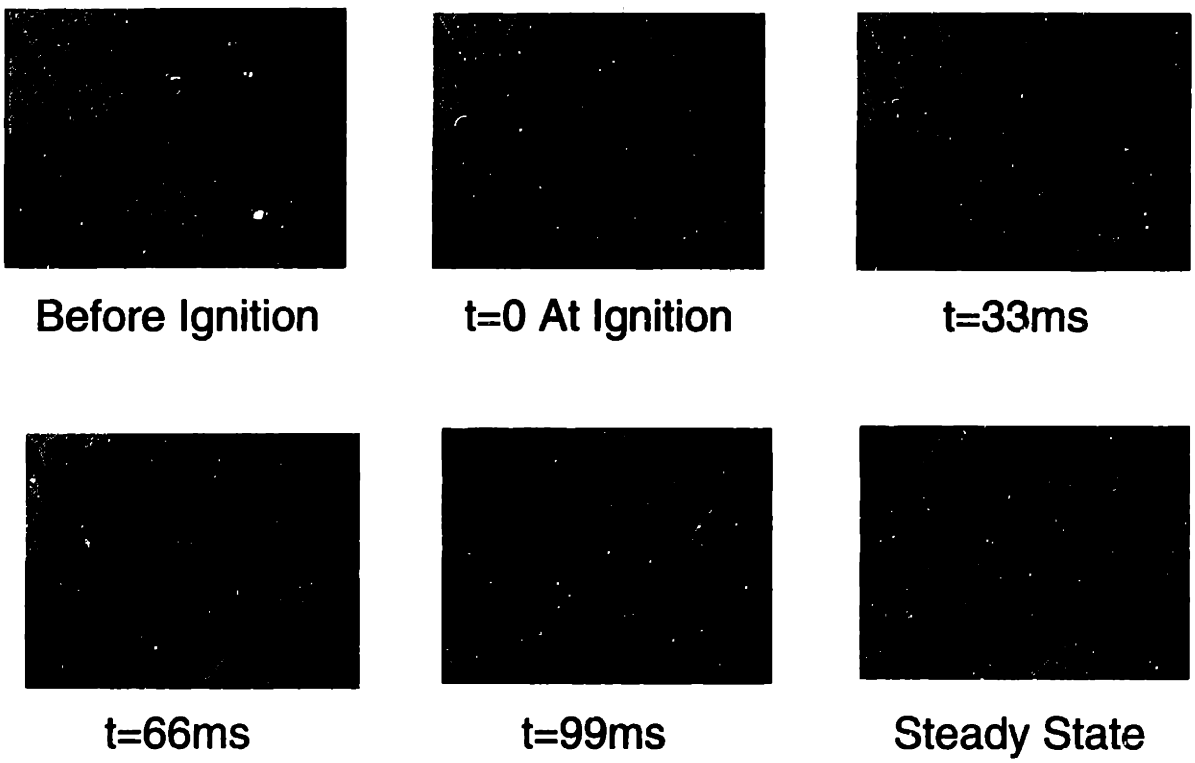


***Figure 4.9*** *Video frames of membrane deformation due to temperature rise and upstream movement of an ignition front in the microreactor. The ignition front eventually stabilizes in the entrance region of the heater.*

***Effect of inlet composition on Ignition-Extinction***

The ignition temperature (~200°C) was found to be independent of the inlet composition. However, the temperature rise after ignition in the upstream temperature sensor increased at inlet compositions that were close to stoichiometry (Figure 4.10), which is consistent with observations in conventional laboratory reactors [7]. At inlet compositions between ~20% and ~70% $NH_3$ in $O_2$, the ignition front was not localized to the active heater segment (#3), and moved upstream to the mixing point. Thus the reaction was self-sustaining and could not be extinguished even by shutting off the power to the on-chip heaters.

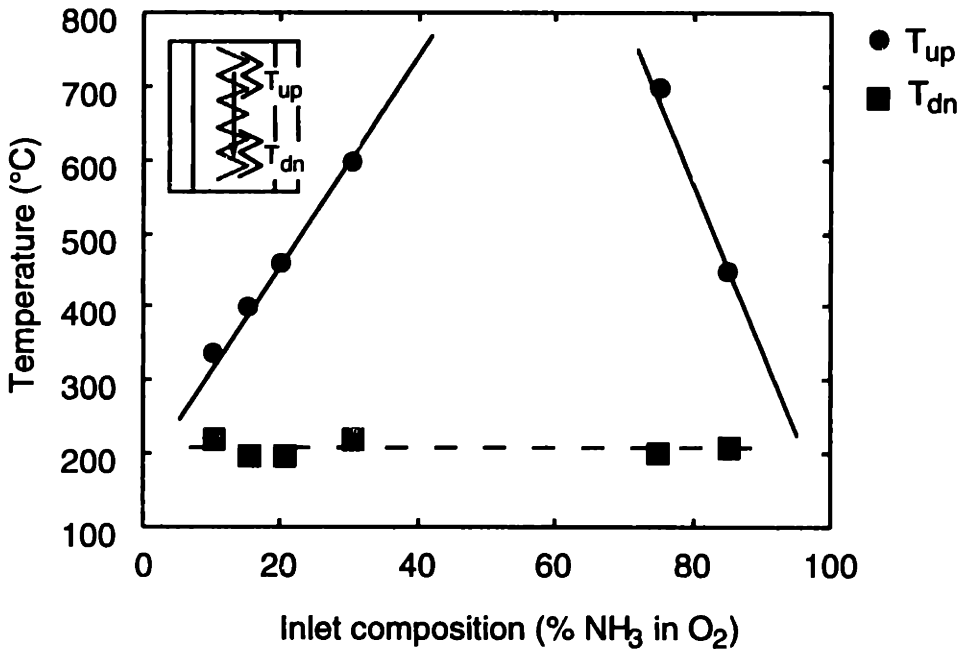


***Figure 4.10*** *Upstream and downstream temperatures with changing inlet composition of $NH_3$ in $O_2$. All data were collected at a total flowrate of 5 sccm, pressure of 1 atm, and heater power of 188±12 mW.*

Depending upon the heat transfer characteristics of the heater and the chemical activity of the catalyst, the range of inlet compositions between which the reaction was self-sustaining varied from 17% -75% to 25%-65%. In some cases, the catalyst upstream

of heater segment 3 was not properly activated, and the ignition front did not move upstream all the way to the mixing point. Experiments closer to stoichiometric mixtures were not conducted, since the microreactor membrane degraded and ruptured at temperatures higher than ~650°C.

### *Effect of External Heating of Microreactor on Ignition-Extinction*

In some of the reaction tests, the microreactor was externally heated to ~150°C to prevent water produced in the reaction from condensing on the cold microreactor walls. Operating the microreactor at 150°C rather than at room temperature changed the heat transfer behavior of the microreactor. Comparison of temperature-power plots of the on-chip heaters operating in an inert ($O_2$) ambient for the externally heated and unheated microreactors show that the externally heated microreactors have better heat transfer (Figure 4.11). This was a counter intuitive and surprising result since external heating would reduce the temperature gradient between the heater and the microreactor walls resulting in decreased heat transfer (as predicted by 1-D model in Section 2.2.2). The increased heat transfer in externally heated microreactors was due to additional heat transfer mechanism of natural convection that was initiated by the large heated surface area of the Al block. Simulations that included natural convection effects show good agreement with the experimental results (Figure 4.11) [2].

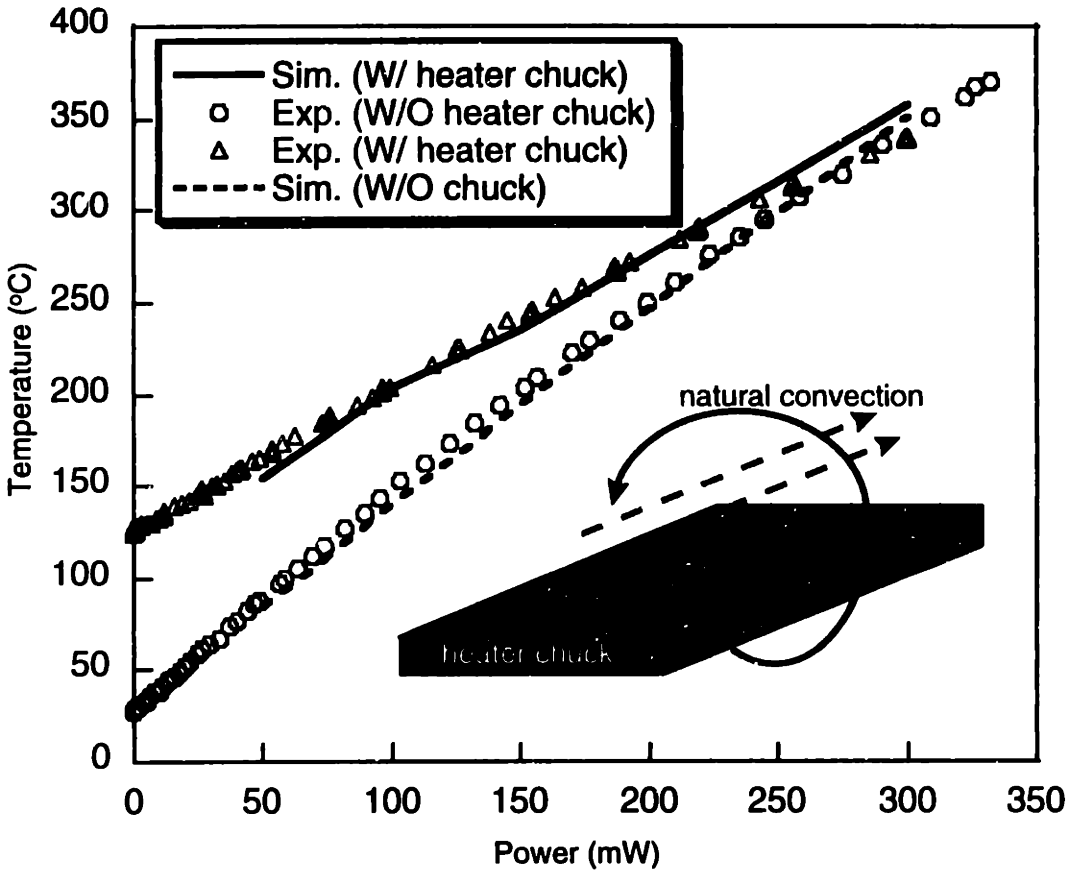


***Figure 4.11*** *A) Temperature-power plots of unheated and externally heated microreactor in $O_2$ ambient. The same microreactor was used for both experiments. The resolution of the temperature data is ± 0.5°C.*

Externally heating the microreactor also changed the ignition-extinction behavior. The range of compositions over which the reaction could be extinguished by shutting off the power to the on-chip heaters decreased, when the microreactor was externally heated. In the unheated microreactor operating at room temperature, 10% $NH_3$ in $O_2$ mixtures were routinely ignited, and the ignition front was localized to the active heater segment. However, upon ignition of 10% $NH_3$ in $O_2$ in the externally heated microreactor

(T=110°C), the reaction was self-sustaining and could not be extinguished by shutting off the power (Figure 4.12).

A constant current power supply was used for these experiments. After ignition, the current supply was increased and maintained at a maximum value that does not excessive membrane deformation. The reaction shut-off periodically due to a malfunctioning $NH_3$ mass-flow-controller, leading to the temperature drops and temperature excursions (Figure 4.12). As the temperature dropped, the electrical resistance of the heater dropped, leading to a drop in power since a constant current source was used (Figure 4.12).

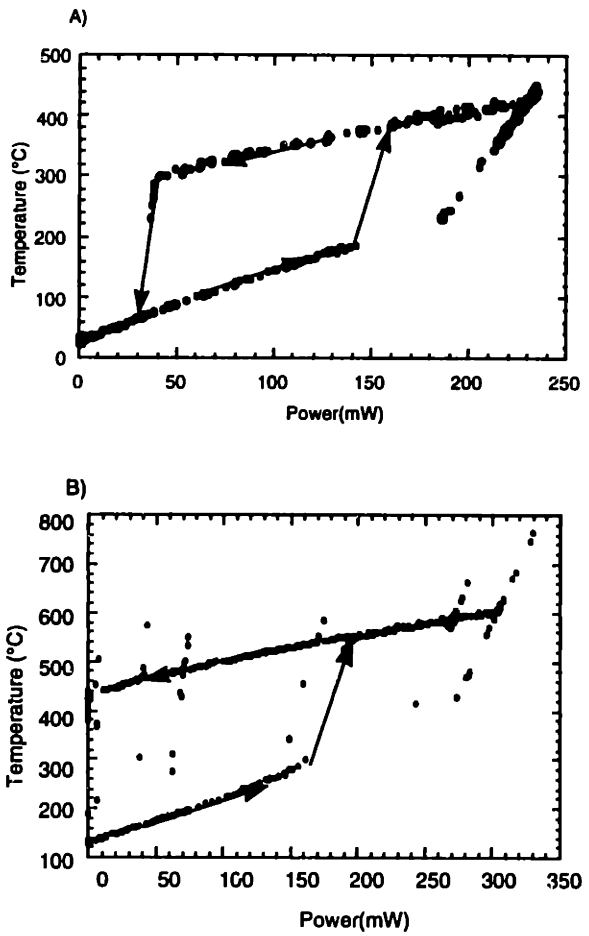


***Figure 4.12** Ignition-extinction behavior at 10% $NH_3$ in $O_2$ mixture at 20sccm flowrate for A) Unheated microreactor and B) Externally heated microreactor. The reaction cannot be extinguished for externally heated microreactor.*

In most cases, the ignition front was not restricted to heater #3 and moved upstream to the mixing point at the reaction channel entrance (Figure 2.1),. But, the ignition was localized to heater 3 for this test because the upstream sections of the catalyst were not active. Externally heated microreactors had a better heat transfer compared with unheated microreactors (lower temperature-power slope for heated microreactor; Figure 4.11). In spite of the better heat transfer, the range of compositions over which the reaction could be extinguished was smaller in externally heated microreactors. This suggested that the upstream movement and the extinction behavior were functions of upstream temperature and not the heat transfer characteristics. The upstream sections in the externally heated microreactor were at 150°C, while the upstream sections of the unheated microreactor were at 25°C. Further work is necessary to understand the complex and non-linear ignition-extinction phenomena in microreactors.

### 4.3.2 Conversion- Selectivity Experiments

Conversion and selectivity were explored as a function of heater powers, flowrates (contact-times), and inlet compositions. The primary products of the reaction were NO and $N_2$ (Figure 4.7). $N_2O$ was formed in small quantities (<15%) at temperatures below 350°C and was absent at temperatures higher than 400°C due to $N_2O$ decomposition, consistent with conventional reactor studies [3].The selectivity ratio of NO to $N_2$ increased dramatically with heater power (Figure 4.13). The error-bar was determined from the mass-spectrometer drift calibrations (Section 3.3). The error calculation procedure is detailed in Appendix H. The strong selectivity increase with temperature is also consistent with conventional laboratory reactor data [3], and is likely caused by a low

NO residence time on the catalyst surface preventing NO dissociation (reaction 3) [4] and reaction with $NH_3$ (reaction 2) [3].

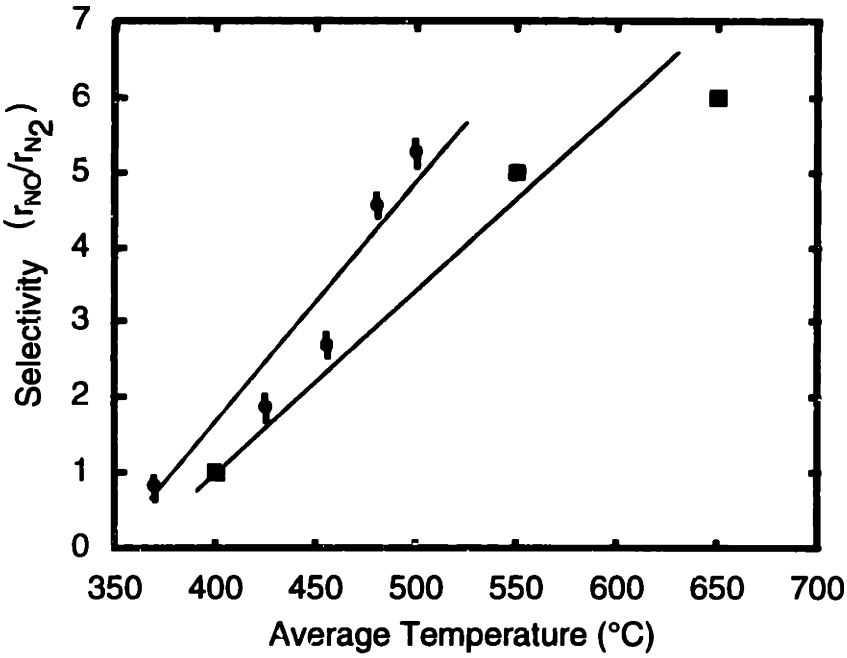


***Figure 4.13*** Selectivity variation with temperature for the microreactor and comparison with conventional laboratory reactors (●: microreactor data 10% $NH_3$ in $O_2$; ■: conventional laboratory reactor, 5.3% $NH_3$ in air, 20% $NH_3$ in $O_2$).

After ignition, as the heater power was further increased, the conversion increased slightly with the spreading of the reaction to downstream sections of the heater. However, increases in conversion with heater power were much less than could be expected from a simple consideration of reaction rate increase with temperature, indicating that the reaction was mass-transfer limited after ignition. The maximum conversion obtainable increased with contact-time, with complete conversion observed at contact-time > 9 ms (Figure 4.14). The conversion error-bar calculation is detailed in Appendix H. This conversion-contact time behavior indicates that the reaction becomes residence-time limited with significant fractions of the reactants bypassing the catalyst at

higher flowrates. The selectivity of NO to $N_2$ decreases with contact-time since larger contact times allow NO to readsorb and further dissociate (reaction 3) [4] and/or react with $NH_3$ (reaction 2) [3] to produce $N_2$. Thus a classic conversion-selectivity trade-off is observed with contact-time. The conversion was found to be independent of inlet composition. However, the selectivity dropped to 0% when operating in $NH_3$-rich conditions because $NH_3$ inhibits NO desorption [3].

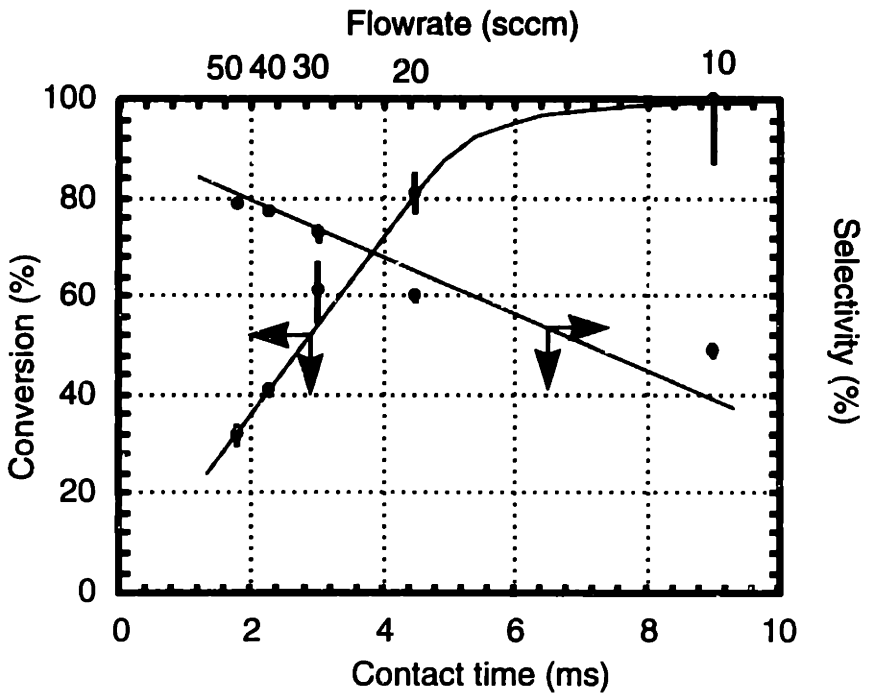


***Figure 4.14*** *Maximum conversion and selectivity in a single heater segment of microreactor as a function of contact time (flowrate). All data were collected at an inlet $NH_3$ to $O_2$ ratio of 10% and average catalyst temperature of 425°±25°C.*

The conversion perfomance of the microreactor is poorer than the industrial catalytic gauze performance due to the large diffusion lengths. Calculations using literature data on mass transfer limitations [8] indicate that 100% conversion of $NH_3$ can be obtained within 3ms on conventional wire-gauzes, while the microreactor requires 9ms for

complete conversion. The calculated productivity of microreactors using the conversion and selectivity data (Figure 4.14) is 0.6 moles NO produced/ s/ $m^2$ of Pt catalyst. Based on this productivity and catalyst area of the prototype microreactor, ~10kgs/day of NO (3.65 tons/year) can be produced by operating 1000 prototype microreactors in parallel.

The ammonia oxidation test results suggest design changes for improving conversion and selectivity in microreactors. Building a microreactor that has catalyst on both the top and bottom face of the channel would reduce the diffusion time, and large conversions can then be obtained at low contact-times, while maintaining high selectivities. In the current design, at low flowrates, most of the reaction occurs in a small upstream section of the heater segment (~1 mm) while a large section downstream (2.4 mm) is unutilized. Therefore, shorter heater segments would allow more efficient use of microreactor area.

### 4.4 Microreactor materials stability issues

Microreactor materials degradation was observed when operating at elevated temperatures. Large mechanical stresses in the SiN membrane caused by thermal expansion, deform and eventually rupture the membrane at temperatures >700°C. Membrane stability was improved by increasing the thickness, and alternative materials systems and designs are being explored to further improve the stability. Visual observation of the reactors after operation also indicated that thin film Pt heaters and temperature sensors began to degrade at temperatures >700°C (Figure 4.15). However, *in-situ* experiments revealed that the electrical characteristics of the heaters and temperature sensors were consistent and repeatable up to 800°C.

At temperatures <700°C, the microreactor lifetime was limited by the Pt catalyst etching by the reactant mixture of $NH_3$ and $O_2$ (Figure 4.15). The microreactor has been operated for ~ 1 hour at 600°C before the 0.1μm thick Pt catalyst was etched. The etching behavior is also observed in conventional reactors [5]. While there is agreement in the literature that Pt is lost to the gas stream, there is disagreement regarding the specific mechanism by which catalyst is lost. Flytzani-Stephanopoulos and Schmidt proposed formation of volatile $PtO_2$, at temperatures ~800°C, as the etching mechanism [9, 10]. It has also been proposed that the Pt reacts with gas-phase radicals, *e.g.*, $HO_2$, to form volatile metastable complexes that are lost to the gas-phase [11, 12]. Lyubovsky and Barelko proposed that the pure Pt from the grain boundaries sublimates due to the coupled effects of enhanced catalytic activity, causing increased temperature and the weak binding of Pt atoms at grain boundaries [13]. The low operating temperatures (400°C-600°C) in the microreactor suggests that $PtO_2$ formation, as an etching mechanism, is unlikely. Further, etching is not observed in the Pt heater and sensors which are exposed to air and are at the same temperature at the Pt catalyst, and have the same thickness (0.1μm). This suggests that both $NH_3$ and $O_2$ have a role to play in the catalyst etching in the microreactor.

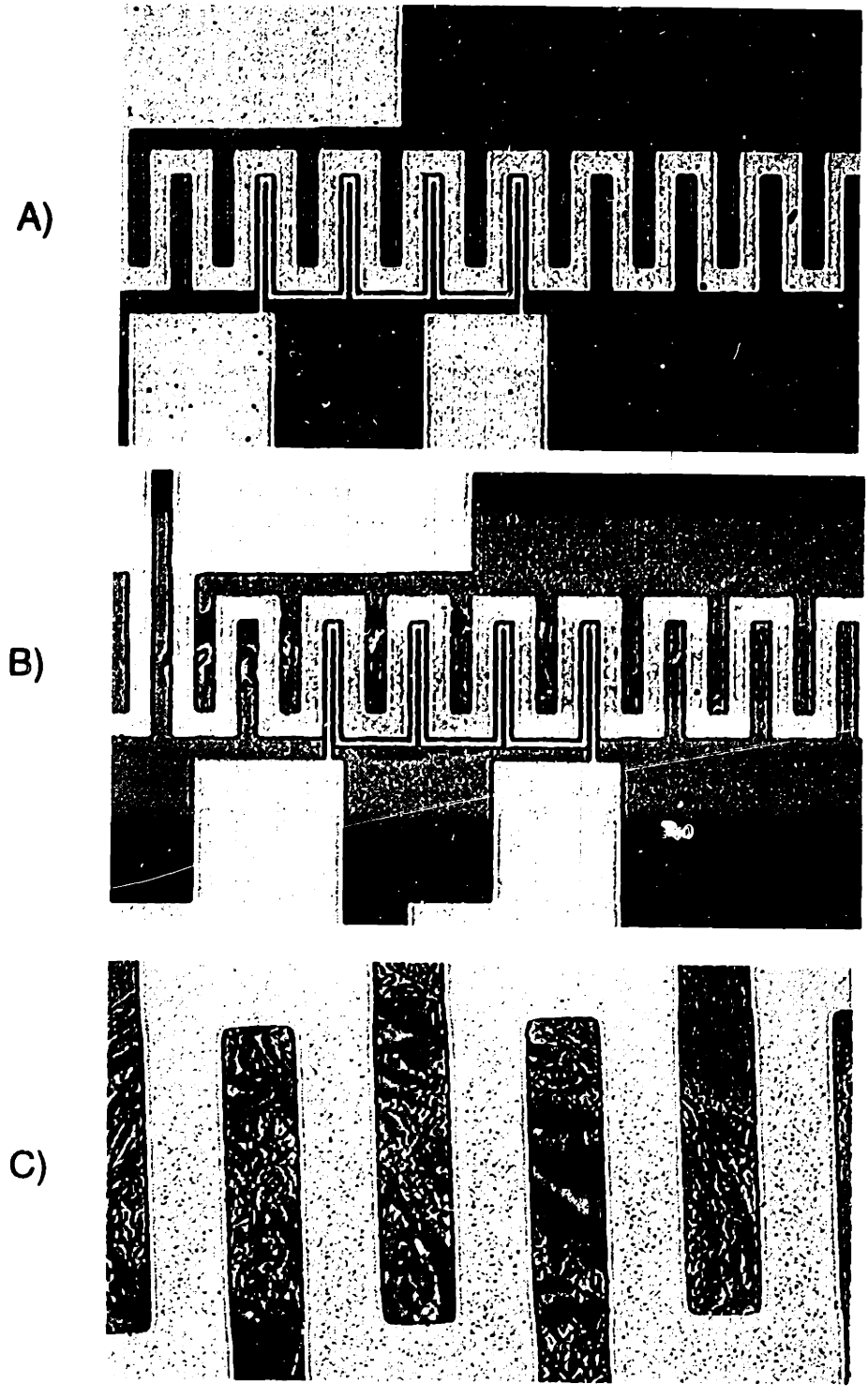


***Figure 4.15*** *Photographs of A) fresh microreactor, B) degraded microreactor, and C) close-up of degraded microreactor. The Pt catalyst has been etched and the heater material has visibly degraded, with pin-hole formation (visible in C) after operation at 600°C for ~0.5 hrs.*

## 4.5 Hydrocarbon Oxidation Experiments

In addition to $NH_3$ oxidation, several model oxidation systems, specifically CO, $H_2$, and $C_2H_6$ on Pt, and $C_2H_4$ on Ag, were explored in the SiN microreactor. The first experiment on the microreactor was CO oxidation on Pt, because this reaction is well studied and relatively well understood [14]. The reaction ignited at ~400°C and $CO_2$ was produced. The catalyst deactivated during the course of this reaction, leading eventually to extinction of the reaction. Ex-situ Auger analysis showed that the catalyst deactivation was due to Ni and C deposits on the catalyst surface. The source of Ni were the solenoid valves of the mass flow controllers (Unit Instruments UFC 1100) which reacted with CO to form volatile $Ni(CO)_5$ that condensed and plated the catalyst surface.

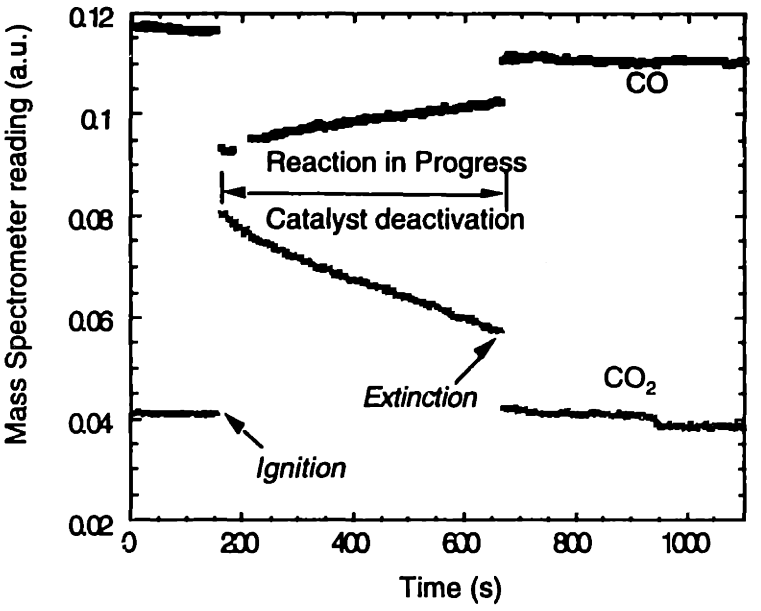


***Figure 4.16*** *Pt catalyzed CO oxidation in the microreactor. The reaction was carried out at an inlet CO to $O_2$ ratio of 0.13 and flowrate of 10sccm. The catalyst deactivation was due to C and Ni deposits on the catalyst surface.*

There has been a lot of interest reacently in the use of alkanes as cheaper replacements for aromatics and olefins as petrochemical feedstock [15]. Schmidt and co-workers have

demonstrated oxidation of several alkanes on Pt gauze catalysts to olefins and oxygenates [16, 17]. Since gauze catalysts are susceptible to flash back and explosions, we explored the use of microreactors for alkane conversion to chemical intermediates. $C_2H_6$ oxidation on Pt was chosen as a model alkane oxidation to study in the microreactor. Ignition occurred at ~200 °C which is lower than the ignition temperatures of conventional laboratory reactors [18]. While there were no explosions even during operation in the explosive regime, $C_2H_6$ was completely oxidized in the microreactor to $CO_2$ and $H_2O$. The complete oxidation was possibly due to the large residence time in the microreactor (~10ms) compared with gauze reactors (<1ms) [16, 19]. The large residence times could allow the partial oxidation intermediates to readsorb on the Pt catalyst and undergo further oxidation to $CO_2$ and $H_2O$. The microreactor design should be changed to allow shorter residence times to prevent complete oxidation.

Attempts were made to oxidize $C_2H_4$ to $C_2H_4O$ on e-beam deposited Ag catalyst film. We did not observe any reaction upto temperatures of ~350 °C. $C_2H_4$ oxidation reaction is known to be very sensitive to catalyst composition and structure [20]. It is possible that e-beam deposited pure Ag is not active for $C_2H_4$ partial oxidation.

Pt catalyzed $H_2$ oxidation was carried out as a demonstration of the safety potential of the microreactor because it is highly exothermic and is an explosion danger. $H_2$ was safely ignited in the microreactor even in the explosive regime (~25% $H_2$ in $O_2$). The reaction ignited at ~180°C, and the main product was $H_2O$.

### 4.6 Summary

Experiments and simulations indicate that one of the unique features of the microreactor is the localized reaction hot-zone, while the channel walls and the bulk of the chip are at room temperature. This could potentially make microreactors safer to operate than conventional reactors, by suppressing flame formation by quenching gas-phase radicals on the cold reactor walls. The microreactor has been tested using Pt catalyzed $NH_3$ oxidation as a model reaction. Test results show that conversion and selectivity behavior of conventional reactors can be reproduced, demonstrating feasibility of conducting chemical reactions in microfabricated systems. While further research is required to address scale-up issues, the current design and operation of a single microreactor could be used as a laboratory platform for kinetic studies. The advantages provided by microreactors for kinetic studies include safety, low reactant usage, less waste, and well-defined geometries that allow relatively simple simulations for better understanding of reaction kinetics. We have ignited highly flammable mixtures without diluents (*e.g.*, 20% $H_2$ and $O_2$, $NH_3$ and $O_2$ at all compositions, $C_2H_6$ and $O_2$ at all compositions) in the microreactor, without an explosion. In some cases, the high temperature induced differential thermal expansion ruptured the membrane, releasing the reactants into air, but the small volumes were quickly diluted in the exhaust system.

## References

[1] T. R. Ohnstein, R. G. Johnson, R. E. Higashi, D. W. Burns, J. O. Holmen, E. A. Satren, G. M. Johnson, R. E. Bicking, and S. D. Johnson, "Environmentally rugged, wide dynamic range microstructure airflow sensor," presented at Solid-State Sensor and Actuator Workshop, Hilton Head, SC, 1990.

[2] I.-M. Hsing, in *Chemical Engineering*. Cambridge, MA.: Massachusettes Institute of Technology, 1997.

[3] T. Pignet and L. D. Schmidt, "Selectivity of ammonia oxidation on Pt," *Chemical Engineering Science*, vol. 29, pp. 1123-1131, 1974.

[4] J. M. Bradley, A. Hopkinson, and D. A. King, "Control of biphasic surface reaction by oxygen coverage: The catalytic oxidation of ammonia of Pt(100).," *Journal of Physical Chemistry*, vol. 99, pp. 17032-17042, 1995.

[5] C. N. Satterfield, *Heterogeneous Catalysis in Industrial Practice*, 2nd ed. New York: McGraw-Hill Inc., 1991.

[6] T. Pignet and L. D. Schmidt, "Kinetics of ammonia oxidation on Pt, Rh, and Pd," *Journal of Catalysis*, vol. 40, pp. 212-225, 1975.

[7] W. R. Williams, M. T. Stenzel, X. Song, L. D. Schmidt, "Bifurcation behavior in homogeneous- heterogenous combustion: I. Experimental results over Platinum," *Combustion and Flame*, vol. 84, pp. 277, 1991.

[8] C. N. Satterfield and D. H. Cortez, "Mass transfer characteristics of woven-wire screen catalysts," *Industrial and Engineering Chemistry Fundamentals*, vol. 9, pp. 613-620, 1970.

[9] M. Flytzani-Stephanopoulos, S. Wong, and L. D. Schmidt, "Surface morphology of platinum catalysts," *Journal of Catalysis*, vol. 49, pp. 51-82, 1977.

[10] M. Flytzani-Stephanopoulos and L. D. Schmidt, "Evaporation rates and surface profiles on heterogeneous surfaces with mass transfer and surface reaction," *Chemical Engineering Science*, vol. 34, pp. 365-372, 1979.

[11] V. W. Dean, M. Frenklach, and J. Phillips, "Catalytic etching of Platinum foils and thin films in Hydrogen-Oxygen mixtures," *Journal of Physical Chemistry*, vol. 92, pp. 5731-5738, 1988.

[12] J. M. Hess and J. Phillips, "Catalytic etching of Pt/Rh gauzes," *Journal of Catalysis*, vol. 136, pp. 149-160, 1992.

[13] M. R. Lyubovsky and V. V. Barelko, "Formation of metal wool structures and dynamics of catalytic etching of platinum surfaces during ammonia oxidation," *Journal of Catalysis*, vol. 149, pp. 23-35, 1994.

[14] T. Engel and G. Ertl, "Elementary steps in the catalytic oxidation of CO on Pt," in *Advances in catalysis*, vol. 28, D. D. Eley, H. Pines, and P. B. Weisz, Eds. New York: Academic Press, 1979.

[15] G. Centi and F. Trifiro, "New Developments in Selective Oxidation," . New York: Elsevier, 1990.

[16] D. A. Goetsch and L. D. Schmidt, "Microsecond catalytic partial oxidation of alkanes," *Science*, vol. 271, pp. 1560-1562, 1996.

[17] M. Huff and L. D. Schmidt, "Production of olefins by oxidative dehydrogenation of propane and butane over monoliths at short contact times," *Journal of Catalysis*, vol. 149, pp. 127-141, 1994.

[18] G. Veser and L. D. Schmidt, "Ignition and extinction in the catalytic oxidation of hydrocarbons over Pt," *AIChE Journal*, vol. 42, pp. 1077-1087, 1996.

[19] D. A. Goetsch, P. M. Witt, and L. D. Schmidt, "Partial oxidation of butane at microsecond contact times," in *Heterogeneous Hydrocarbon Oxidation*, vol. 638,

*ACS Symposium series*, S. T. O. Barbara K. Warren, Ed.: American Chemical Society, 1996.

[20] R. A. v. Santen and H. P. C. E. Kuipers, "The mechanism of ethylene epoxidation," *Advances in Catalysis*, vol. 35, pp. 265, 1987.

# Chapter 5 Novel Microreactor Designs for Improved Heat and Mass Transfer

Test results from the prototype SiN microreactor (Chapter 4) suggest design improvements for enhanced performance of the microreactor- The temperature rise after ignition (Figures 4.6 and 4.9) suggests improved heat transfer for greater control over reactor temperature. The diffusion-limited operation (Figure 4.12, Section 4.3.2) points towards shallower channel for reducing diffusion resistance. New microreactor designs were implemented and tested for both cases of, improved heat transfer and improved mass transfer.

## 5.1 Si membrane microreactors (Si microreactors) for enhanced heat transfer

Heat transfer models of the SiN microreactor showed that heat conduction via the membrane was the dominant mode of heat transfer out of the catalyst (Section 2.3.1). By increasing the thermal conductivity of the membrane material and by increasing its thickness, the heat transfer could be further increased. Both of these concepts were implemented in new Si microreactors. These systems had a 3μm thick Si membrane (thermal conductivity = 140W/m/°K) (Figure 5.1) as compared to 1μm thick SiN membrane (thermal conductivity ~14W/m/°K) in the previous reactor. Thus, this design allowed for enhanced heat transfer of Si microreactors. Apart from the membrane, the Si microreactor dimension and design were the same as SiN microreactors (Section 2.1).

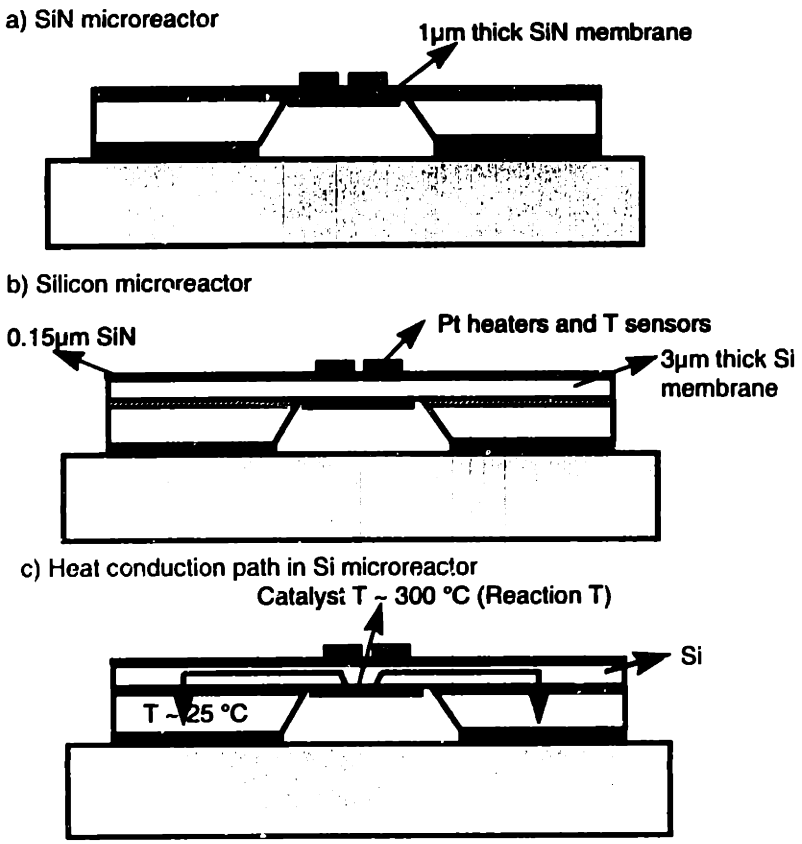


***Figure 5.1*** *Schematic diagrams of- a) SiN microreactor, b) Si microreactor, and c) Heat conduction path from the catalyst to the cold chip via Si membrane in Si microreactor. The enhanced heat transfer of Si microreactor is due to the higher thermal conductivity membrane materiai (Si, $k_{Si}$= 140 W/m/K; $k_{SiN}$ = 14 W/m/K), and larger thickness ($t_{Si}$= 3μm, $t_{SiN}$= 1μm).*

### 5.1.1 Si microreactor fabrication process

The fabrication process for the Si microreactors was similar (Figure 5.2) to that for the SiN microreactor and used the same mask-set (Appendix B). The starting material for the Si

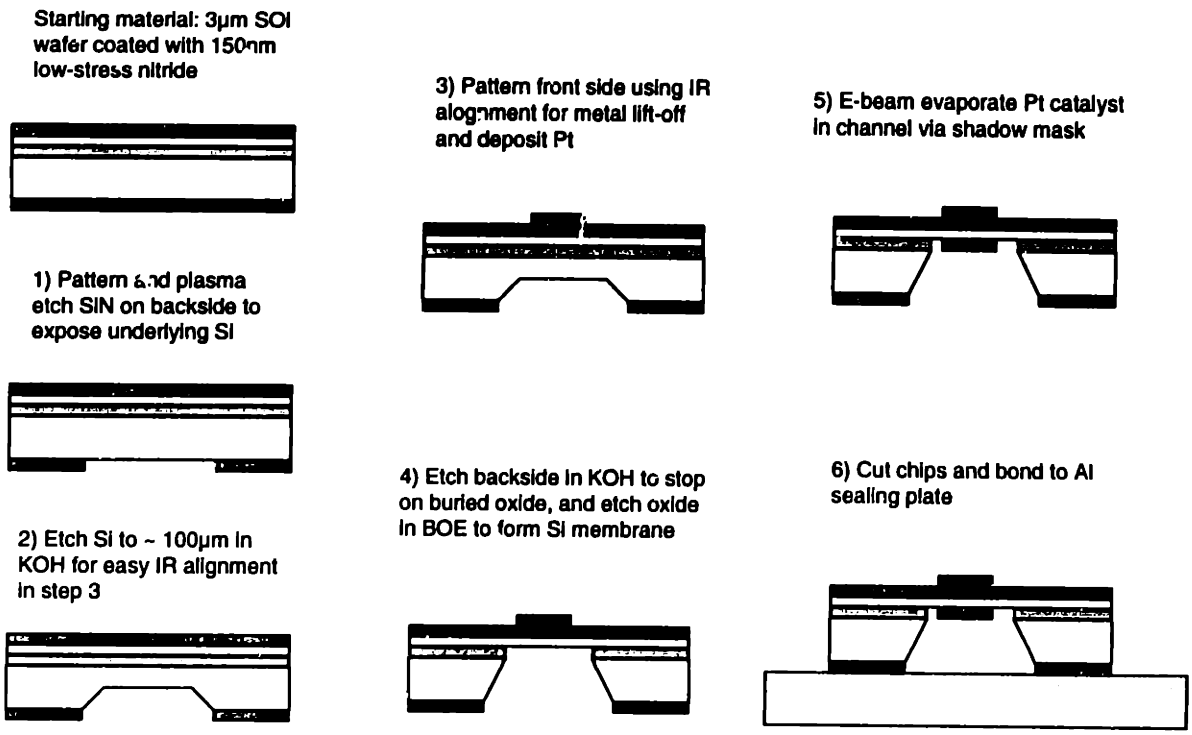


***Figure 5.2** Fabrication process flow for the Si microreactor.*

microreactor fabrication was a Silicon-on-insulator (SOI) wafer (with 3μm thick Si device layer) coated with 150nm thick low-stress SiN. The SiN on the backside of the wafer was patterned and plasma etched (in $SF_6$) to expose the underlying Si in the T-shaped channel regions. The exposed T-shaped Si regions was then etched in KOH to a depth of ~100μm to clearly see, using IR, the T-channels and the alignment marks on the rough wafer backside for frontside photoresist patterning in the following step (Figure 5.2). Using IR alignment, lift-off photo-resist was patterned on the front-side of the wafer for Pt heaters and sensors, followed by a e-beam Pt deposition. The wafer was subsequently etched in KOH using a custom built etch-assembly to protect the metal on the frontside during the etch. The end of the Si etching was determined visually when the bubbling, due to $H_2$ release during Si etching, stopped. The resulting oxide coated Si membrane deformed, and in some cases even ruptured, due to the compressive stress of the oxide. The wafer was then dipped in buffered oxide etch (BOE) for ~10min to etch

the oxide to relieve the membrane stress, and the resulting Si membrane was stress-free and undeformed. Pt catalyst was then e-beam evaporated selectively into the reaction channel via a shadow mask. The shadow mask alignment was achieved using an IR lamp, since the Si membrane does not allow visualization using an optical microscope. In some cases, a blanket catalyst deposition was carried out without a shadow mask. The wafer was then cut into individual chips and packaged with a sealing plate using vacuum grease.

### 5.1.2 Si microreactor Testing

The test setup has been described previously (Chapter 3). The temperature-power curves (Figure 5.3) in an inert ambient ($O_2$) showed that the power required for same temperature rise was much higher for Si microreactor when compared with SiN microreactors, confirming the enhanced heat transfer in Si microreactors.

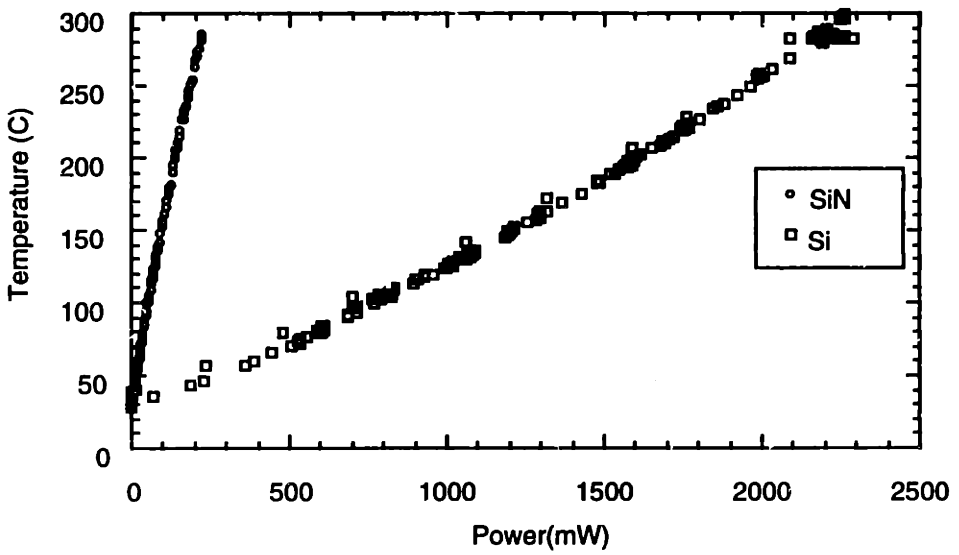


***Figure 5.3** Temperature-Power plots for heating in inert ambient ($O_2$) for SiN and Si microreactors. Higher power is required to heat Si microreactor than SiN microreactor, to achieve the same temperature rise.*

Pt catalyzed ammonia oxidation was again used as a model system to investigate and compare the behavior of Si microreactors, SiN microreactors, and conventional laboratory reactors. At a given inlet composition of $NH_3$ in $O_2$, as the temperature to the Si microreactor was increased to >200°C , the reaction products ($N_2$, NO and $N_2O$) was seen on the mass spectrometer indicating that ignition had occurred, but there was no temperature rise after ignition (Figure 5.4). In contrast, conventional laboratory reactors [1], and the SiN microreactor (Section 4.3.1) showed a large temperature rise after ignition. The difference in behavior was due to the better heat transfer of Si microreactors, with the heat of reaction being conducted away to prevent the temperature rise. Thus, while conventional reactors cannot be operated between ignition and extinction temperatures [1], Si microreactors showed a continous temperature-curve and therefore could be operated at intermediate temperatures.

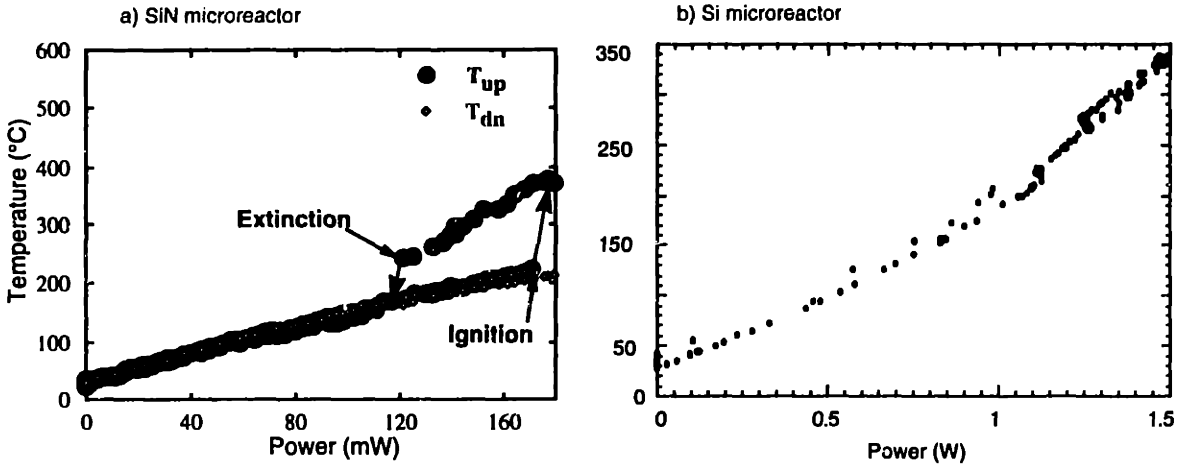


***Figure 5.4** Temperature-Power curves for $NH_3$ oxidation (Inlet conditions: 10% $NH_3$ in $O_2$, flowrate = 10sccm). While SiN microreactor shows temperature rise after ignition, the temperature rise is completely suppressed in the Si microreactor.*

Operating in these intermediate temperatures changed the product distribution of Pt catalyzed $NH_3$ oxidation in Si microreactors compared with conventional laboratory reactors. While NO and $N_2$ are the primary products in conventional laboratory reactors

[2] and in SiN microreactor (Section 4.3.2), significant amounts of $N_2O$ (~15%) was produced in addition to NO and $N_2$ in the Si microreactor, at inlet conditions of 10% $NH_3$ in $O_2$. $N_2O$ is only observed at low temperatures (<400°C) of operation of Pt catalyzed $NH_3$ oxidation [2]. The overall reactions observed in the Si microreactor are:

$$NH_3 + \tfrac{5}{4}O_2 \xrightarrow{Pt} NO + \tfrac{3}{2}H_2O + 226kJ \quad \text{(R1)}$$

$$NH_3 + \tfrac{3}{2}NO \xrightarrow{Pt} \tfrac{5}{4}N_2 + \tfrac{3}{2}H_2O + 454kJ \quad \text{(R2)}$$

$$NH_3 + 2O_2 \xrightarrow{Pt} \tfrac{1}{2}N_2O + \tfrac{3}{2}H_2O + 454kJ \quad \text{(R3)}$$

Although higher operating temperatures and the resulting higher NO selectivity is desirable for $NH_3$ oxidation, operating at lower temperatures accessible to Si microreactors is important in several partial oxidation reactions, e.g. $C_2H_4$ to $C_2H_4O$, where intermediate operating temperatures increase selectivity to the desired partial oxidation product while higher temperatures result in complete oxidation to the thermodynamically stable products, $CO_2$ and $H_2O$.

The higher exothermicity of the complete combustion reactions can also cause runaways and explosions in conventional reactors. By designing the heat transfer of the Si microreactors for the worst-case scenario of complete combustion, the microreactors can potentially be made inherently safe from thermal runaways. A disadvantage, however, of designing and operating a Si microreactor for preventing thermal runaways would be the large external power requirement. While conventional reactors are run autothermally, the excellent heat transfer of the Si microreactors would require external power to maintain the desired reaction temperature, resulting in higher operating costs. Si microreactors

could therefore be useful where safety considerations override the cost concerns, or for producing chemicals by operating in intermediate temperature regimes that cannot be accessed by conventional reactors.

The continuous temperature- power curve of Si microreactors also allow their use as laboratory tools for studying reaction kinetics of exothermic partial oxidation reactions at atmospheric pressures. Studying reaction kinetics at atmospheric pressures in conventional laboratory reactors is limited by the temperature rise after ignition, which results in increased reaction rates, eventually leading to operation in the mass-transport limited regime. $NH_3$ conversion data for Pt catalyzed $NH_3$ oxidation reaction at 1 atmosphere (Figure 5.5) was obtained in the Si microreactor to demonstrate the feasiblity of studying reaction kinetics. For all the data in Figure 5.5., the inlet reactant composition to the reactor was 10% $NH_3$ in $O_2$, with a total flowrate of 20sccm, and the microreactor was maintained at a temperature of 110°C to prevent water condensation on the microreactor walls. The microreactor temperature was increased till the $NH_3$ peak height in the mass-spectrometer dropped, which indicated ignition. Thereafter, $NH_3$ conversion data was collected at a different temperatures. The microreactor temperature could not be increased beyond 325°C because of differential thermal expansion of Pt and SiN which lead to membrane deformation and breakage. Both the Si microreactor and the SiN microreactor break at ~325°C when heated using on-chip resistors. But, the SiN membrane can survive upto 600°C when heated by the reaction exotherm. This is because while the reaction exotherm heats the Pt and the SiN membrane uniformly, the on-chip heater generates large local temperature gradients (the heater segment is much hotter than the edge of the membrane) that leads to large local stress fields. Since the reaction exotherm is conducted away in the Si microreactor, it does not experience high

temperatures. The reaction rate was repeatable with no hysteresis for increasing and decreasing temperatures, within the detection limits of the experimental setup. As a check for the validity of the data, the reaction rate was calculated to be well below the $NH_3$ collision rate on the catalyst surface at 1atmosphere pressure and 300°C (maximum reaction rate=0.5mol/m$^2$/°K, collision rate=3500 mol/m$^2$/°K).

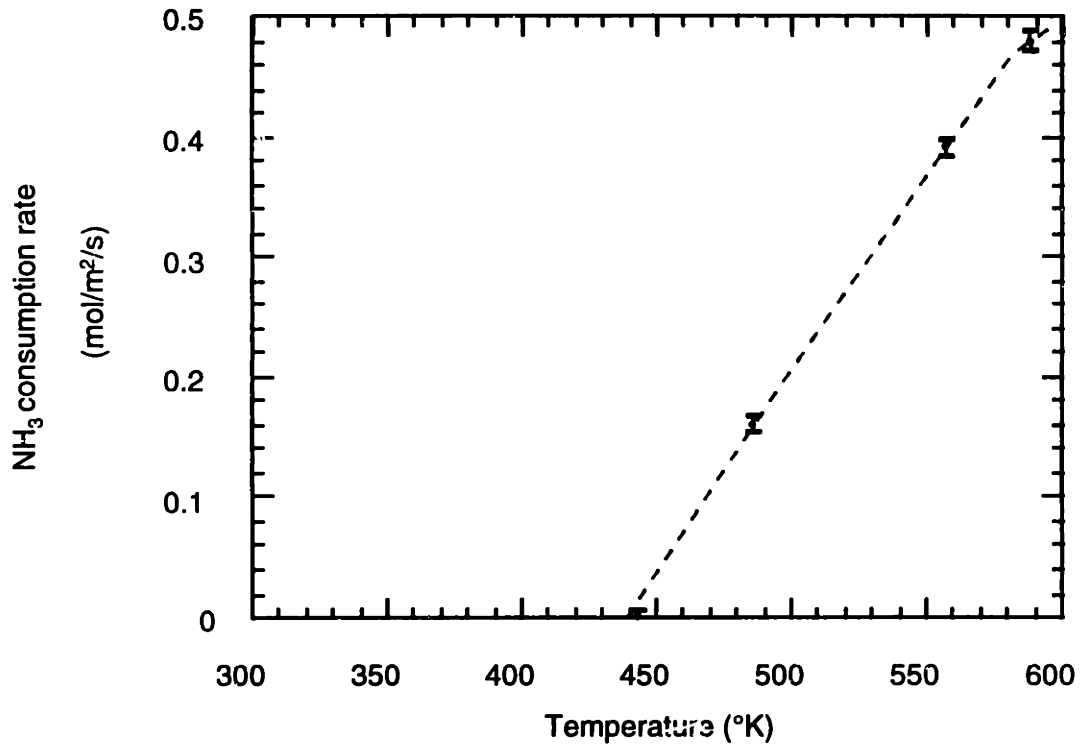


***Figure 5.5** Rate of $NH_3$ consumption as a function of temperature for $NH_3$ oxidation reaction in Si microreactor.*

The limitations of these set of reaction rate data are -

1) The reactant residence times were low (~5ms) due to high flowrates (~20sccm), and were comparable to the reaction times (~1ms), because the delay time in the detection system was too large to measure reactions at low flowrates;

2) The reaction surface area is not well characterized. The reaction rate was calculated on the basis of total Pt catalyst area under the heater segment, but the actual area is larger because of roughness (Section 4.3.2);

3) The catalyst temperature was not uniform, as revealed by simulations (Figure 4.4 ).

All of these issues will have to be addressed before kinetic studies can be reliably carried out in the Si microreactor. The residence time can be increased by modifying and increasing the sensisitivity of the detection system. The reaction surface area could be determined by adsorption studies before collecting reaction kinetics data, and the microreactor redesigned to maintain a uniform catalyst temperature. A simple method to achieve a uniform catalyst temperature is to deposit the catalyst only in the center of the heater zone where the temperature is uniform, as revealed by simulations.

In addition to the experimental limitations mentioned in the previous paragraph, drift in the mass spectrometer peak heights contributed to the experimental error. To quantify the error due to mass-spectrometer drift, $NH_3$- $O_2$ calibration was done immediately preceding and following an experiment, and reaction rate uncertainty due to the variation in peak heights is plotted as the error bar (Figure 5.5).

## 5.2 Shallow-channel Microreactors

Conversion-flowrate studies of Pt catalyzed $NH_3$ oxidation in the SiN microreactor demonstrated that the reaction was limited by diffusion of reactants to the catalyst surface (Section 4.3.2). Furthermore, with increasing flowrates, the $NH_3$ conversion decreased because the reactants bypassed the catalyst (Figure 4.12). Reducing the channel height decreases the diffusion length of the reactants to the catalyst surface, allowing for increased conversion at higher flowrates. To test this concept, conversion-flowrate

comparisons were made using microreactors with two channel heights: a 550 μm high channel reactor referred to as deep-channel microreactor, and a 275μm high channel reactor referred to as shallow-channel microreactor. The deep-channel microreactor was the SiN microreactor described previously (Chapter 2; Figures 2.1 and 2.2). The shallow-channel microreactors was a SiN microreactors with the lower part of the microreactor reaction channel blocked using a micromoulded ceramic insert (Figure 5.6), for decreased channel height. The ceramic insert was placed only in the reaction channel away from the outlet hole to allow gas exit, and not in the flowsensor region.

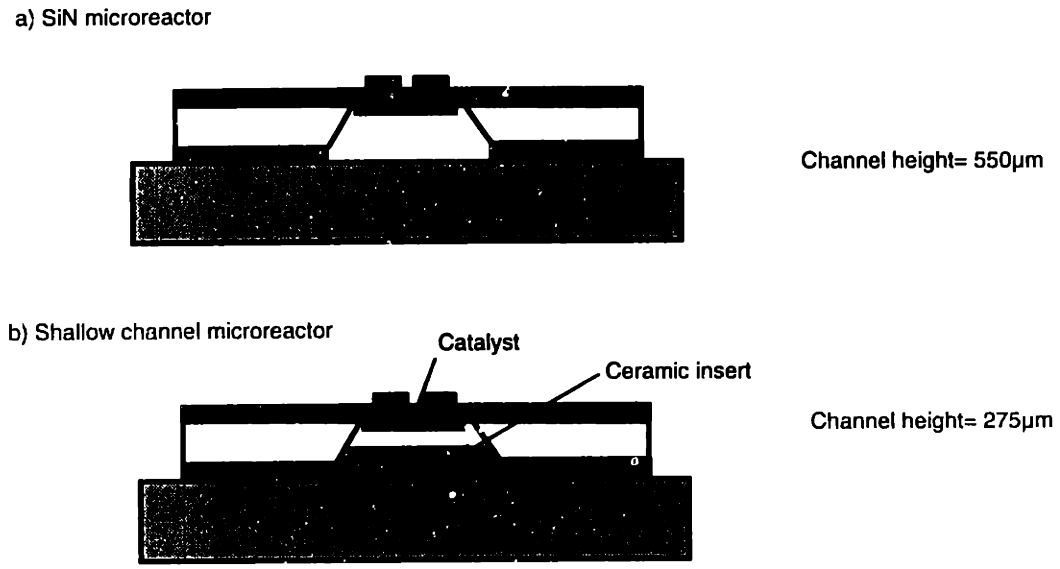


***Figure 5.6*** *Schematic diagram of- a) SiN microreactor and b) Shallow channel microreactor showing the ceramic insert. The enhanced mass transfer in shallow channel microreactors is due to the shorter diffusion length for reactants from bulk gas to catalyst*

### 5.2.1 Device Modeling

Models of varying degrees of accuracy and detail starting from a simple scaling analysis, an analytically tractable model, as well as detailed finite element method (FEM) calculations [3] were developed to understand the conversion-flowrate behavior with varying channel heights. While the scaling arguments provided a quick and simple

analysis and order of magnitude estimates of conversion, the analytical model was more exact and provided an upper bound on the conversion data. The FEM analysis [3] were used to compute the exact numbers.

***Scaling Analysis***

The relative magnitudes of the characterisitic reaction times, diffusion times and residence times were compared in the scaling analysis to predict the trend in the conversion-flowrate behavior of microreactors with changing channel heights. The arguments follow the scaling analysis presented in section 2.2.1. Since the reaction rate is limited by reactant diffusion (section 4.3.2), the characterisitic reactant diffusion time ($\tau_D$) to the catalyst surface is much greater than the characteristic reaction time ($\tau_{rxn}$) (Figure 5.7). At large flowrates, however, the reaction rate becomes residence time limited ($\tau_{res} < \tau_D$), with increasing fraction of the reactions by-passing the catalyst (Section 4.3). Therefore, for complete conversion, the residence time should be larger than the diffusion time ($\tau_{res} >> \tau_D$). The residence time in the reaction channel is given by, $\tau_{res} = L/v$ (Figure 5.7), where L is the length of the heated catalyst segment and v is the average velocity of the gas in the channel. Since the total flowrate, $Q = h \times w \times v$, substituting for v gives, $\tau_{res} = L \times w \times h/Q$, implying that the residence time decreases linearly with decreasing channel height. However, the diffusion time of the reactants to the catalyst surface decreases to the square of the channel height, $\tau_D \sim h^2/D$, where D is the $NH_3$ diffusivity. Mathematically, the criteria for complete conversion ($\tau_{res} >> \tau_D$) gives, $L \times w \times h/Q >> h^2/D$, which reduces to, $L \times w/Q >> h/D$. Therefore, while keeping L, w, and D constant, on reducing h, Q can be correspondingly increased to maintain the inequality criterion for

complete conversion. In other words, reducing the channel height would allow complete conversion even at larger flowrates.

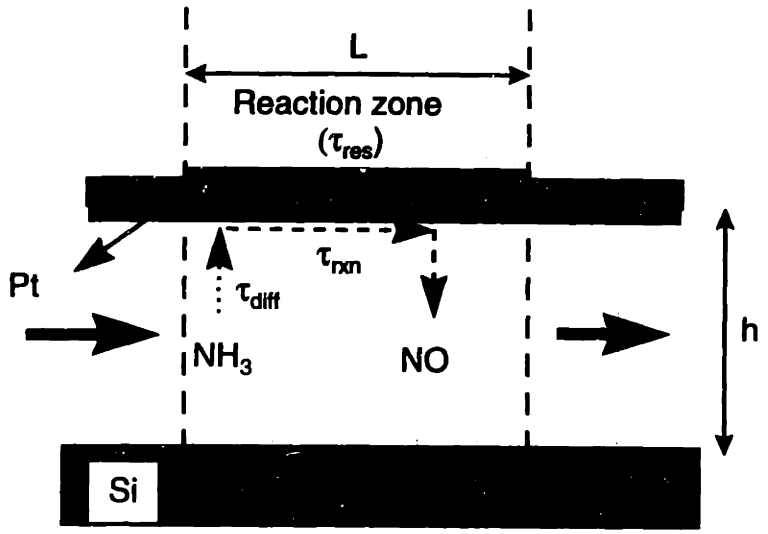


***Figure 5.7** Schematic of microreactor axial cross-section showing the steps of the reaction with the respective time constants.*

The scaling analysis provides order of magnitude estimates and is not exact. Scaling analysis is breaks down in regions where the mass transfer boundary layer is developing, because the characteristic diffusion length in this region is the mass transfer boundary layer thickness and not the channel height, h, as assumed in the scaling analysis. Therefore, at large flowrates, where the mass transfer boundary layer is still developing over a significant length of the reaction zone, the scaling analysis provides incorrect conversion estimates.

***2-D parallel plate extended-Graetz-Nusselt analysis***

2-D modeling was carried out to obtain the conversion upper bound with flowrate for changing SiN microreactor channel height. Simplifications and assumptions were made to reduce the problem to the classic extended-Graetz-Nusselt problem that was analytically tractable. The simplified SiN microreactor geometry used for this model consists of two parallel plates with the catalyst and the heater on the top plate (Figure

5.8), and an inert and impermeable lower plate. Dilute $NH_3$ in $O_2$ mixture entered the reaction zone where $NH_3$ was reacted on the heated catalyst. The goal was to predict the $NH_3$ concentration at the exit of the reaction zone (3.4 mm long).

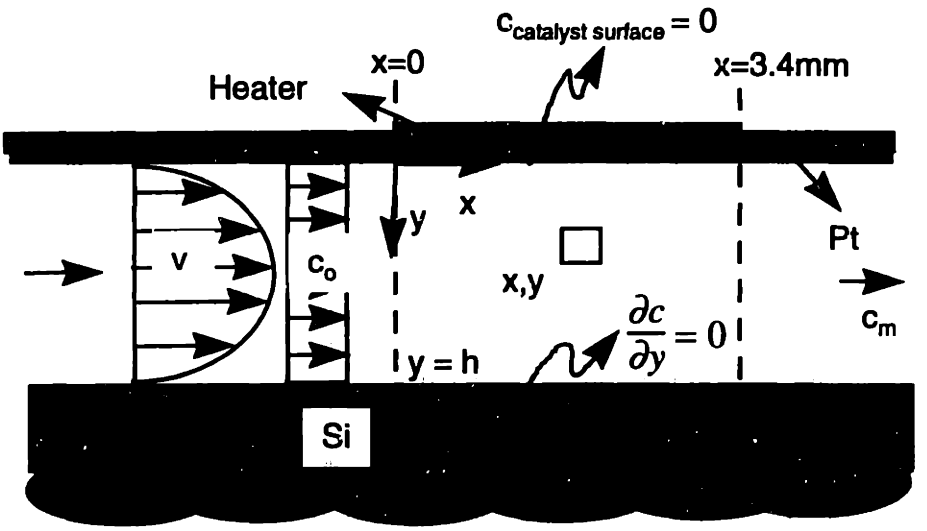


***Figure 5.8** Microreactor schematic axial cross-section showing the boundary conditions used for analytical model.*

Negligible axial diffusion is assumed since Pe ~30 >>1, implying that convection dominates diffusion. Iincompressible flow is assumed even though this is a poor assumption since the temperature increases close to catalyst decreasing the density. This assumption, however, makes the problem analytically tractable. Finally, dilute species are considered since maximum $NH_3$ concentration in experiments is 10%). Writing a differential $NH_3$ balance in the bulk gas (Figure 5.8) with the above approximations yields,

$$\frac{\partial(cv)}{\partial x} - D\frac{\partial^2 c}{\partial y^2} = 0 \qquad (5.1)$$

Where c is the concentration of $NH_3$ at any point x,y in the fluid bulk, v is the local fluid velocity and $D$ is the $NH_3$ diffusivity.

Since $v = v(y)$, the equation 5.1 reduces to,

$$v\frac{\partial c}{\partial x} - D\frac{\partial^2 c}{\partial y^2} = 0 \qquad (5.2)$$

Dedimensionlizing the velocity v with maximum velocity $v_o$, concentration c with inlet concentration $c_o$, and the length variables x and y with channel height h, equation (5.2) reduces to,

$$v^*\frac{\partial c^*}{\partial x^*} - (\frac{D}{v_o h})\frac{\partial^2 c^*}{\partial y^{*2}} = 0 \qquad (5.3)$$

The boundary conditions are:

1) Inlet BC1: $x^* \le 0$, all $y^*$, $c^* = 1$,

2) Constant concentration BC2: $x^* > 0$, $y^* = 0, c^* = 0$,

3) Zero flux BC3: all $x^*$, $y^* = h, \frac{\partial c^*}{\partial y^*} = 0$.

The second boundary condition (BC2) assumption of zero $NH_3$ concentration on the catalyst is valid since the reaction is very fast at high temperatures (T > 400°C), and is consistent with the observation of diffusion limited reaction (Section 4.3.2).

Since the fluid travels several entrance lengths before reaching heater #3, it can be further assumed to be fully developed and parabolic,

$v^* = 1 - (2y^* - 1)^2$, and equation (5.3) reduces to,

$$\frac{\partial c^*}{\partial x^*} - (\frac{D}{v_o h})(\frac{1}{1-(2y^*-1)^2})\frac{\partial^2 c^*}{\partial y^{*2}} = 0 \qquad (5.4)$$

The analogous heat transfer problem (which gives the same differential equations) of flow through parallel plates with a developing *temperature* profile is the classic Graetz-Nusselt problem [4]. The problem has been analytically solved for a variety of boundary conditions, using separation of variables technique, to obtain solutions in the form of eigenfunctions and eigenvalues. These solutions are summarized in [5]. Since the parallel plate extended Graetz-Nusselt problems solved in the literature have symmetric boundary conditions [6] while our boundary conditions are asymmetric, we have adapted the solutions of a flow through an annulus (Figure 5.9) [5] to this problem, with the parallel plate being a special limiting case where the annulus has the same inner and outer radius $(\frac{r_i}{r_o} \rightarrow 1)$.

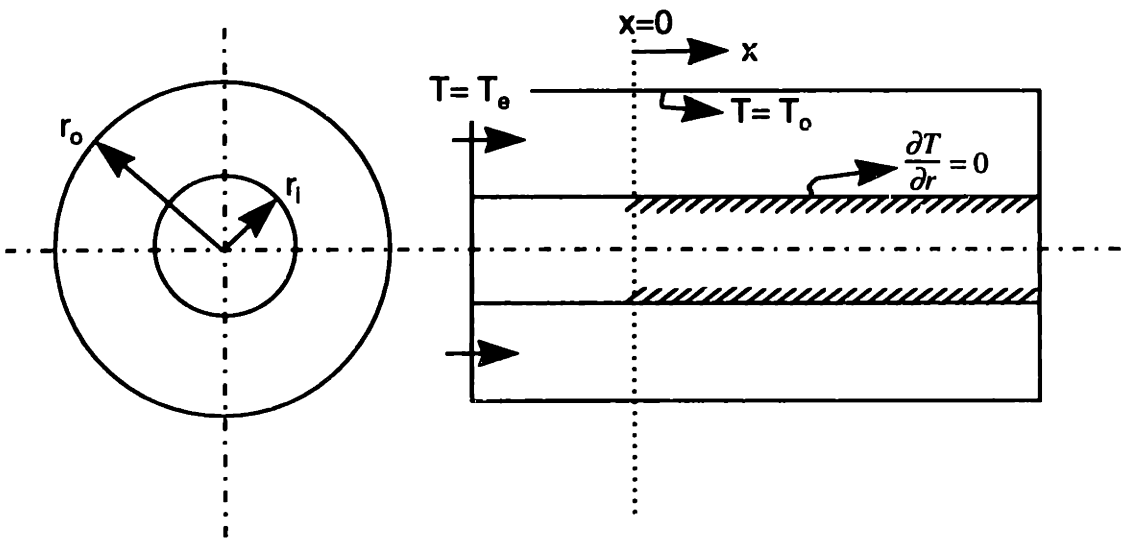


***Figure 5.9*** *Schematic of developing flow through annulus heat transfer problem whose solution was adapted for microreactor developing mass transfer flow.*

The solved mean dimensionless 'temperature' $\theta$ at the exit is tabulated (Table 96) in [5] for different values of the dimensionless x-distance $x^{\pm}$, defined as,

$$x^{\pm} = \frac{x}{Pe \bullet h} \tag{5.5}$$

where $Pe$ is the dimensionless Peclet number,

$$Pe = \frac{v_o h}{D} \qquad (5.6).$$

For our case the dimensionless 'temperature',

$$\theta = \frac{c_o - c}{c_o} \qquad (5.7),$$

where $c$ is the mean concentration of $NH_3$ at the exit of the reaction zone (also referred to as 'mixing-cup' concentration in the literature). Therefore, $\theta$ is the reaction conversion. The solution for $\theta$ (from table 96 in reference [5] is plotted (Figure 5.10) for easy readout.

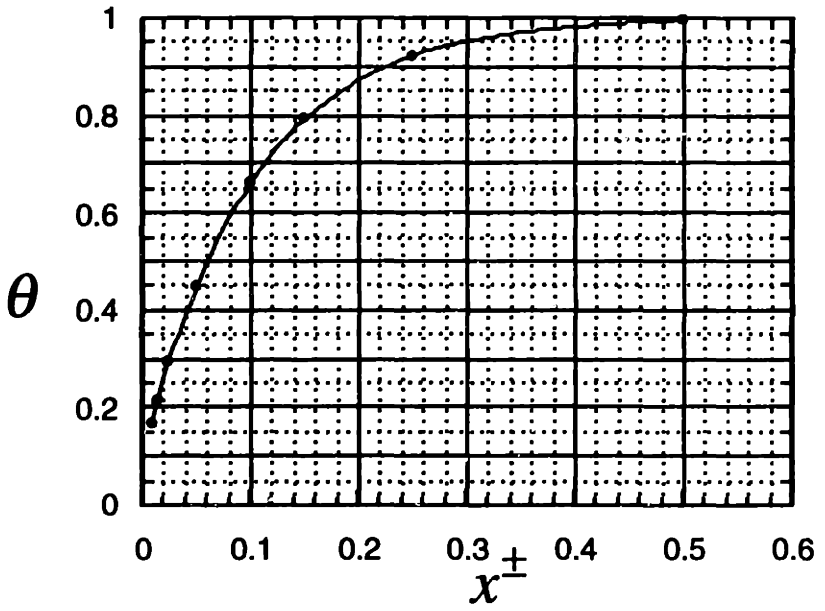


***Figure 5.10*** *Solution to the parallel plate fully developed parabolic flow and developing thermal flow problem. The data is from Table 96 in reference[5].The x-axis is the dimensionless distance and y-axis is the dimensionless temperature, as defined in the text.*

We are interested in the values of $\theta$ at x= 3.4mm, which is the length of the reaction zone. Substituting the expression for Pe, and expressing $v_o$ in terms of flowrate $Q$,

channel height $h$ (550μm or 275μm), and average channel width $w$, $x^{\pm}$ can be reduced to,

$x^{\pm} = \frac{x \bullet D \bullet w}{h \bullet Q} = \frac{3.4mm \bullet 10^{-5}\, m^2/s \bullet 925\mu m}{h \bullet Q}$. The values of $x^{\pm}$ are calculated for different $h$ and $Q$, and $\theta$ is read off the graph (Figure 5.10), to obtain the conversion under different flowrates and for different channel heights (Figure 5.11).

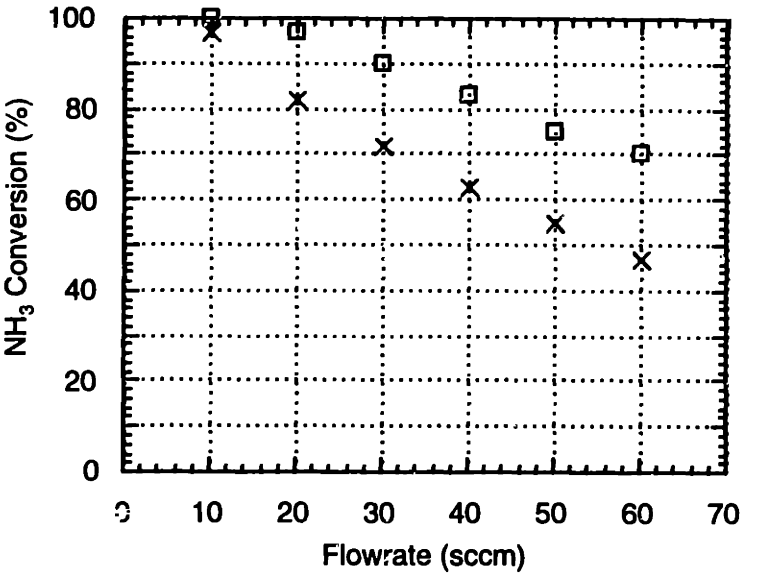


***Figure 5.11*** *The results of the analytical modeling giving the upper bound of the conversion as a function of flowrate for two different channel heights: 275μm ( ) and 550μm ( × ).*

The model predicts a conversion increase of ~20% at flowrates larger than 20sccm, when the channel height is halved from 550μm to 275μm. The model gives the upper bound on the conversion data because:

1) The surface concentration of $NH_3$ is zero, whereas in reality it would be a finite number especially at relatively low microreactor temperatures (300-400°C),
2) The temperature rise of the gas during reaction and the resulting fluid expansion and loss of residence time, would further reduce conversion.

### 5.2.2 Fabrication process

The fabrication process for the SiN microreactor has been described previously (Section 2.3). The micromolding process for the ceramic insert and the packaging scheme is described in this section. The ceramic insert has to be the exact size and shape as the micoreactor channel so that there are no dead volumes and gas stagnation regions. The mould for the ceramic insert was a Si wafer that was microfabricated using a similar process, and the same masks as that used for the SiN microreactor fabrication. The starting material for the micromold (Figure 5.12) was a double-side polished (100 mm diameter, 550 μm thick) silicon wafer. The wafer was coated by low pressure chemical vapor deposition (LPCVD) with 0.1 μm thick low-stress silicon nitride ($SiN_x$) (Sekimoto *et al.*, 1982) that formed the etch mask for the micromold in subsequent steps (step 3 in Figure 5.7). The $SiN_x$ on the backside of the wafer was patterned using photoresist, and plasma etched (in $SF_6$) to expose the underlying silicon in the T-shaped channel regions (step 3). The mold was formed by etching bulk of the silicon (exposed on the backside of the wafer) in KOH solution (20% by weight in water at 90°C) to a depth of 275μm (desired ceramic insert thickness).

Silicone mold-release (Cotronics Corporation, 3379 Shore Parkway, Brooklyn, N.Y. 11035, 718-646-7796), was spray coated on the mold, following which a ceramic slurry of $Al_2O_3$ particles (<50μm size) in water (~1:1 ratio by volume of $Al_2O_3$ to water) was poured into the mold. The $Al_2O_3$ powder was supplied by Cotronics Corporation (Part information: Precision Castable Alumina Ceramic, RTC-70). Larger particles resulted in grainy ceramic insert that caused difficulty in packaging by preventing a good seat of the microreactor to the sealing plate. While excess $Al_2O_3$ to water ratio slurry was difficult to

pour into the mold uniformly, excess water resulted in brittle ceramic inserts that were difficult to handle. The water was supplied by Cotronics Corporation (Activator RTC-70), but regular 'tap-water' was also successfully used.

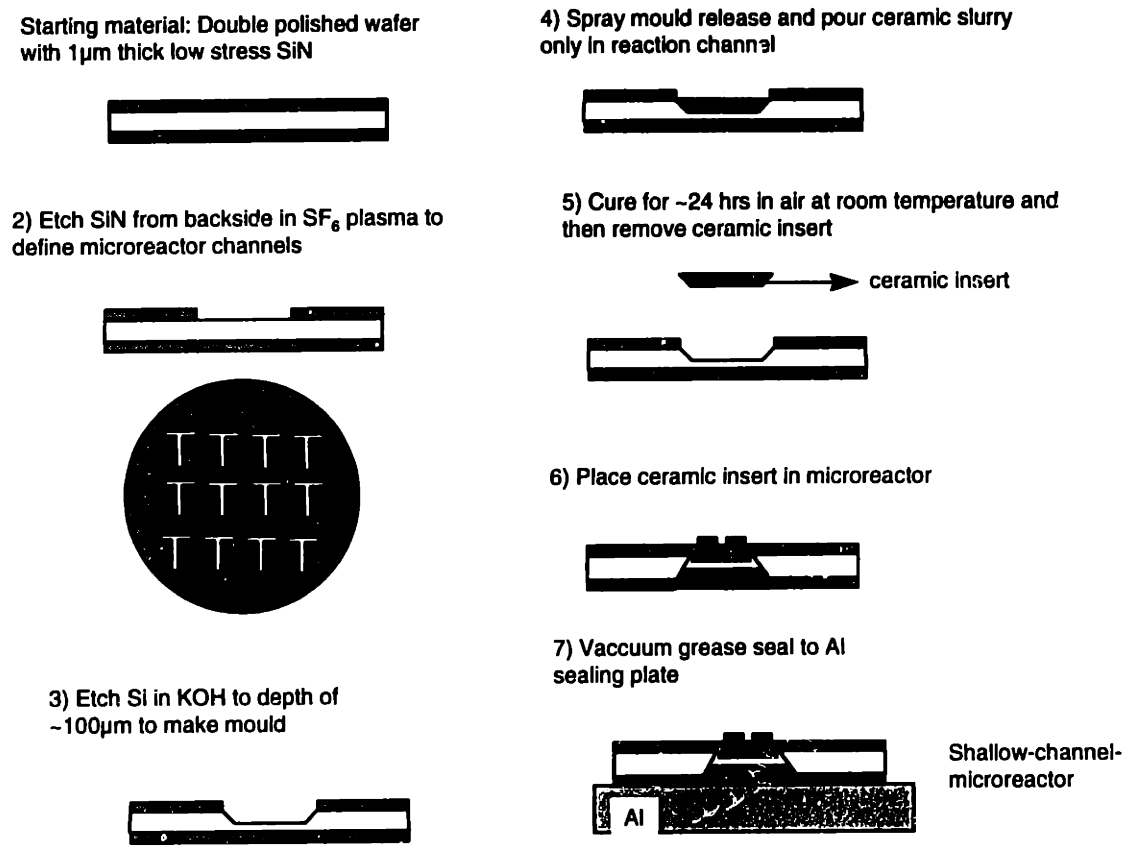


***Figure 5.12** Fabrication process of Si micromold and the ceramic insert.*

The ceramic slurry in the mold was leveled using a spatula to ensure that the mold height is exactly reproduced in the finished ceramic-insert. Ceramic inserts with excess thickness also prevented good seal of the microreactor to the sealing plate. The slurry was cured at room temperature for ~48 hours before the solid ceramic insert was released from the mold using a spatula. In the realease process, ceramic inserts of ~5mm length consistently survived while longer inserts sometimes broke. The ceramic insert was then packaged in the SiN microreactor. The ceramic insert was not subject to a high-temperature cure because the room-temperature cured ceramic insert has sufficient

mechanical strength and integrity. In addition, the dimensions of the high-temperature cured ceramic insert would have decreased due to sintering, requires characterization of the shrinkage and designing new molds to account for the shrinkage. The molds were reused after removing the silicone mold release by soaking in acetone, followed by a water rise and drying using pressurized $N_2$.

The ceramic insert was placed using tweezers into the reaction channel of an inverted SiN microreactor (to prevent the insert from falling-off), and an Al sealing plate was placed on the inverted SiN microreactor with ceramic insert. The T-channel was then aligned to the 3 inlet-outlet holes in the base-plate and sealed using vacuum grease (Dow Corning High Vacuum Grease, Dow Corning Corporation, Midland, MI 48640). The vacuum grease allowed differential thermal expansion between the Al base-plate and the SiN microreactor, preventing breakage when the microreactor was externally heated during experiments.

### 5.2.3 Shallow-channel Microreactor Testing

The goal of this study was to make comparions of conversion-flowrate behavior, for the shallow and deep-channel microreactors. The test setup and testing procedure has been described previously (Chapter 3). The microreactor was externally heated to 150°C to prevent water condensation.

The catalyst activation procedure described previously (Section 3.4) was carried out before data collection. For the conversion-flowrate experiments in this study, the same microreactor was used as the deep-channel microreactor, and later repackaged with ceramic insert to be used as shallow-channel microreactor. The use of the same

microreactor allowed conversion-flowrate comparisons by isolating the effect of channel height, without the uncertainty of conversion variations due to catalyst area and activity.

***Test results***

External heating of the microreactor changed the ignition-extinction behavior compared with unheated microreactor operating at room temperature (Section 4.3.1; Figure 4.13). In the unheated microreactor, 10% $NH_3$ in $O_2$ mixtures were routinely ignited, and the ignition front was localized to the active heater segment . However, upon ignition of 10% $NH_3$ in $O_2$ in the externally heated microreactor (T=110°C), the ignition front was not restricted to heater #3 and moved upstream to the mixing point at the reaction channel entrance.

Therefore conversion-flowrate experiments in externally heated microreactors was carried out at a low inlet composition of 5% $NH_3$ in $O_2$, to restrict the ignition front to heater #3. To detect the upstream movement, the temperature sensors on heaters 1&2 (Figure 2.1) were monitored, and any temperature rise after ignition indicated an upstream movement of the ignition front.

In all the experiments for both deep-channel and shallow-channel microreactors, the downstream temperature sensor ($T_{32}$) was maintained at 325±25°C. Typically, higher power was needed to maintain this temperature for the shallow-channel (Power ~ 260 ± 10 mW) than for the deep-channel SiN microreactor (155±25mW), because of better heat transfer for shallow-channel microeactors due to shorter heat conduction path via the gas in the channel to the cold floor of the channel (Figure 5.6).

Results indicate that decreasing the channel height by 50% enhances the conversion by ~10%, with increasing differences at larger flowrates (Figure 5.13). The conversion is ~100% at flowrates less than 15sccm for both the shallow channel and the normal SiN

microreactor, because the residence time is much larger than the diffusion time of the reactants. However, at larger flowrates, the conversion achieved with the shallow-channel microreactors is higher than deep-channel microreactors, with increasing difference with flowrate, confirming the hypothesis of enhanced conversion due to shorter diffusion length.

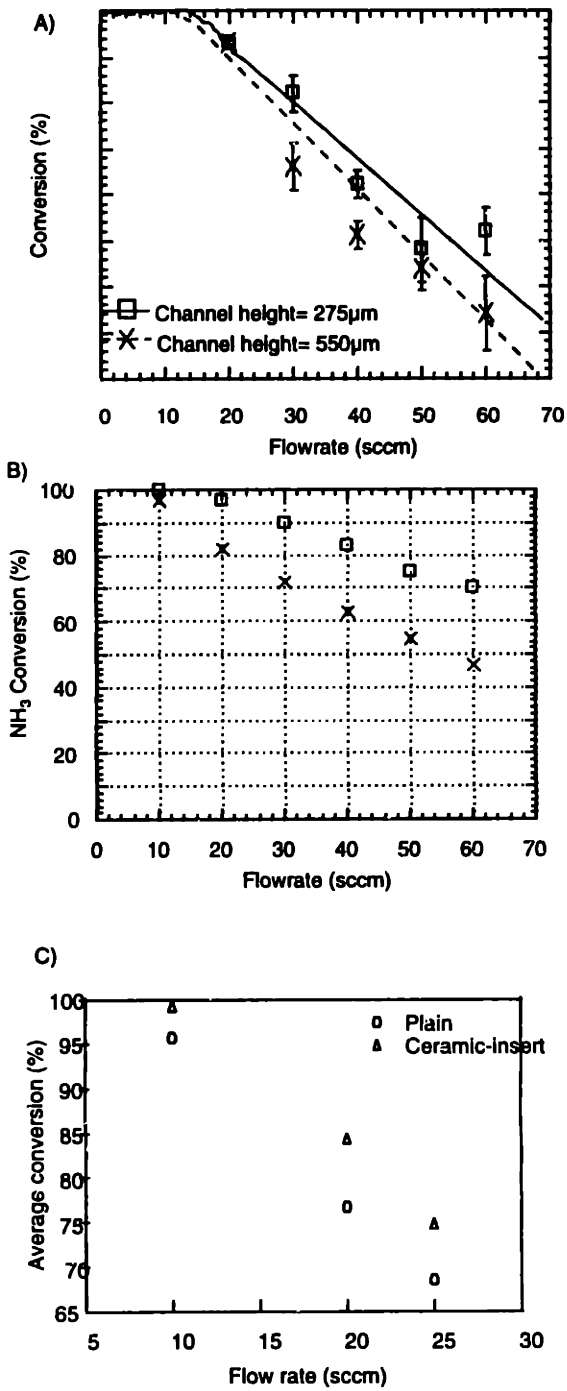


***Figure 5.13*** *A) Conversion-flowrate test results for 5% $NH_3$ in $O_2$ mixtures as a function of varying microreactor channel heights. The conversion is enhanced for shallow-channel microreactor. Conversion-flowrate values predicted by B) Graetz-Nusselt analysis, and C) FEM simulations (Courtesy- I-Ming Hsing).*

Comparison with the 2-D analytical model results (that provide conversion upper bound) show that the experimentally observed conversions are consistently lower than the model predictions by ~15% for both channel heights (except for one data point -20sccm, 550μm high channel, 93% observed conversion, which is rejected as an anomaly).

Significant simplifying assumptions were made in the 2-D parallel plate analysis. In particular, the assumption of incompressible flow and constant temperature, although incorrect, provided an upper bound on the conversion. For exact predictions of the conversion, detailed Galerkin Finite Element simulations were carried out for changing channel height [3]. Simulations of unheated microreactor (that is at ambient temperature) show a conversion increase of ~10% by decreasing the channel width by 50%, consistent with experimental observations. The absolute value of the conversion matches experimental observations within 10%. Simulation at flowrates higher than 25 sccm could not be carried out due to numerical instabilites associated with high Reynolds numbers [3].

The results obtained in this study suggest further experiments to explore the effects of reaction rates on decreasing the channel height further (< 50μm), to determine the critical channel height at which the reaction is rate limiting. While the ceramic micromolding technique used in this study is a useful tool for simple and fast laboratory studies, it is unsuitable for large scale production of shallow-channel microreactors, which requires a robust process that does not need handling of delicate ceramic moulded inserts. The ceramic micromolding technology could be further developed for more robust processing, or alternative micromachining designs could be used to change the channel height.

## References

[1] W. R. Williams, M. T. Stenzel, X. Song, L. D. Schmidt, "Bifurcation behavior in homogeneous- heterogenous combustion: I. Experimental results over Platinum," *Combustion and Flame*, vol. 84, pp. 277, 1991.

[2] T. Pignet and L. D. Schmidt, "Selectivity of ammonia oxidation on Pt," *Chemical Engineering Science*, vol. 29, pp. 1123-1131, 1974.

[3] I.-M. Hsing, "Simulation strategies for microfabricated chemical systems," Ph.D. thesis in Chemical Engineering. Cambridge, MA: Massachusetts Institute of Technology, 1997.

[4] M. Jacob, *Heat Transfer*, vol. 1. New York: John Wiley & Sons, 1949.

[5] R. K. Shah and A. L. London, *Laminar Flow Forced Convection in Ducts*. Ney York: Academic Press, 1978.

[6] J. R. Sellars, M. Tribus, and J. S. Klein, "Heat Transfer to Laminar Flow in a Round Tube or Flat Conduit- The Graetz Problem Extended," *Transactions of ASME*, vol. 78, pp. 441-448, 1956.

# Chapter 6 Conclusions and Recommendations for Future Work

## 6.1 Conclusions

Microfabrication technology allows manufacture of novel chemical reactors having several advantages over conventional techniques. Micromachined chemical reactor systems offers distributed point-of-use chemical manufacturing for safer operation without storage and transportation hazards, ability to tailor reactor geometries of submillimeter to micron dimensions for improved performance, improved process control by integrated sensors and actuators, and shorter development time from laboratory to chemical production.

To test these concepts, a prototype microreactor having submillimeter channels with integrated heaters, flow and temperature sensors was microfabricated on silicon. Test results using Pt catalyzed $NH_3$ oxidation as model reaction demonstrate feasibility of conducting chemical reactions in the microreactor. $NH_3$ oxidation reaction exhibits ignition-extinction behavior in the micoreactor, consistent with behavior in conventional reactors. Conversion-selectivity studies show that the microreactor operation for $NH_3$ oxidation is mass transfer limited. Experiments and simulations indicate that one of the unique features of the microreactor is the localized reaction hot-zone, while the channel walls and the bulk of the chip is at room temperature. This could potentially make microreactors safer to operate than conventional reactors by suppressing flame formation due to quenching of gas phase radicals on the cold reactor walls. Several highly flammable gas mixtures without diluents (*e.g.*, 20% $H_2$ and $O_2$, $NH_3$ and $O_2$ at all

compositions, $C_2H_6$ and $O_2$ at all compositions) were ignited in the microreactor, without an explosion, demonstrating the safety potential of the microreactor.

Based on the preliminary results of the prototype SiN microreactor, novel microreactor designs for improved heat transfer (Si membrane microreactor) and improved mass transfer (Ceramic insert microreactor) were implemented. Test results using $NH_3$ oxidation as a model reaction show that the Si membrane microreactor does not exhibit temperature rise after ignition due to its excellent heat transfer characteristics. This allowed operation in low temperature regimes inaccessible by conventional reactors, for improved safety and improved product distribution. While $N_2$ and NO are the primary products of $NH_3$ oxidation reaction in conventional reactors, significant amount of $N_2O$ was also produced in addition to NO and $N_2$ in the Si membrane microreactor. Improved mass transfer in the ceramic insert microreactor was achieved by reducing the diffusion length of the reactants to the catalyst.

## 6.2 Recommendations for future work

Future research on the microreactors are required on two fronts: 1) Microreactor-level designs for improved performance, for increased lifetimes, for new chemistries and applications, and 2) Microreactor packaging and scale-up.

### 6.2.1 Microreactor design improvements

***Improving microreactor lifetimes***

The current microreactor designs have membranes that are fragile and prone to breakage. The membrane strength could be improved by avoiding sharp corners that cause stress-concentrations, and by changing the intrinsic stress. The membrane deforms

and eventually ruptures during high temperature operation due to differential thermal expansion of Pt and the membrane. The membrane deformation and breakage could be reduced by using materials whose thermal expansions are matched and by fabricating tethered thermal microstructures that would allow thermal expansions. Alternatively, new microreactor designs that do not use membranes could be investigated. The Pt thin film heater exhibited degradation due to diffusion at high temperatures (>600°C) [1]. Further work is necessary to improve high-temperature thin film lifetimes by the use of diffusion barriers or stable alloys.

***Microreactor designs for improved chemical performance***

New microreactor designs that incorporate the unique advantages offered by microfabrication technology- 1) Integration of sensors and actuators such as valves on chip, 2) Tailoring reaction channel geometry for improved heat and mass transfer, could be implemented. The use of sensors and valves could improve reactor process control and increase safety. For example, an integrated microvalve could be shut off when the sensors detect a runaway condition. The small time constants of the microreactor actuators such as heaters and valves due to their low inertia and small dimensions, offers operation in transient unsteady regimes. Studies in the literature have reported improved performance (conversion and selectivity) by operating reactors an unsteady regime [2].

The ability to tailor reaction channel geometry has been used in the current microreactor design for on-chip mixing that improves safety by preventing flash-back. Since the shape of the reaction channel affects the transport properties, tailoring the reaction channel geometry also offers the ability to tailor the heat and mass transfer. For example, a modified SiN microreactor having a diverging reaction channel (Figure 6.1)

(which could be implemented using the newly available high density plasma etcher from STS technologies ) would have decreasing heat transfer along the channel length. In conventional reactors, since the heat transfer is uniform along the reactor length, the temperature is maximum at the reactor entrance due to the presence of fresh reactants. The temperature rapidly drops along the reactor as the reactants are depleted, leading to an undesirable temperature profile. In many reactions, e.g. ethylene to ethylene oxide, it is desired to have a uniform temperature profile for maximum selectivity. The proposed diverging channel micoreactor would be able to maintain a uniform temperature profile.

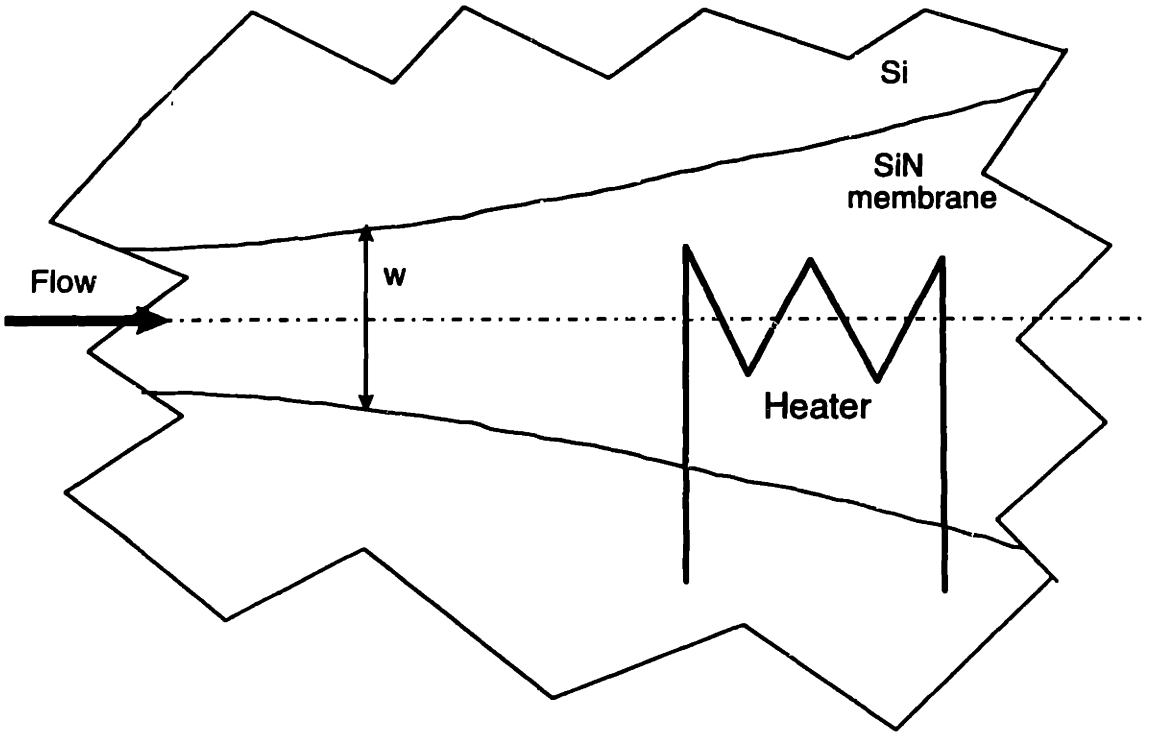


***Figure 6.1*** *Proposed diverging channel microreactor for uniform axial temperature profile. The upstream sections have narrow membrane width for enhanced heat transfer, while the downstream sections have good thermal isolation.*

The diverging channel microreactor would also have improved power efficiency compared with current microreactor designs. The current microreactor designs involved a

trade off in providing sufficient thermal isolation for resistive heating of the catalyst, and providing heat removal capability of reaction exothermicity (Section 2.3.1), leading to lower operating efficiency. By placing the resistive heater in the downstream sections of the reaction channel that has increased thermal isolation, the ignition temperature could be reached at low powers. SiN microreactor tests showed that the reaction front moved upstream upon ignition (Section 4.3.1, Figure 4.10), due to the presence of fresh reactants upstream. In the diverging channel, the ignition front would travel to the region upstream where ignition front is self-sustaining, that is the membrane heat transfer is exactly balanced the heat of reaction. Further upstream of this reaction zone, the ignition front would be unstable since the membrane heat transfer would exceed the heat of reaction.

***Microreactor as laboratory tools***

While further research is necessary to use the microreactors for chemical production, the current microreactor designs could be used as laboratory tools for kinetic studies and catalyst screening. The advantages provided by microreactors as laboratory tools include safety, low reactant usage, less waste, and well-defined geometries that allow relatively simple simulations for better understanding of reaction kinetics. Studying reaction kinetics at atmospheric pressures in conventional laboratory reactors is limited by the temperature rise after ignition, which results in increased reaction rates, eventually leading to operation in the mass-transport limited regime. The continuous temperature-power curve of Si microreactors also allow their use as laboratory tools for studying reaction kinetics of exothermic partial oxidation reactions at atmospheric pressures.

The silicon microreactor could also be used for ignition-extinction studies. Currently, there is a debate in the literature whether the ignition-extinction behavior is

caused by thermal feedback or kinetic feedback. The two effects cannot be decoupled in current laboratory reactors. By preventing a temperature rise after ignition, the Si microreactor could be used to identify the origins of ignition for different reactions.

***Alternative fabrication technologies for microreactors***

The prototype microreactor used a single-crystal Si wafer as a starting material since the microfabrication technology for Si is relatively well established. While the single-crystal Si wafer has excellent thermal conductivity (comparable to metals) for heat removal and has high strength, it places the upper limit on temperature of operation at ~1100°C. The use of alternative materials such as ceramics could allow high temperature operations needed for several of the partial oxidation reactions carried out in the industry. For some applications such as commodity chemical production, the use of single-crystal silicon wafer as starting material and the use of many of the microfabrication steps such as lithography could be prohibitively expensive. Many of the advantages offered by lithography- the ability of create several microreactor channels in parallel, could be achieved by alternative parallel fabrication technologies such as molding and stamping. While stamping has low parts resolution (~1mm), injection molding techniques used to manufacture Compact Disks has micron-scale resolution and could be adapted to microreactor fabrication[3]. Molding and stamping, however, would have the disadvantage of not being able to integrate sensors and actuators.

### 6.2.2 Scaleup of microreactors

Developing an efficient packaging scheme that provides fluid transport and electrical interconnections to the many thousands of microreactors operating in parallel is critical for successful scale-up and commercialization of microreactors. The microreactor

packaging could be achieved at the wafer level (Figure 6.2A) or at the individual chip level (Figure 6.2B). Wafer-level packaging for fluid delivery has been demonstrated by DuPont [4] and is being pursued by PNNL [5]. But these wafer-level packages do not allow electrical interconnections. Two new packaging schemes being developed for the microfabricated chemical analysis devices could be adapted for microreactor use for chip level integration. Both the packaging schemes are analogous to the printed circuit boards used by the electronics industry. Researchers at the University of Twente have proposed a 'mixed-circuit-board' that provides both electrical and fluidic interconnections to the microreactor [6]. Abbot laboratories have developed a compact fluid delivery system ( Fluistor ® board) for 10-100 micro-analytical devices [7]. Fluid flow can be regulated using on-off valves that are integrated on-board. This technology does not provide electrical interconnections. Clearly, further work is required to develop the packaging technology if microreactors are to be used for chemical production.

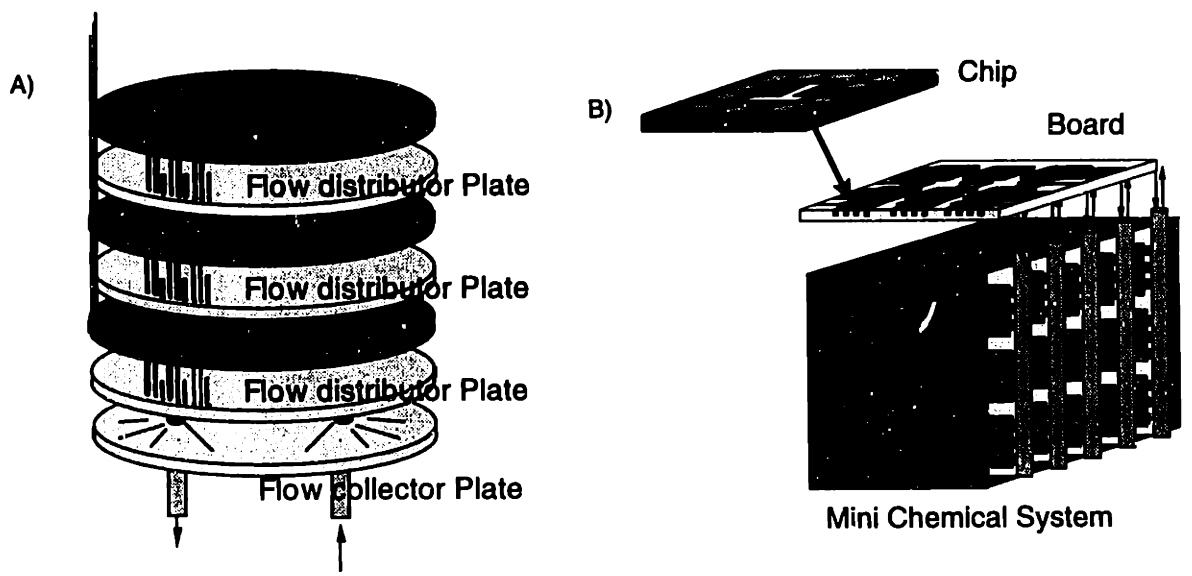


***Figure 6.2** Scale-up and packaging schemes for microreactor. A) Wafer level integration fo microreactors, and B) Chip level integration using printed circuit board analogy.*

The scale-up by replication, or 'scale-out' of microreactors offers several advantages over conventional routes of scale-up, and should be pursued. Since each microreactor would behave exactly alike, individually and in replicated units, scale-up would be considerably shorter and less expensive, allowing for faster time to market, and flexible operation in the event of sudden changes in product demand. Integration of sensors and valves on-chip offers additional flexibility. In the event of a malfunction, a single microreactor could be valved-off and replaced with a functioning microreactor with minimal disturbance to chemical production. In contrast, a conventional large unit would have to be shut down with loss of production and potential dangers of runaway conditions associated with reactor shut-down and start-up.

In summary, microfabrication offers several advantages over conventional reactor technologies. Additional studies of are needed to evaluate the cost and specific application areas for this technology.

## References


[1] S. L. Firebaugh, K. F. Jensen, and M. A. Schmidt, "Investigation of high temperature degradation of Pt thin films with an in-situ resistance measurement apparatus," *Journal of MicroElectroMechanical Systems.*

[2] Y. S. Matros, "Forced unsteady-state processes in heterogeneous catalytic reactors," *Canadian Journal of Chemical Engineering*, vol. 74, pp. 566-579, 1996.

[3] O. Larsson, O. Öhmann, Å. Billman, L. Lundbladh, C. Lindell, and G. Palmskog, "Silicon based replication technology of 3D-microstructures by conventional CD-

injection molding techniques," presented at The 7th International Conference on Solid-State Sensors and Actuators, Chicago, 1997.

[4] J. J. Lerou, M. P. Harold, J. Ryley, J. Ashmead, T. C. O'Brien, M. Johnson, J. Perrotto, C. T. Blaisdell, T. A. Rensi, and J. Nyquist, "Microfabricated Minichemical Systems: Technical Feasibility," presented at Microsystem Technology for Chemical and Biological Microreactors, Mainz, Germany, 1996.

[5] R. S. Wegeng, C. J. Call, and M. K. Drost, "Chemical system miniaturization," presented at Spring National Meeting of the AIChE, New Orleans, 1996.

[6] A. v. d. Berg, T. S. J. Lammerink, V. Spiering, and W. Olthuis, "Modular Concept for Miniature Chemical Systems," presented at Microsystem Technology for Chemical and Biological Microreactors, Mainz, 1996.

[7] D. VerLee, A. Alcock, G. Clark, T. M. Huang, S. Kantor, T. Nemcek, J. Norlie, J. Pan, F. Wadsworth, and S. T. Wong, "Fluid circuit technology: Integrated interconnect technology for miniature fluidic devices," presented at Solid-State Sensor and Actuator Workshop, Hilton Head. SC, 1996.

# Appendix A 1-D Heat transfer fin model to determine membrane width

A 1-D heat transfer fin model was used to obtain an initial estimate of the microreactor membrane width that could provide sufficient thermal isolation for resistive heating of the catalyst. The membrane was modeled as a 1-D fin (Figure A.1), and the calculated characteristic fin length ($L_{fin}$) was used as the membrane width estimate. Writing a heat balance across a differential element in the fin,

$$(-k_{SiN} \cdot t_{SiN} \cdot \frac{\partial T}{\partial x})\Big|_x + (k_{SiN} \cdot t_{SiN} \cdot \frac{\partial T}{\partial x})\Big|_{x+dx} - h_{air} \cdot (T - T_o) \cdot dx = 0 \qquad \text{(A.1)}$$

$$\therefore k_{SiN} \cdot t_{SiN} \cdot \frac{\partial^2 T}{\partial x^2} = h_{air} \cdot (T - T_0) \qquad \text{(A.2)}$$

The heat transfer coefficient of air was estimated by,

$$h_{air} \approx \frac{k_{air}}{H} \qquad \text{(A.3)}$$

De-dimensionlising equation (A.2), with the distance de-dimensionlised by the characteristic fin length, $L_{fin}$, and temperature with $(T_{\max} - T_0)$, we get,

$$k_{SiN} \cdot \frac{t_{SiN}}{L_{fin}^2} \cdot \frac{\partial^2 \theta}{\partial X^2} = \frac{k_{air}}{H} \cdot \theta \qquad \text{(A.4)}$$

Equating dimensional quantities on both sides of the equality, we get,

$$k_{SiN} \cdot \frac{t_{SiN}}{L_{fin}^2} = \frac{k_{air}}{H} \qquad \text{(A.5)}$$

$$\therefore L_{fin} = \sqrt{\frac{k_{SiN} \cdot t_{SiN} \cdot H}{k_{air}}} \qquad \text{(A.6)}$$

$$L_{fin} = \sqrt{\frac{14 \cdot 1 \times 10^{-6} \cdot 550 \times 10^{-6}}{0.046}}$$ (All units in S.I)

$$\therefore L_{fin} \approx 400\mu m.$$

This analysis indicates that at $x = 400\mu m$ ($L_{fin}$), the fin temperature drops significantly. Therefore, a membrane ~800μm wide ($w \sim 2 \cdot L_{fin}$, since the x=0 in fin model is at the membrane center-line) would provide sufficient thermal isolation to allow resistive heating to ignition temperatures. We chose a membrane width of 500μm (w), to allow for better removal of heat of reaction.

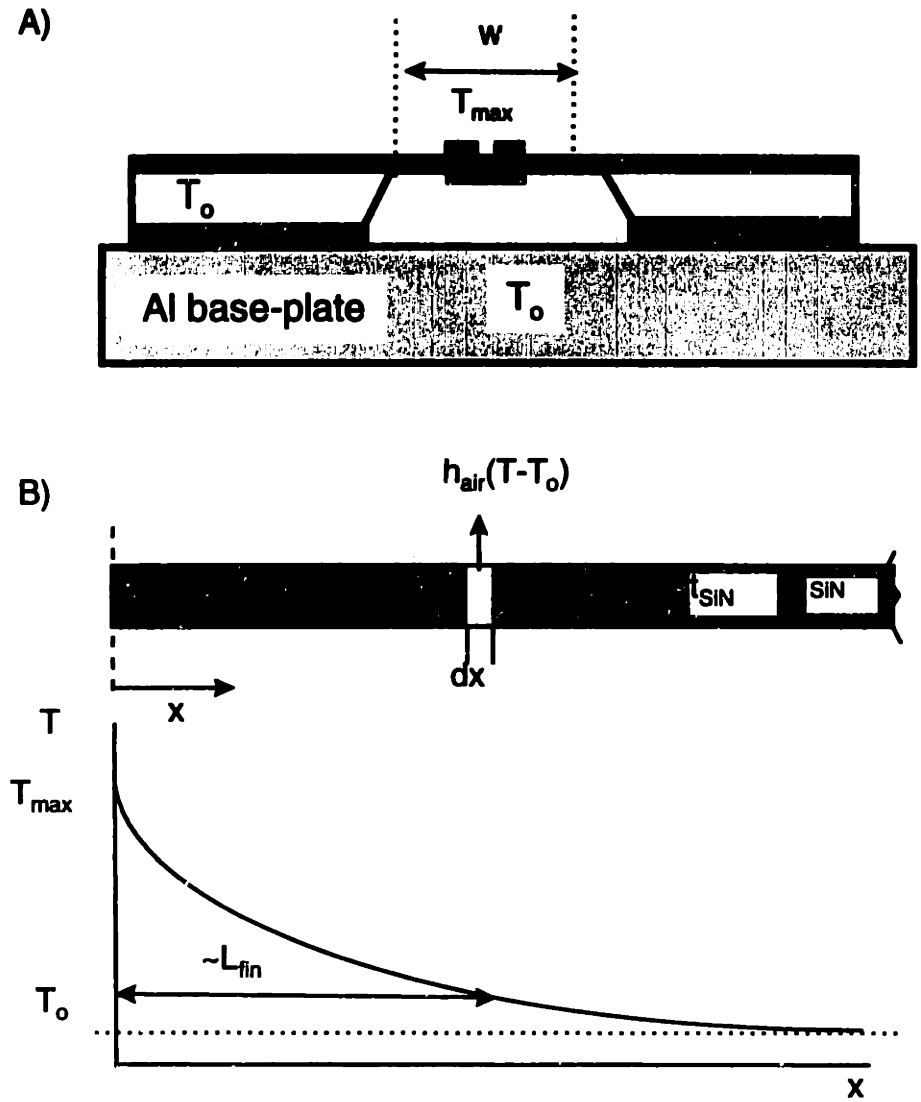


***Figure A.1*** *A) Schematic of the microreactor cross section. B) Schematic of membrane width that was modeled as 1-D fin, with the expected temperature profile and the characteristic fin length ($L_{fin}$).*

# Appendix B

# Lithography Masks Used for Microreactor Fabrication

The microreactor fabrication process involved 2 masks (+1 shadow mask). They are included in this appendix. All the masks were 1:1 contact masks.

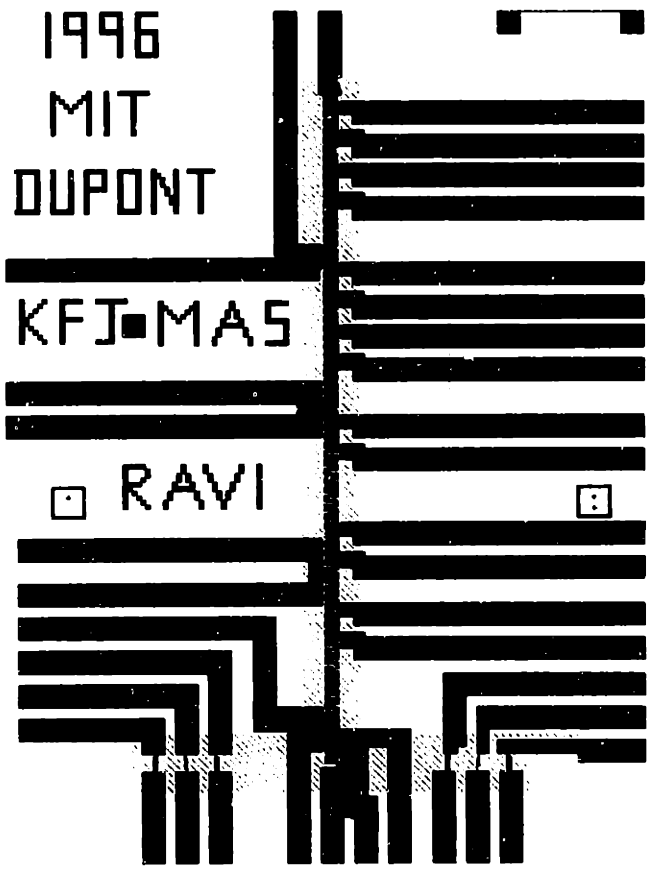


***Figure B.1*** *Mask printout of one chip having the channel and the metal mask overlaid. Each wafer produced twelve chips. The alignment marks (+) were 10 μm wide.*

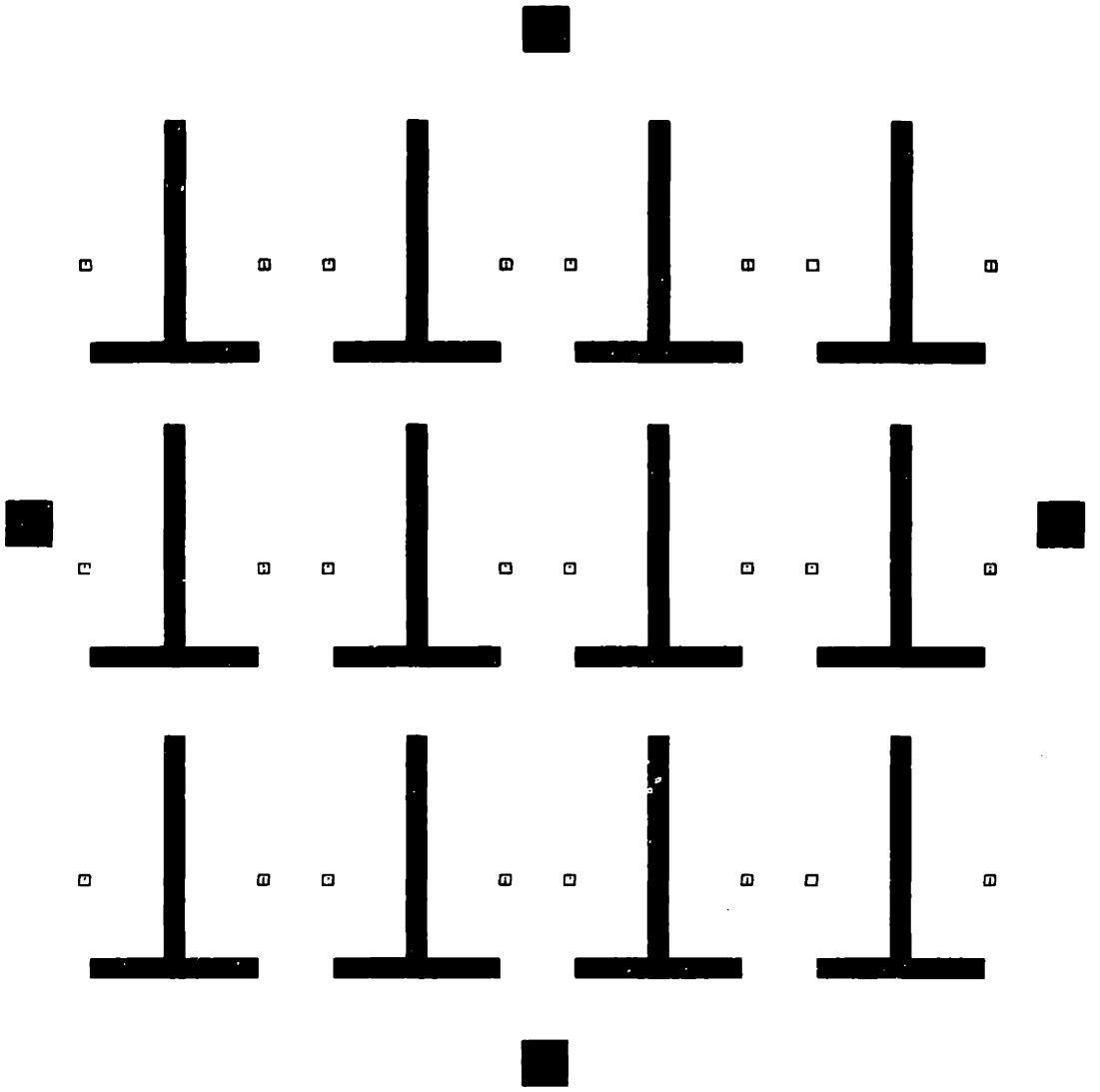

***Figure B.2** Mask(dark field) used to define microreactor channel. The dimension of the pattern was 1.3mm, which resulted in a 500 μm wide membrane after the anisotropic KOH etch. The four square structures at the edge of the mask were holes for uv epoxy used for shadow mask alignment (Section 2.4).*

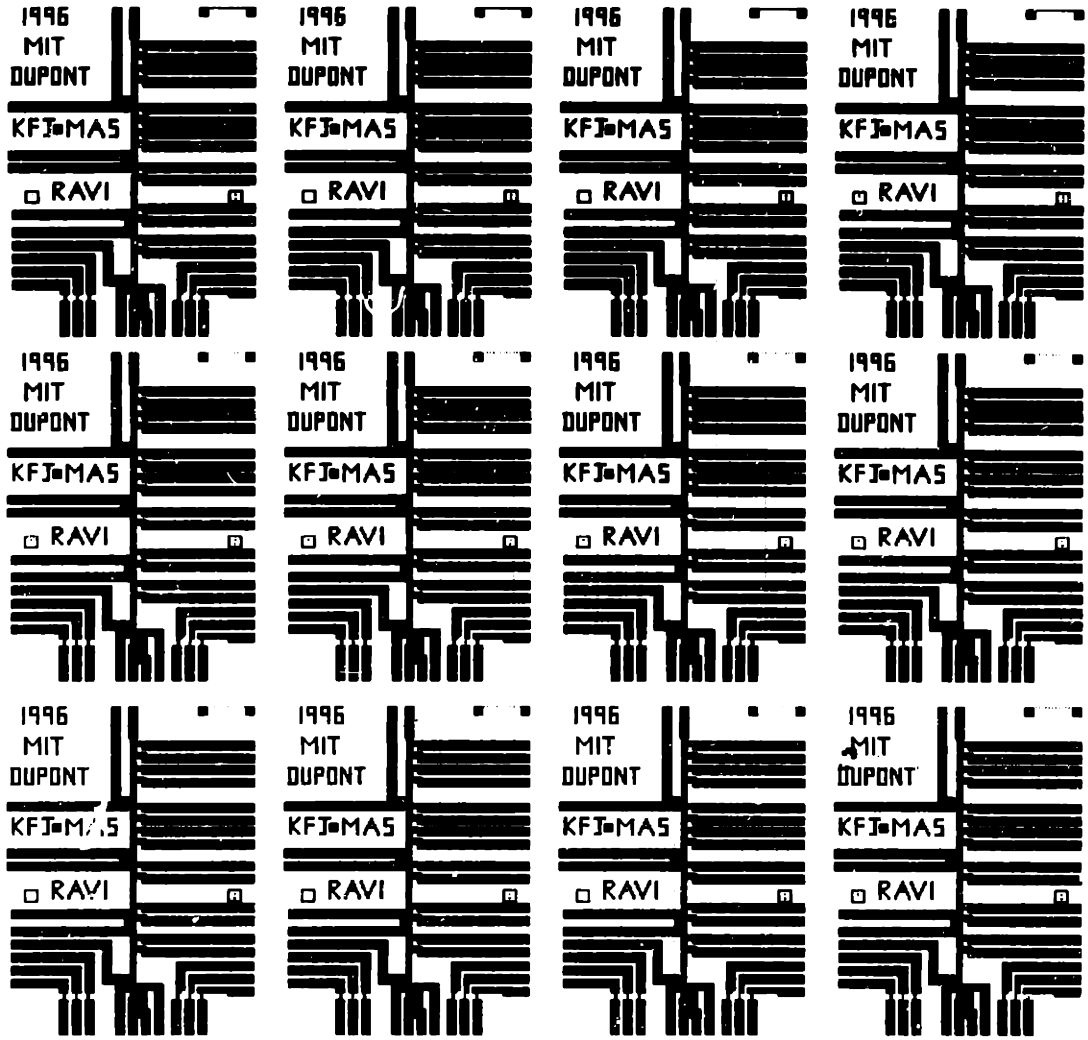


***Figure B.3** Metal mask (clear field for lift-off process) used for microreactor fabrication. The minimum linewidth of this mask was 10μm.*

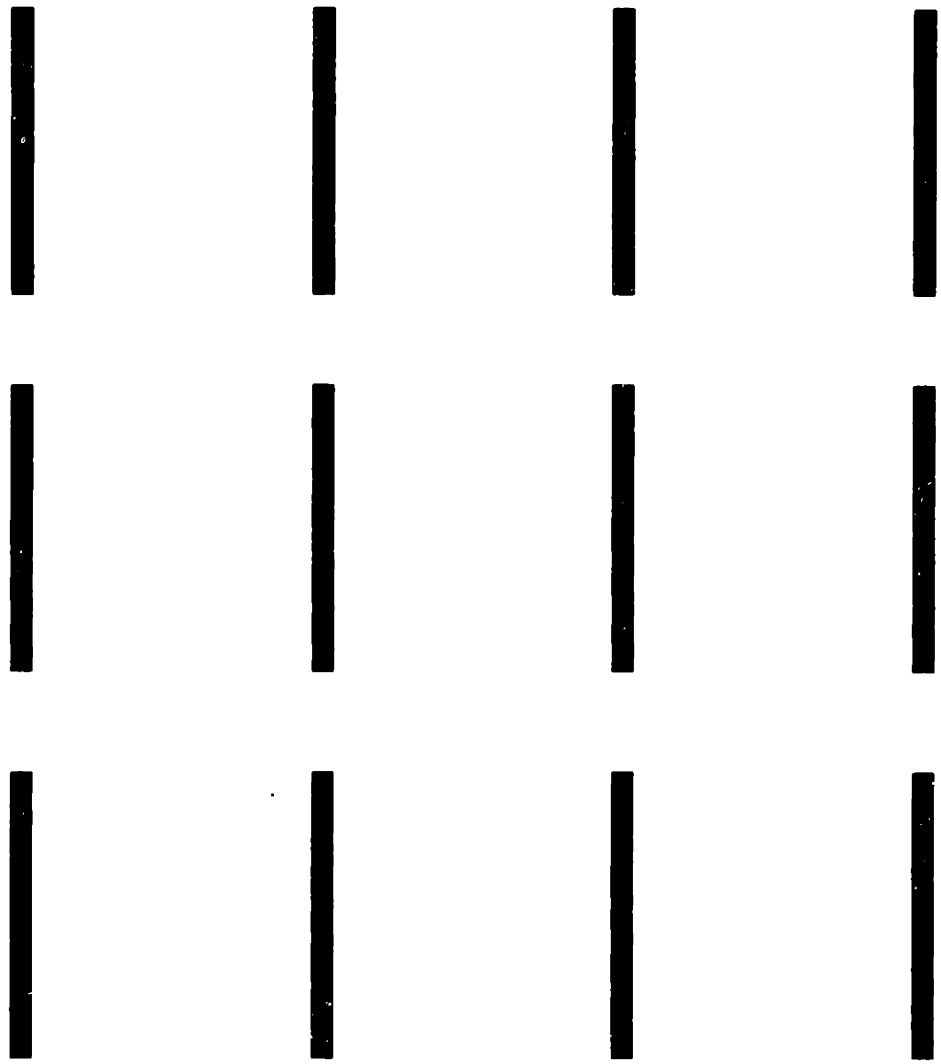

***Figure B.4*** *Mask (dark field) used to fabricate Si shadow mask. Since shadow mask fabrication was a single mask process, there were no alignment marks. The rectangular channel width was 1.1mm, which created slots that were 300μm wide on the frontside after the anisotropic KOH etch.*

# Appendix C Microreactor Fabrication Process Details

Step-wise sequence of the microreactor fabrication is detailed in this appendix. The fabrication was carried out in the Integrated Circuits Laboratory (ICL), Technology Research Laboratories (TRL), and Research Group Laboratories (RGL) at MIT.

## C.1 SiN microreactor fabrication process flow

Starting wafer: 100mm, <100> double-side polished, n-type or p-type (electrical properties irrelevant since no electronics are being integrated on-chip).

| Laboratory | Step | Process Description | Comments |
|---|---|---|---|
| ICL | 1 | RCA clean. | |
| ICL | 2 | Grow 1μm thick SiN in VTR tube (10:1 ratio of dichlorosilane and ammonia). | |
| TRL | 3 | Lithography for channel on wafer backside. Used 1μm thick photoresist coating and 1:1 contact mask. | Standard recipe. |
| ICL | 4 | Plasma etch SiN in etcher-1, $SF_6$ plasma, 300W power, ~2.5 min etch (characterize). | Recipe 15, Timed stop on Si, Overetch ok. |
| TRL | 5 | Piranha strip resist. | |
| TRL | 6 | Front side metal patterning, | Use image-reversal-resist. |

| | | | |
|---|---|---|---|
| | | Infra-red alignment from back to front. Use alignment jig and Karl Suss 1. | Follow recipe in TRL photo-room. |
| TRL | 7 | Descum in uv-ozone. | Clean residual resist. |
| TRL | 8 | Deposit 10nm Ti/100nm Pt using e-beam. | |
| TRL | 9 | Lift-off in acetone using ultra-sound. Nanostrip clean wafer. | |
| TRL | 10 | Sinter in tube A3 at 600 for 15 min. | |
| RGL | 11 | BOE dip 1min. KOH etch Si to stop on SiN membrane on frontside of wafer. Use 20% KOH soln at 90C. | Use DuPont one-sided etch-jig to protect Pt on frontside during this etch. |
| RGL | 12 | DI water rinse 3x and $N_2$ dry. | Post-KOH clean. |
| TRL | 13 | DI water rinse 3x. RCA-1 only in acid-hood in special metal container. Spin-dry in lithography room. | Post-KOH clean. RCA-2 and HF react with Ti and lifts-off metal. |
| TRL | 14 | Align shadow-mask and SiN micro-reactor. Dab uv-epoxy in epoxy holes (Appendix B)in microreactor to hold shadow mask. Cure for 1min in uv standard exposure. | Use alignment jig and Karl-Suss 1 mask - aligner. |
| TRL | 15 | e-beam evaporate catalyst in reactor channel. | |

| | | | |
|---|---|---|---|
| TRL | 16 | Separate shadow-mask and microreactor by dipping in acetone. Use razor-blade if necessary. | Piranha clean shadow-mask before reuse. |
| | 17 | Die-saw. | In die-saw room. |

**C.2 Shadow mask fabrication**

Starting wafer: 100mm, <100> double-side polished, n-type or p-type (electrical properties irrelevant since no electronics are being integrated on-chip).

| Laboratory | Step | Process Description | Comments |
|---|---|---|---|
| ICL | 1 | RCA clean | |
| ICL | 2 | Grow SiN in VTR tube<br>(10:1 ratio of dichlorosilane and ammonia). | Standard thickness<br>(150nm or higher). |
| TRL | 3 | Lithography for channel<br>1μm thick photoresist coating<br>1:1 contact mask on Karl Suss 1. | Standard recipe. |
| ICL | 4 | Plasma etch SiN in etcher-1.<br>$SF_6$ plasma, 300W power,<br>~2.5 min etch (characterize). | Recipe 15.<br>Timed stop on Si.<br>Overetch ok. |
| TRL | 5 | Piranha strip resist. | |
| RGL | 6 | BOE dip 1min. KOH etch Si to stop on SiN membrane on frontside of wafer.<br>Use 20% KOH in $H_2O$ solution at 90°C. | |

| | | | |
|---|---|---|---|
| RGL | 7 | DI water rinse 3x and $N_2$ dry. | Post-KOH clean. |
| TRL | 8 | DI water rinse 3x.<br>3:1 Piranha dip 15min and DI rinse 3x.<br>RCA clean.<br>Spin-dry in lithography room. | Standard Post-KOH clean. |
| ICL | 9 | RCA clean. | Standard Post-KOH clean. |
| ICL | 10 | Etch SiN in hot-phosphoric etch (180°C) in reflux bath. DI rinse and spin dry. | |

### C.3 Si microreactor fabrication process flow

Starting wafer: 100mm, 3μm thick device layer SOI wafer <100> n-type or p-type (electrical properties irrelevant since no electronics are being integrated on-chip). Note: Although double polished wafers would be desired, rough-backside wafers were used in this study.

| Laboratory | Step | Process Description | Comments |
|---|---|---|---|
| ICL | 1 | RCA clean. | |
| ICL | 2 | Grow 150nm thick SiN in VTR tube (10:1 ratio of dichlorosilane and ammonia). | Standard thickness (other thicknesses acceptable). |
| TRL | 3 | Lithography for channel on wafer backside. 1μm thick photoresist coating, 1:1 contact mask on Karl Suss 1. | Standard recipe |

| | | | |
|---|---|---|---|
| ICL | 4 | Plasma etch SiN in etcher-1,<br>$SF_6$ plasma, 300W power,<br>~2.5 min etch (characterize). | Recipe 15,<br>Timed stop on Si,<br>Overetch ok. |
| TRL | 5 | Piranha strip resist. | |
| RGL | 6 | BOE dip 1min.<br>KOH etch Si to depth of ~100μm.<br>Use 20% KOH soln at 90°C.<br>This step was necessary due to<br>rough wafer backside. | KOH etch partway through<br>wafer for clearer viewing in<br>step 7 for IR alignment.<br>Timed etch (overetch,<br>underetch ok) |
| RGL | 7 | DI rinse 3x and $N_2$ dry. | Standard Post KOH clean. |
| TRL | 8 | Piranha clean 15 min.<br>3:1 Piranha dip 15min and DI rinse 3x.<br>RCA clean.<br>Spin-dry in lithography room. | Standard Post KOH clean. |
| TRL | 9 | Front side metal patterning.<br>Infra-red alignment from back to<br>front. Use alignment jig and Karl-<br>Suss 1 aligner. | Use image-reversal-resist.<br>Follow recipe in TRL<br>photo-room. |
| TRL | 10 | Descum in uv-ozone. | Clean residual resist. |
| TRL | 11 | Deposit 10nm Ti/100nm Pt using e-beam. | |
| TRL | 12 | Lift-off in acetone using ultra-sound.<br>Nanostrip clean wafer. | |

| | | | |
|---|---|---|---|
| TRL | 13 | Sinter in tube A3 at 600°C for 15 min. | |
| RGL | 14 | BOE dip 1min.<br>KOH etch Si (20% in $H_2O$ at 90°C)<br>Stop on buried oxide.<br>Etch-stop visually determined due to Si membrane buckling.<br>BOE dip to remove oxide on Si membrane. | Use DuPont one-sided etch-jig to protect Pt on frontside during this etch. Si memebrane buckled due to oxide stress.<br>Si membrane smooth and de-stressed. |
| RGL | 15 | DI water rinse 3x and $N_2$ dry. | Post-KOH clean. |
| TRL | 16 | DI water rinse 3x.<br>RCA-1 only in acid-hood in special metal container.<br>Spin-dry in lithography room. | Post-KOH clean.<br>RCA-2 and HF react with Ti and lifts-off metal. |
| TRL | 17 | Align shadow-mask and SiN microreactor. Dab uv-epoxy in epoxy-holes (Appendix B) in microreactor and cure for 1min in uv standard exposure. | Use alignment jig and Karl-Suss 1 mask - aligner. |
| TRL | 18 | e-beam evaporate catalyst in reactor channel. | This step was optional.<br>Blanket deposition on some wafers. |
| TRL | 19 | Separate shadow-mask and microreactor | Piranha clean shadow- |

| | | |
|---|---|---|
| | by dipping in acetone. Use razor-blade if necessary. | mask before reuse |
| 20 | Die-saw. | In die-saw room. |

# Appendix D

# Microreactor Sealing Plate Design

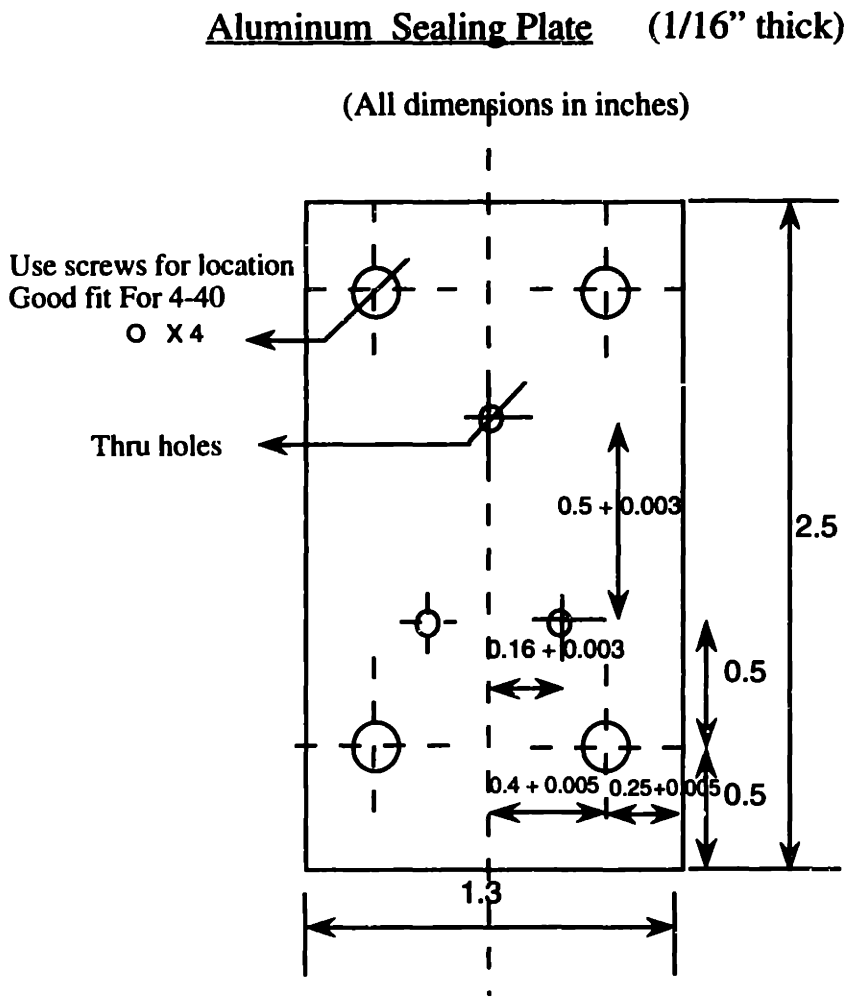

# Appendix E Gas Feedthrough Al block drawing

Material : Aluminum

Cartridge heater- 100W Omega Industries, part CIR-1041/"

All dimensions in inches

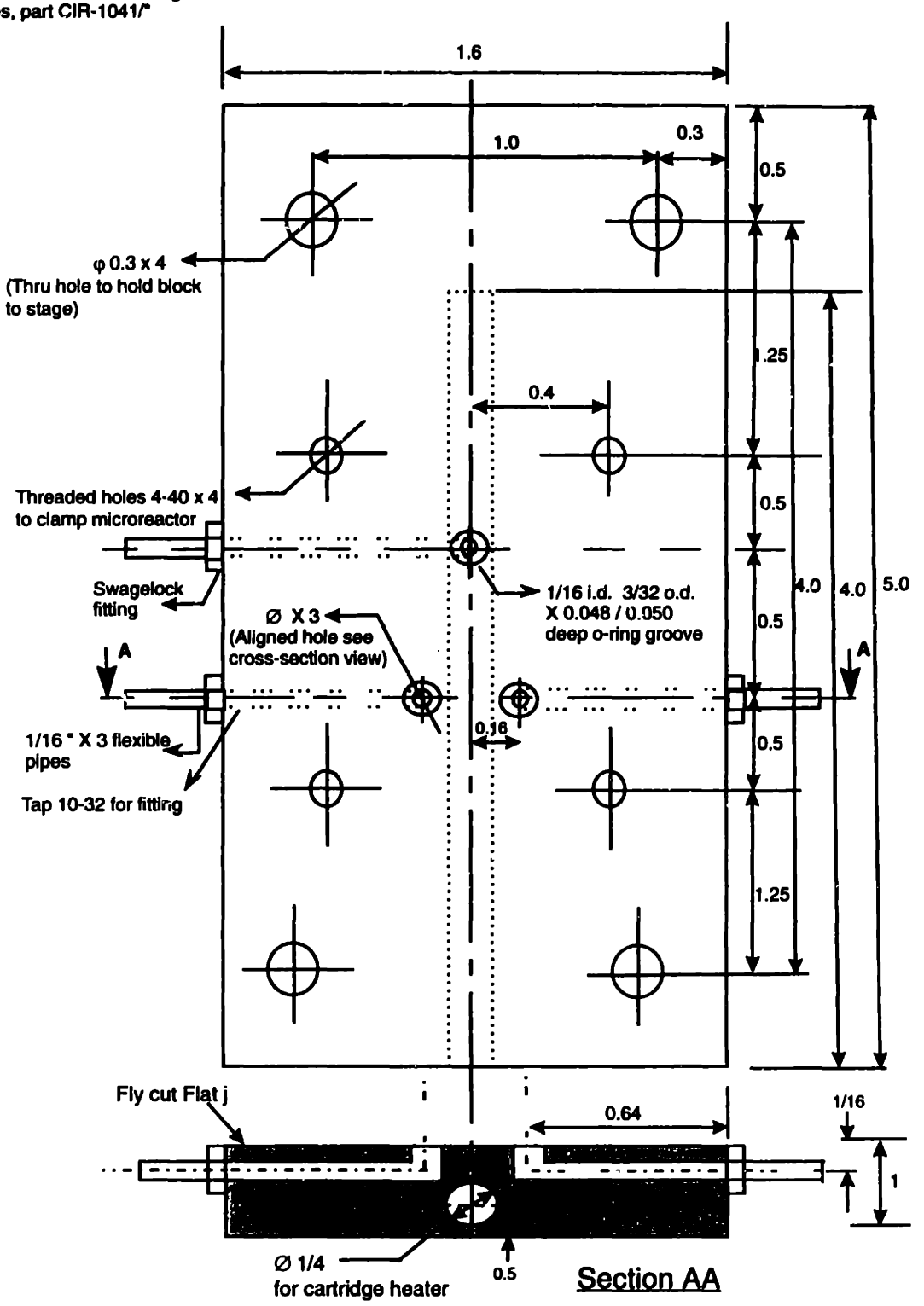

# Appendix F Mass Spectrometer Doser Fabrication

The mass spectrometer doser consists of a 1/16" stainless steel gas exhaust tubing was silver brazed to a blank copper gasket (Figure J.1). A 15mm i.d capillary tube (Polymicro Technologies Inc., 3035 N. 33rd drive, Phoenix, AZ 85017) was then epoxied to the exhaust tubing. A hole was drilled in the tubing for the capillary on the vacuum side of the copper gasket. The capillary of desired length (3.8cm) was inserted into the hole, and Torrseal® epoxy was applied for vacuum tight seal. The assembly was heated in ~180°C for ~30min in an oven to cure the epoxy. The capillary length of 3.8cm was determined by trial and error to maintain the vacuum chamber at 1e-5 torr.

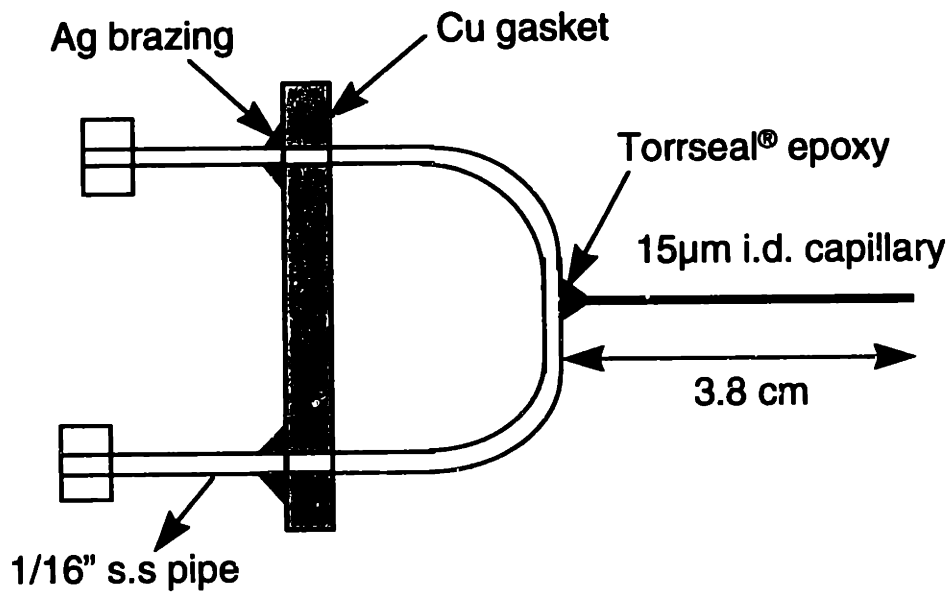


***Figure F.1** Schematic of capillary doser.*

# Appendix G Calibration Curves

This appendix details the calibration curves for different gases involved in $NH_3$ oxidation reaction. Gases were calibrated individually with $O_2$. The gas flowrate and $O_2$ flowrate were maintained using separate mass flow controllers. The gases were mixed using a Swagelock® Tee and dosed into the mass spectrometer using the microreactor experimental apparatus (Section 3.1). The peak heights are normalized with the peak height of 100% $O_2$ (mass number 32) for drift independent calibration. It is observed that the normalized peak heights are linear with composition, within experimental error. $NH_3$ calibration curve slopes are observed to be different at low compositions (0-10%) and high compositions (0-100%), primarily due to pressure changes in the system. $NH_3$ is known to adsorb on the chamber walls making its measurement difficult {Pignet, 1974 #2}. To get accurate $NH_3$ measurements, $NH_3$ calibrations were carried out immediately prior to, and immediately after a reaction, as explained in Section 3.3. The slope of the calibration curves of $N_2$ and NO are found to be the same at both low and high compositions.

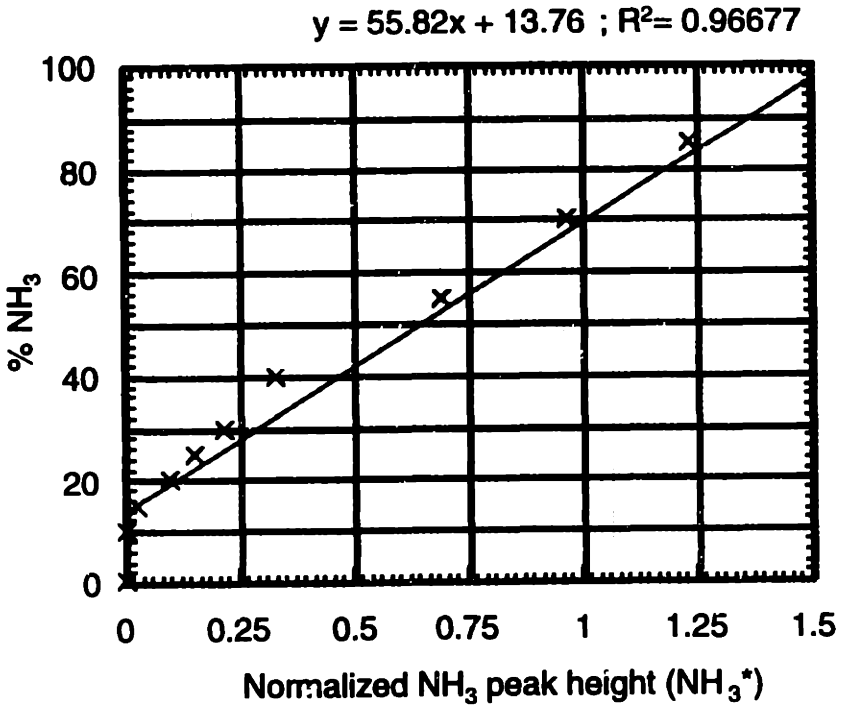


***Figure G.1** Calibration curve of %$NH_3$ (0-100%) as a function of normalized $NH_3$ peak height (normalized using 100% $O_2$ peak height).*

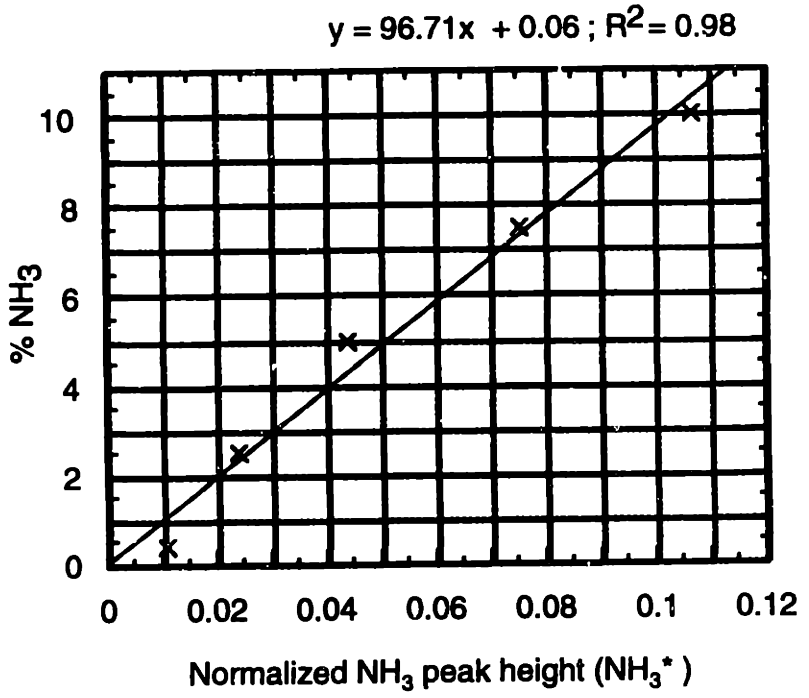


***Figure G.2** Calibration curve of %$NH_3$ (0-10%) as a function of normalized $NH_3$ peak height (normalized using 100% $O_2$ peak height).*

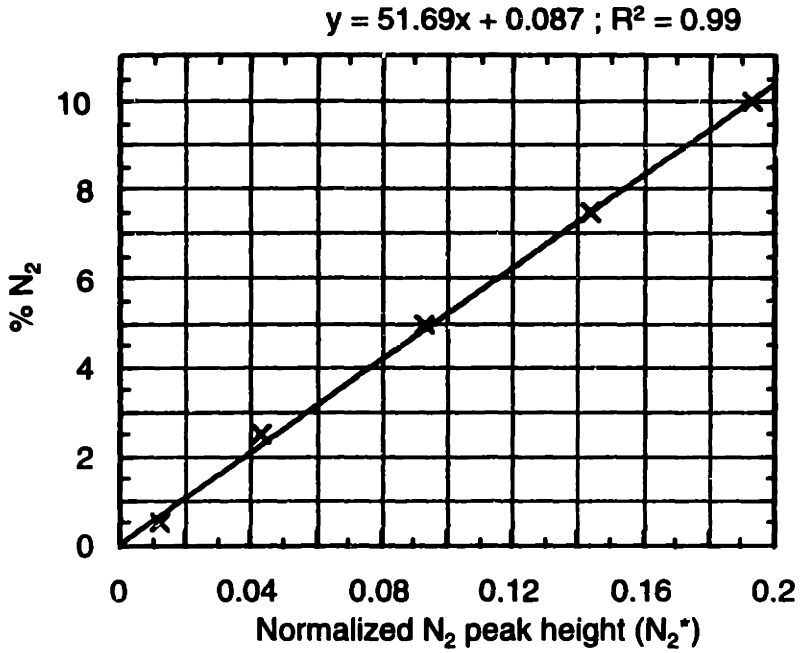


***Figure G.3*** *Calibration curve of $\%N_2$ (0-10%) as a function of normalized $N_2$ peak height (normalized using 100% $O_2$ peak height).*

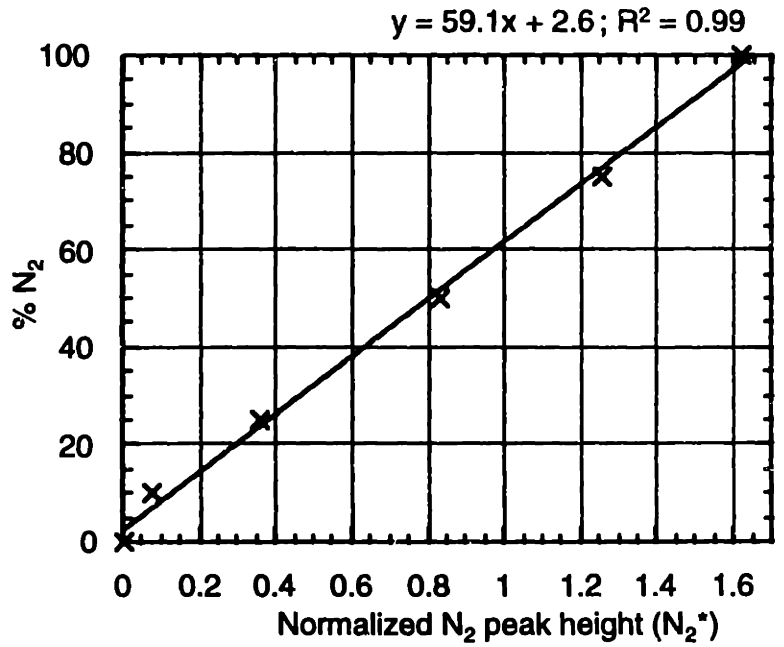


***Figure G.4*** *Calibration curve of $\%N_2$ (0-100%) as a function of normalized $N_2$ peak height (normalized using 100% $O_2$ peak height).*

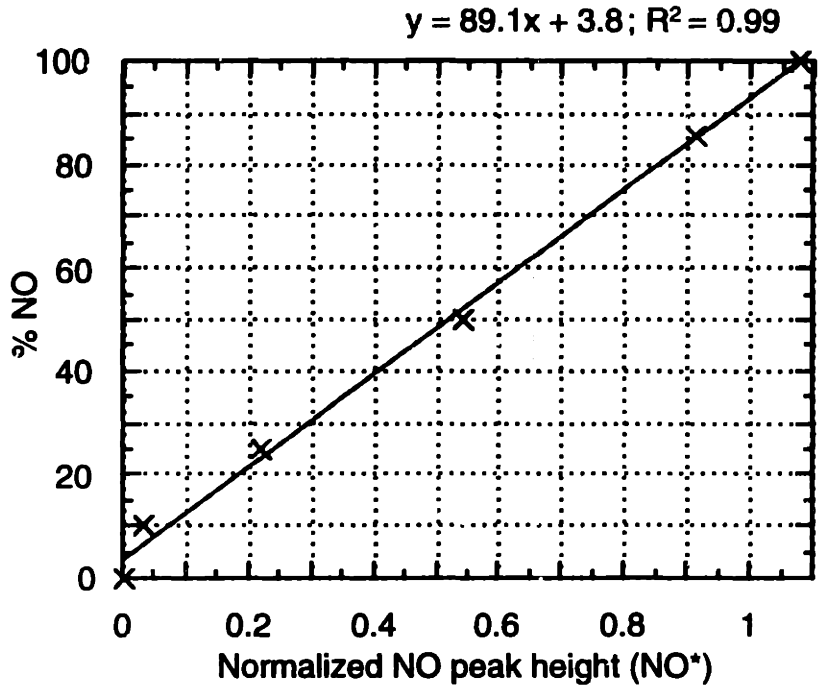


***Figure G.5*** *Calibration curve of %NO (0-100%) as a function of normalized NO peak height (normalized using 100% $O_2$ peak height).*

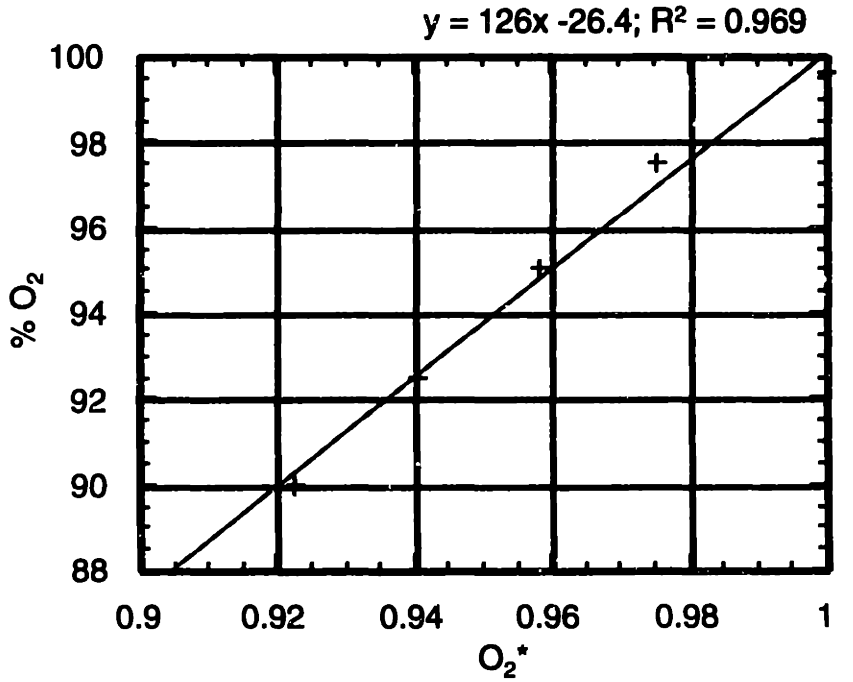


***Figure G.6*** *Calibration curve of %$O_2$ (90%- 100%) as a function of normalized $O_2$ peak height (normalized using 100% $O_2$ peak height). The carrier gas used was $NH_3$.*

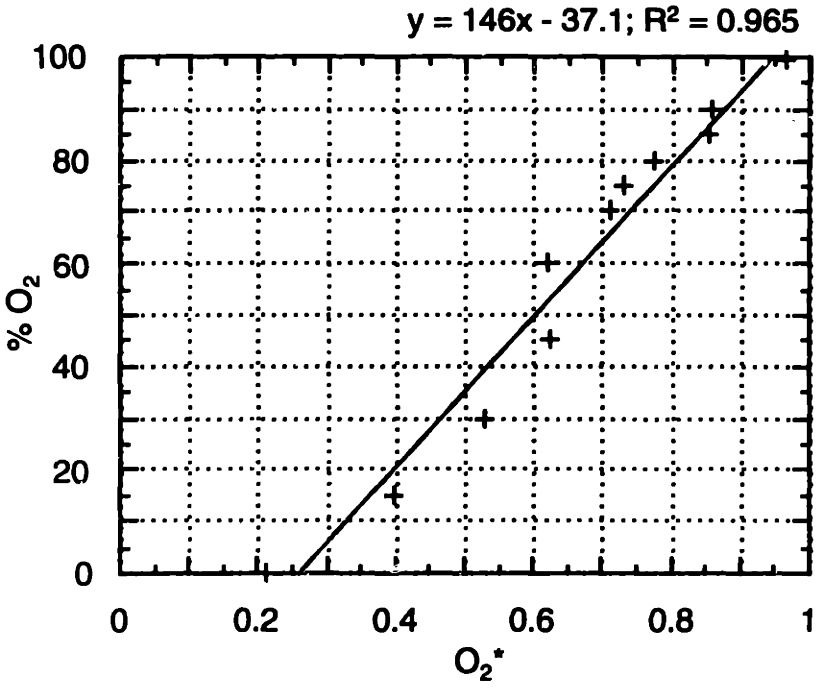


***Figure G.7** Calibration curve of $\%O_2$ (0-100%) as a function of normalized $O_2$ peak height (normalized with 100% $O_2$ peak height). The carrier gas used was $NH_3$.*

# Appendix H Experimental Error Analysis with a Sample Calculation

The sources of error in the temperature and concentration data and the calculation procedure to determine the error are outlined in this appendix with sample calculations.

***Error in temperature data***

To measure the temperature, a constant current of 1mA is applied to the sensor resistor and the voltage developed across the resistor is read into the data acquisition card. The error in the temperature data was due to the voltage resolution of the 12-bit data acquisition board (AT-MIO-64E-3). The (user-specified) maximum voltage setting of the card was 15V, giving a voltage resolution of 3.6 7 mV. The Johnson noise limit of the resistor was found to be negligible. The voltage generated by Johnson noise in a resistor is given by,

$V_{noise} = (4k_B TRB)^{0.5}$,

where $k_B$ is the Boltzmann constant ($1.38\times10^{-23}$ SI units), T is the temperature (900 °K), R is the resistance (300 Ω), and B is the bandwidth of data acquisition (10Hz). Substituting these values,

$V_{noise} = 10nV$, which is much lower than the data acquisition card resolution of 3.67mV.

The electrical resistance of the sensor is given by,

$R = R_o \cdot [1+\alpha \cdot (T - T_o)]$

where R is the resistance at T, $R_o$ is the resistance at $T_o$ (300Ω), and α is the temperature coefficient of resistance ( 3.9% / °C). Differentiating the equation gives,

$\Delta R = R_o \cdot \alpha \cdot \Delta T$,

or, $1mA \cdot \Delta R = 3.67mV = 1mA \cdot R_o \cdot \alpha \cdot \Delta T$

Substituting values and solving for $\Delta T$,

$\Delta T = 0.3\ ^{\circ}C$.

***Error calculation in concentration data***

The main source of error in concentration data was the drift in the mass spectrometer peak heights. $NH_3$ peak height was calibrated immediately prior to and immediately after an experiment (Figure H.1). The drift in the $NH_3$ peak height ($\Delta$) determined the error in the $NH_3$ exhaust concentration during reaction (*i.e.* drift in x).

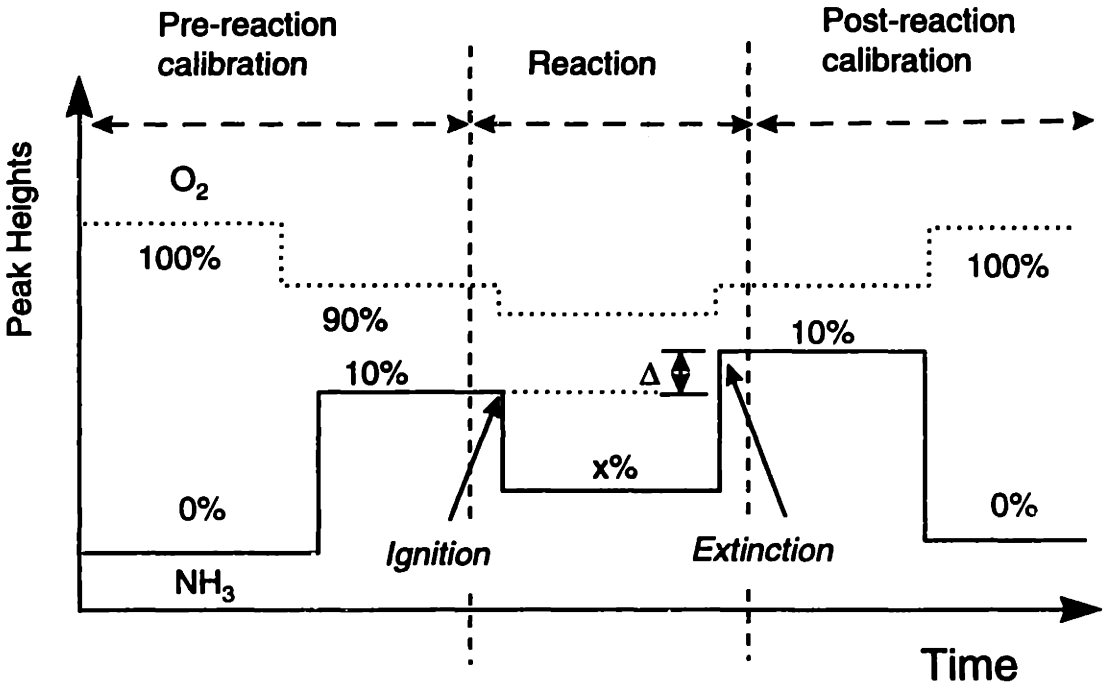


*Figure H.1 Typical experimental run used for the sample error calculation.*

Sample calculation:

Peak height of 10% $NH_3$ before reaction ($NH_{3,1}$*) = 5.4

Peak height of 10% $NH_3$ after reaction ($NH_{3,2}$ *)= 5.0.

$$\therefore \delta NH_3^* = 0.4$$

$$\delta x = \frac{\delta NH_3^*}{NH_{3,1}^*} \cdot inletNH_3\%$$

$$\Rightarrow \delta x = \frac{0.4}{5.4} \cdot 10\% = 0.8\% (= \pm 0.4\%)$$

***Error in Conversion data***

Since conversion (X) is defined as,

$$X = (1 - \frac{x}{inletNH_3\%}) \cdot 100\%$$

$$\delta X = \frac{\delta x}{inletNH_3\%} \cdot 100\%$$

$$\delta X = \frac{0.4}{10} \cdot 100\% = \pm 4\%.$$

Therefore, the error in conversion is ±4%.

***Error in selectivity data***

Since the drift is uniform for all the gases, Δ was also used to calculate the error in NO and $N_2$ concentrations. Assuming that the drift is proportional to the mass spectrometer sensitivity (experimentally verified),

$\delta\%NO = \delta x \cdot$(Mass spectrometer sensitivity to NO/ Mass spectrometer sensitivity to $NH_3$)

or, $\delta\%NO = \delta x \cdot$(Slope of NO calibration curve/ Slope of $NH_3$ calibration curve)

Getting the slope from the calibration curves in Appendix K, for our example case,

$$\therefore \delta\%NO = 0.4 \cdot \frac{1.2}{1.5}$$

$$\delta\%NO = \pm 0.32\%$$

Similarly,

$$\delta\%N_2 = 0.4 \cdot \frac{1.6}{1.5}$$

$$\delta\%N_2 = \pm 0.42\%$$

Since selectivity (S) is defined as,

$$S = \frac{\%NO}{\%NO + \%N_2}$$

$$\delta S = \frac{\delta\%NO}{\%NO + \%N_2} - \frac{\%NO \cdot (\delta\%NO + \delta\%N_2)}{(\%NO + \%N_2)^2}$$

$$\delta S = \frac{\%N_2 \cdot (\delta\%NO) - \%NO \cdot (\delta\%N_2)}{(\%NO + \%N_2)^2}$$

Substituting values for $\delta\%NO$ and $\delta\%N_2$, we get

$$\delta S = \frac{\%N_2 \cdot (0.32) + \%NO \cdot (0.42)}{(\%NO + \%N_2)^2}$$

Substituting the calculated %NO and $\%N_2$ will give the error in selectivity.